

# SMA Observations of Class 0 Protostars: A High-Angular Resolution Survey of Protostellar Binary Systems

Xuepeng Chen<sup>1,2</sup>, Héctor G. Arce<sup>2</sup>, Qizhou Zhang<sup>3</sup>, Tyler L. Bourke<sup>3</sup>, Ralf Launhardt<sup>4</sup>, Jes K. Jørgensen<sup>5</sup>, Chin-Fei Lee<sup>6</sup>, Jonathan B. Foster<sup>7</sup>, Michael M. Dunham<sup>2</sup>, Jaime E. Pineda<sup>8,9</sup>, and Thomas Henning<sup>4</sup>

<sup>1</sup>*Purple Mountain Observatory, Chinese Academy of Sciences, 2 West Beijing Road, Nanjing 210008, China; xpchen@pmo.ac.cn*

<sup>2</sup>*Department of Astronomy, Yale University, Box 208101, New Haven, CT 06520-8101, USA; xuepeng.chen@yale.edu*

<sup>3</sup>*Harvard-Smithsonian Center for Astrophysics, 60 Garden Street., Cambridge, MA 02138, USA*

<sup>4</sup>*Max Planck Institute for Astronomy, Königstuhl 17, D-69117 Heidelberg, Germany*

<sup>5</sup>*Niels Bohr Institute and Centre for Star and Planet Formation, Copenhagen University, Juliane Maries Vej 30, DK-2100 Copenhagen Ø, Denmark*

<sup>6</sup>*Academia Sinica Institute of Astronomy and Astrophysics, P.O. Box 23-141, Taipei 106, Taiwan*

<sup>7</sup>*Institute for Astrophysical Research, Boston University, Boston, MA 02215, USA*

<sup>8</sup>*ESO, Karl Schwarzschild Str. 2, 85748 Garching bei München, Germany*

<sup>9</sup>*Jodrell Bank Centre for Astrophysics, School of Physics and Astronomy, University of Manchester, Manchester, M13 9PL, UK*

## ABSTRACT

We present high angular resolution 1.3 mm and 850  $\mu\text{m}$  dust continuum data obtained with the Submillimeter Array toward 33 Class 0 protostars in nearby clouds (distance  $< 500$  pc), which represents so far the largest survey toward protostellar binary/multiple systems. The median angular resolution in the survey is 2''.5, while the median linear resolution is approximately 600 AU. Compact dust continuum emission is observed from all sources in the sample. Twenty-one sources in the sample show signatures of binarity/multiplicity, with separations ranging from 50 AU to 5000 AU. The numbers of singles, binaries, triples, and

quadruples in the sample are 12, 14, 5, and 2, respectively. The derived multiplicity frequency (MF) and companion star fraction (CSF) for Class 0 protostars are  $0.64 \pm 0.08$  and  $0.91 \pm 0.05$ , respectively, with no correction for completeness. The derived MF and CSF in this survey are approximately two times higher than the values found in the binary surveys toward Class I young stellar objects, and approximately three (for MF) and four (for CSF) times larger than the values found among main sequence stars, with a similar range of separations. Furthermore, the observed fraction of high order multiple systems to binary systems in Class 0 protostars ( $0.50 \pm 0.09$ ) is also larger than the fractions found in Class I young stellar objects ( $0.31 \pm 0.07$ ) and main sequence stars ( $\leq 0.2$ ). These results suggest that binary properties evolve as protostars evolve, as predicted by numerical simulations. The distribution of separations for Class 0 protostellar binary/multiple systems shows a general trend in which companion star fraction increases with decreasing companion separation. We find that  $67\% \pm 8\%$  of the protobinary systems have circumstellar mass ratios below 0.5, implying that unequal-mass systems are preferred in the process of binary star formation. We suggest an empirical sequential fragmentation picture for binary star formation, based on this work and existing lower resolution single-dish observations.

*Subject headings:* binaries: general — ISM: clouds — ISM: dust, extinction — stars: formation — techniques: interferometric

## 1. INTRODUCTION

Over the past two decades, our knowledge of the formation and evolution of low-mass stars has made significant progress (see, e.g., Reipurth et al. 2007 for several reviews). It is widely accepted that low-mass stars form from the gravitational collapse of molecular cloud cores (see, e.g., Shu et al. 1987; McKee & Ostriker 2007). Initially, these cores, generally referred to as prestellar cores, are cold dense condensations with infall motions that have not yet formed central stellar objects (André et al. 2000; 2009). Resulting from the collapse of prestellar cores, Class 0 objects are the youngest accreting protostars observed right after point mass formation, when most of the mass of the system is still in the surrounding dense core/envelope (André et al. 2000). As the protostellar envelope dissipates through accretion and ejection of circumstellar material, Class 0 protostars evolve into Class I young stellar objects (YSOs; Lada 1987). Class I YSOs subsequently evolve into pre-main sequence (PMS) stars surrounded by circumstellar disks, but without dense envelopes. Eventually, PMS stars evolve into main sequence (MS) stars.

One of the major puzzles in our understanding of star formation concerns the origin of binary stars (Tohline 2002). A series of surveys toward solar-type MS stars have found that about 40%–60% of MS stars are actually binary systems, with periods from less than one day to over 10 million years (e.g., Duquennoy & Mayor 1991; Fischer & Marcy 1992). The binary frequency found among PMS stars is even higher than that among the MS stars (e.g., Mathieu 1994). For example, in the survey toward PMS stars in the Taurus star formation region, Köhler & Leinert (1998) found that for systems with separations from 18 AU to 1800 AU the binary frequency is  $48.9\% \pm 5.3\%$ , which is larger than a factor of two compared to the binary frequency in solar-type MS stars with the same separation range. Recent surveys toward Class I YSOs show that binary systems are also common in the Class I phase (see, e.g., Haisch et al. 2004; Duchêne et al. 2004, 2007; Connelley et al. 2008a, b). For example, the large survey by Connelley et al. (2008a, b) found that for Class I YSOs the binary frequency for separations from 100 AU to 4500 AU is about 43%. The high frequency of binary systems found in different stellar evolution stages has led to a widely held opinion that most stars form in binary/multiple systems (e.g., Mathieu 1994; Goodwin et al. 2007). In contrast, however, Lada (2006) argued that the most common outcome of the star formation process is a single star rather than a binary star, based on two observational facts: (1) that most low-mass stars (stellar mass  $< 0.5 M_{\odot}$ ) are single objects (e.g., Delfosse et al. 2004; Siegler et al. 2005), and (2) that these low-mass stars represent the majority of the field stars (Kroupa 2002; Chabrier 2005).

Do most stars form as singles or binaries? Before trying to answer this question still in debate, it must be noted that multiple stellar systems undergo dynamical evolution at the beginning of their formation phase (e.g., Reipurth & Clarke 2001; Reipurth et al. 2010). Dynamical evolution will modify the binary population by reducing the overall binary fraction and by hardening the remaining binaries on a timescale of less than  $10^5$  yr (see Goodwin et al. 2007). Therefore, neither observations of PMS/Class I young stars nor observations of field dwarfs can constrain the *original* properties of binary/multiple systems. Clearly, the most effective way to answer this question is to extensively observe the earliest stages of the star formation process.

Class 0 objects, which represent the youngest protostars at an age of a few  $10^4$ – $10^5$  yr (André et al. 2000; Evans et al. 2009), provide an important opportunity to probe the earliest phase of the star formation process, where most of the initial information of (binary) star formation is expected to still be preserved. To understand the formation of binary stars, it is therefore critical to observe large samples of Class 0 protostars in nearby molecular clouds to answer a number of key questions, e.g., how common is binarity/multiplicity in the Class 0 protostellar phase? What are the initial distributions of separations and mass ratios? Unfortunately, direct observations of the Class 0 protostellar stages, when the main

collapse has started but no optical or near-infrared emission emerges from the protostar through the opaque infalling envelope, were long hampered by the low angular resolution of single-dish (sub-)millimeter telescopes. Only the high angular resolution attained with current millimeter interferometers enables us to directly observe the formation phase of binary stars. In the past decade, a handful of Class 0 protostellar binary (protobinary) systems have been found using different interferometric arrays (e.g., Looney et al. 2000; Reipurth et al. 2002; Launhardt 2004), and there are increasing interferometric studies of binarity in the protostellar phase (e.g., Volgenau et al. 2006; Maury et al. 2010). However, these studies were limited to small samples of objects and no statistically strong conclusions could be drawn from them.

On the theoretical side, numerous simulations support the hypothesis that the fragmentation of molecular cloud cores is the main mechanism for the formation of binary/multiple stellar systems (see reviews by Bodenheimer et al. 2000, Tohline 2002, and Goodwin et al. 2007). Yet, many key questions concerning this fragmentation process (e.g., exactly *when*, *where*, *why*, and *how*) are still under debate. In general, fragmentation models can be classified depending on when the fragmentation takes place during the different collapse phases of the core<sup>1</sup>. Initial clump/filament fragmentation takes place prior to the collapse of individual cores, and results in cores with separations of  $\sim 10^3\text{--}10^4$  AU (see, e.g., Kauffmann et al. 2008; Launhardt et al. 2010), while prompt (isothermal) fragmentation takes place at the end of the core’s isothermal collapse phase, and results in fragments with separations of  $\sim 10^2\text{--}10^3$  AU (see Tohline 2002). On the other hand, adiabatic fragmentation occurs when the collapse evolves into the adiabatic phase, and results in fragments with separations of  $\sim 3\text{--}300$  AU (Machida et al. 2005; 2008). Finally, secondary fragmentation takes place during the core’s secondary collapse phase, and results in fragments with separations of 0.01 to 0.1 AU (Machida et al. 2008). In all these cases, fragmentation takes place when there is some angular momentum in the core (see the review by Goodwin et al. 2007). The source of the angular momentum may be ordered rotational motions (i.e., rotational fragmentation) or turbulence (i.e., turbulent fragmentation).

These different possible models of fragmentation result in different binary/multiple systems with a wide range of properties. These properties are largely determined by the accretion process which, in turn, strongly depends on the initial conditions of the cloud cores, e.g., the initial distributions of mass and angular momentum (see Bate & Bonnell 1997). It must be noted that the constraints used on current binary formation models mostly come from the observations of MS and PMS stars. These observations cannot provide information on the

---

<sup>1</sup>See, e.g., Figure 2 in Tohline 2002 or Figure 9 in André et al. 2009 for a discussion of the different evolutionary phases of core collapse.

initial conditions of fragmenting cores. Hence, it is critical to observe the early phase of core fragmentation and study in detail their properties (e.g., mass and separation distributions), in order to put direct constraints on different fragmentation models.

To achieve a comprehensive understanding of binary star formation, we have started a systematic program to observe at different (sub-) millimeter interferometers a large sample of low-mass prestellar and protostellar cores. The early survey was conducted at the Owens Valley Radio Observatory (OVRO) millimeter array (Chen et al. 2007; R. Launhardt et al. in preparation), and was then continued with the Australia Telescope Compact Array (ATCA; Chen et al. 2008a), the IRAM Plateau de Bure Interferometer (PdBI; Chen et al. 2009; X. Chen et al. in preparation), and the Submillimeter Array (SMA; Chen et al. 2008b; Chen & Arce 2010). As part of this program, we present in this paper high angular resolution (sub-) millimeter continuum observations toward 33 Class 0 protostars using the SMA, which represents so far the largest survey of protobinary systems. High angular resolution (sub-) millimeter continuum emission traces the circumstellar dust from the inner envelopes and disks surrounding protostars, which we used to resolve binary/multiple systems, and measure their masses, sizes, and spatial distribution. In Section 2 we describe the target list, observations, and data reduction. Observational results are presented in Section 3 and discussed in Section 4. The main conclusions of this study are summarized in Section 5. We give a detailed description of the individual sources in Appendix A.

## 2. SAMPLE, OBSERVATIONS, AND DATA REDUCTION

### 2.1. Sample

The sources in this study were collected from the SMA science archive. A total of 33 sources were selected by using the following three criteria: (1) available in the SMA archive<sup>2</sup>; (2) confirmed classification as a Class 0 object by other studies; and (3) known distance less than 500 pc. These sources were observed at the SMA between 2004 and 2009 with different science goals (e.g., for studying outflow, kinematics, or chemistry in the Class 0 protostars). Only for a few sources (i.e., IRAS 03282, NGC 1333 SVS 13, and CG 30), the proposed science goal was to study the formation of binary stars. The target list and their basic properties (i.e., bolometric luminosity  $L_{\text{bol}}$ , bolometric temperature  $T_{\text{bol}}$ , and envelope mass  $M_{\text{env}}$ ) are summarized in Table 1. Most sources in Table 1 were cataloged by both André et al.

---

<sup>2</sup>All the SMA data used in this work are publicly available from the SMA archive. Some of the data are unpublished and in Tables 2-3 we list the name of the principle investigator (PI) responsible for the observations. For data that had been published we list the paper that first presented the data in Tables 2-3.

(2000) and Froebrich (2005). We refer readers to these two papers and references therein for more details about the basic properties of these sources. Note that several sources may represent transition objects between the Class 0 and Class I phases (see Froebrich 2005 for more detailed discussion).

Distances to the different sources were obtained from the literature. Early estimates of the distance to Perseus indicated that this region is 350 pc away (e.g., Herbig & Jones 1983). However, more recent studies indicate that this region is significantly closer. Photometric distances towards the western part of Perseus place this cloud at 220 pc (Černis 1990; Černis & Straižys 2003), consistent with recent VLBI observations that give a distance to NGC 1333 of  $240 \pm 20$  pc (Hirota et al. 2008, 2011). We therefore adopt a distance of 240 pc for all objects in Perseus, in agreement with other recent studies of this cloud (e.g., Enoch et al. 2006; Evans et al. 2009; Arce et al. 2010, 2011). The basic properties (bolometric luminosity and envelope mass) of the Perseus sources listed in André et al. (2000) and Froebrich (2005) were modified using the new distance of 240 pc (see Table 1). For sources in the Taurus star forming region, we adopt a distance of 140 pc (Elias 1978; Kenyon et al. 1994; Loinard et al. 2007b). For sources in the Orion region, we adopt a distance of 440 pc, obtained by the VLBI observations of Hirota et al. (2007). For sources in the Ophiuchus cloud, we use a distance of 120 pc, derived from recent VLBA observations by Loinard et al. (2008). For the Lupus region, the distance is estimated to be 130 pc (Murphy et al. 1986). For isolated objects, the distance references are as follows: CB 17 (Launhardt et al. 2010), CG 30 (Knude et al. 1999), L483 (Dame & Thaddeus 1985), L723 (Goldsmith et al. 1984), B335 (Tomita et al. 1979), L1157 (Straižys et al. 1992), and L1251B (Kun & Prusti 1993).

## 2.2. Observations

Observations were carried out with the SMA<sup>3</sup> (Ho et al. 2004) between 2004 and 2009. Five different array configurations, Subcompact (Subcom), Compact (Com), Compact-North (Com-N; for several equatorial and southern sources), Extended (Ext), and Very Extended (V-Ext), were used in the observations, with baselines ranging from about 10 m to 500 m. Only one source, IRAS 16293–2422, was also observed with the Extended Submillimeter Array (eSMA<sup>4</sup>).

---

<sup>3</sup>The Submillimeter Array is a joint project between the Smithsonian Astrophysical Observatory and the Academia Sinica Institute of Astronomy and Astrophysics and is funded by the Smithsonian Institution and the Academia Sinica.

<sup>4</sup>See <http://www.jach.hawaii.edu/JCMT/eSMA/> for more details.

Table 1. Basic properties of target sources

Source Name	Other (or short) Name <sup>a</sup>	Association Region	Distance [pc]	$L_{\text{bol}}$ [ $\text{L}_{\odot}$ ]	$T_{\text{bol}}$ [K]	$M_{\text{env}}$ [ $\text{M}_{\odot}$ ]	Class	References <sup>b</sup>
L1448 IRS2	IRAS 03222+3034	Perseus	240	1.7-4.1	43-63	0.6-1.4	0	1, 2, 3, 4
L1448 N	IRAS 03225+3034	Perseus	240	4.3-17	53-90	1.5-4.5	0/I	1, 2, 3, 4
L1448 C	L1448-mm	Perseus	240	4.4-6.3	49-69	0.7-1.9	0	1, 2, 3, 4
PER 065	Per-Bolo 30	Perseus	240	0.03-0.22	31-37	0.4-2.1	0	3, 4
NGC 1333 IRAS 2A	IRAS 2A	Perseus	240	19-23	50-69	1.0-2.8	0	1, 2, 3, 4
NGC 1333 IRAS 2B	IRAS 2B	Perseus	240	19-23	50-69	1.0-2.8	0	1, 2, 3, 4
NGC 1333 SVS 13	SVS 13	Perseus	240	7-33	30-180	1.3-3.3	0/I	1, 2, 3, 4
NGC 1333 IRAS 4A	IRAS 4A	Perseus	240	4.2-8.5	34-51	2.7-7.8	0	1, 2, 3, 4
NGC 1333 IRAS 4B	IRAS 4B	Perseus	240	1.6-7.6	36-54	1.4-3.7	0	1, 2, 3, 4
IRAS 03282+3035	IRAS 03282	Perseus	240	0.7-1.2	33-60	0.4-1.0	0	1, 2, 3, 4
Per B1-c	B1-c	Perseus	240	1.8-3.7	53-76	2.1-18	0/I	3, 4, 5, 6
Per B1-b	B1-b	Perseus	240	1.2-2.5	< 25	2.8-26	0	3, 5, 7
HH 211-MM		Perseus	240	1.5-4.5	24-31	0.5-3.0	0	1, 2, 3, 4
IC 348 MMS		Perseus	240	0.5-1.9	49-59	1.8-10	0	3, 4
CB 17 IRS	L1389	Isolated	250	0.6	> 55	< 4	0/I	8
IRAM 04191+1522	IRAM 04191	Taurus	140	0.12-0.28	18-36	0.5	0	1, 2, 9, 10
L1521F-IRS	L1521F/MC 27	Taurus	140	0.1-0.36	20	0.7-4.8	0	11, 12, 13
L1527 IRS	IRAS 04368+2557	Taurus	140	1.9-2.2	36-60	0.4-0.9	0/I	1, 2, 14
HH 114 MMS		Orion	440	< 25	40-84	1.4-2.8	0	1, 2
OMC 3 MM 6		Orion	440	< 60	30-72	6-12	0	1, 2
NGC 2024-FIR 5		Orion	440	$\geq 10$	20	8.2-15	0	1, 2
HH 212-MM		Orion	440	7.7-14	< 56	0.3-1.2	0	1, 2
HH 25 MMS		Orion	440	6.0-7.2	34-41	0.5-1.2	0	1, 2
CG 30	BHR 12	Isolated	200	10-17	74-117	1.1-2.3	0/I	1, 2
B228	IRAS 15398-3359	Lupus	130	0.9-1.2	48-61	0.3-0.4	0	2, 14
VLA 1623		Ophiuchus	120	0.4-1.2	< 59	0.2-0.5	0	1, 2, 4
Oph MMS 126	IRAS 16253-2429	Ophiuchus	120	0.25	35	0.51	0	4
IRAS 16293-2422	IRAS 16293	Ophiuchus	120	6.9-14	41-54	1.2-2.8	0	1, 2, 4
L483	IRAS 18148-0440	Isolated	200	9-13	50-54	0.3-1.8	0/I	1, 2, 14
L723 VLA2	IRAS 19156+1906	Isolated	300	3-3.3	47-50	0.6-1.6	0	1, 14
B335	IRAS 19345+0727	Isolated	250	3.0-3.1	28-45	0.7-1.2	0	1, 2, 14
L1157	IRAS 20386+6751	Isolated	325	5.8-11	42-60	0.5-2.6	0	1, 2, 14
L1251 B IRS1	IRAS 22376+7455	Isolated	300	$\leq 10$	83-87	2.0-2.1	0/I	2, 15, 16

<sup>a</sup>The IRAS source is not always associated with the mm source.

<sup>b</sup>References for the basic properties of the objects. — (1) André et al. (2000); (2) Froberich (2005); (3) Hatchell et al. (2007); (4) Enoch et al. (2009); (5) Matthews & Wilson (2002); (6) Matthews et al. (2006); (7) Hirano et al. (1999); (8) Launhardt et al. (2010); (9) André et al. (1999); (10) Dunham et al. (2006); (11) Crapsi et al. (2004); (12) Bourke et al. (2006); (13) Terebey et al. (2009); (14) Shirley et al. (2000); (15) J. Lee et al. (2006); (16) J. Lee et al. (2007).

Table 2. SMA observation log: 1.3 mm dust continuum

Source Name	R.A. & Dec. (J2000) <sup>a</sup> [h:m:s, ° : ' : "]	Observing Dates [day/month/yr]	Array configurations	UV coverage [kλ]	HPBW <sup>b</sup> [arcsecs]	rms <sup>c</sup> [mJy/beam]	PI or Referred Paper
L1448 IRS2	03:25:22.40, +30:45:12.0	04/11/07, 06/11/07	Com	7-53	3.4×2.5	0.68/2.1	J. Foster
L1448 N	03:25:36.00, +30:45:20.0	21/11/07	Com	8-59	2.8×2.4	0.74/7.0	Jørgensen et al. (2007)
L1448 C	03:25:38.80, +30:44:05.0	07/11/04	Com-N	8-107	2.7×1.9	1.1/4.0	Jørgensen et al. (2007)
PER 065	03:28:39.10, +31:06:01.8	20/01/09, 28/01/09	Com	6-53	3.7×2.7	0.45/5.5	T.-H. Hsieh
NGC 1333 IRAS2 (A, B)	03:28:55.70, +31:14:37.0	07/11/04	Com-N	8-107	2.8×1.9	1.4/1.8	Jørgensen et al. (2007)
NGC 1333 SVS 13	03:29:03.07, +31:15:52.0	07/12/08	Com	9-59	2.8×2.6	0.40/2.5	X. Chen
NGC 1333 IRAS4 (A, B)	03:29:10.50, +31:13:31.0	22/11/04, 17/01/06	Com-N, Com	9-140	1.5×1.4	1.4/12	Jørgensen et al. (2007)
IRAS 03282	03:31:21.00, +30:45:30.0	08/12/08	Com	6-59	2.5×2.2	0.37/1.8	X. Chen
Per-B1c	03:33:17.88, +31:09:32.0	17/10/05	Com	6-53	3.4×2.9	1.6/2.7	B. Matthews
Per-B1b	03:33:21.14, +31:07:35.3	10/09/07, 11/09/07	Subcom, Com	5-52	7.6×4.5	0.91/4.2	N. Hirano
IC 348 MMS	03:43:57.30, +32:03:09.0	20/11/05	Com	5-53	3.3×3.0	3.3/4.0	M. Reid
CB 17 IRS	04:04:35.85, +56:56:03.1	30/11/08	Com	6-53	3.1×2.8	0.44/0.5	X. Chen
IRAM 04191	04:21:56.90, +15:29:46.4	02/11/07, 03/11/07	Com	9-54	3.7×3.1	0.60/0.5	J. Karr
L1521F-IRS	04:28:38.95, +26:51:35.1	03/01/07	Com	9-53	3.4×2.4	0.98/1.5	N. Ohashi
L1527	04:39:53.90, +26:03:10.0	08/11/04	Com-N	11-108	2.7×1.8	0.91/1.4	Jørgensen et al. (2007)
HH 114 MMS	05:18:15.20, +07:12:02.0	28/11/05, 01/12/05	Com	8-52	3.4×3.1	1.3/5.0	H. Arce
HH 212 MM	05:43:51.30, -01:02:53.0	30/10/06, 25/11/06	Ext, V-Ext	22-390	0.8×0.7	0.63/1.1	C.-F. Lee
CG 30	08:09:33.00, -36:05:08.0	07/03/08	Com	6-53	5.0×2.0	1.3/4.0	X. Chen
B 228	15:43:02.16, -34:09:09.0	29/04/09	Com	5-87	3.9×2.4	1.4/1.5	A. Hedden
B 228 (1.1 mm)	15:43:02.16, -34:09:09.0	12/05/09	Com	8-109	2.5×1.9	1.4/1.6	A. Hedden
VLA 16 <sup>d</sup> 23	16:26:26.36, -24:24:30.3	25/05/07, 11/06/07	V-Ext	22-390	0.6×0.3	0.38/1.0	N. Ohashi
Oph MMS 126	16:28:21.60, -24:36:23.4	02/05/08	Com	7-93	4.8×2.2	2.0/2.1	K. Stapelfeldt
IRAS 16293	16:32:22.91, -24:28:35.5	22/06/04, 18/02/05	Com-N, Com	7-146	1.5×1.2	1.2/19	T. Bourke
L723 VLA2	19:17:53.40, +19:12:19.4	07/08/04, 22/10/04	Com	11-106	2.9×2.1	0.81/1.2	Girart et al. (2009)
B335	19:37:00.89, +07:34:10.0	24/06/05	Com	6-54	3.4×3.1	0.98/2.9	Jørgensen et al. (2007)
L1157	20:39:06.19, +68:02:15.9	06/07/05	Com	5-52	4.3×2.7	1.2/4.8	Jørgensen et al. (2007)
L1251 B	22:38:47.20, +75:11:28.7	25/09/05	Com	5-42	4.1×3.1	3.0/3.2	J. Lee et al. (2007)

<sup>a</sup>Phase center of the observations (if more than two pointings in the observations, the final figure center of the mosaic image is listed here).

<sup>b</sup>Synthesized FWHM beam size with robust weighting (weighting parameter 1.0).

<sup>c</sup>1 σ theoretical noise (robust weighting 1.0) / 1 σ rms noise in the cleaned map.

Table 3. SMA observation log: 850  $\mu\text{m}$  dust continuum

Source Name	R.A. & Dec. (J2000) <sup>a</sup> [h:m:s, ° : ' : '']	Observing Dates [day/month/yr]	Array configurations	UV coverage [k $\lambda$ ]	HPBW <sup>b</sup> [arcsecs]	rms <sup>c</sup> [mJy/beam]	PI or Referred Paper
L1448 C	03:25:38.55, +30:44:13.4	05/12/06, 25/12/06	Com, Ext	10–265	0.97×0.65	1.6/5.5	Hirano et al. (2010)
NGC 1333 IRAS2A	03:28:55.57, +31:14:37.2	17/10/04, 08/01/06	Com, Ext	17–265	0.75×0.61	1.7/4.5	Jørgensen et al. (2007)
NGC 1333 IRAS4A	03:29:10.50, +31:13:31.0	11/11/04, 20/11/04	Com-N, Com	14–143	1.8×0.86	2.8/24	Jørgensen et al. (2007)
IRAS 03282	03:31:21.00, +30:45:30.0	24/08/09, 25/10/09	Com, Ext	17–265	0.86×0.76	1.1/4.0	X. Chen
HH 211-MM	03:43:56.80, +32:00:50.3	23/01/08, 18/08/08	Ext, V-Ext	60–600	0.20×0.15	2/1.4	Lee et al. (2009, 2010)
HH 114 MMS	05:18:15.20, +07:12:02.0	31/12/05	Com	10–78	2.2×1.9	3.1/16	H. Arce
OMC3 MMS6	05:35:23.49, −05:01:32.2	15/11/07, 15/12/07, 15/02/09	Com, Ext	15–210	1.4×1.1	1.5/20	Y.-W. Tang
NGC 2024-FIR5	05:41:44.25, −01:55:40.8	24/11/07, 19/12/07	Com	15–88	2.2×1.3	2.8/14	Alves et al. (2011)
HH 212 MM	05:43:51.41, −01:02:53.1	02/12/05, 14/01/06, 18/11/06	Com, Ext, V-Ext	10–550	0.35×0.32	2.3/2.8	Lee et al. (2007a, 2008)
HH 25 MMS	05:46:07.56, −00:13:41.6	21/12/06, 19/02/07, 26/08/08	Subcom, Com, Com-N	8–165	2.3×1.9	1.2/6.8	Q. Zhang
IRAS 16293	16:32:22.90, −24:28:35.5	22/03/09	eSMA	30–900	0.35×0.30	1.3/18	S. Bottinelli
L483	18:17:29.86, −04:39:38.8	18/06/05, 10/07/05	Com	13–82	2.6×1.9	1.7/3.2	Jørgensen et al. (2007)

<sup>a</sup>Phase center of the observations (if more than two pointings in the observations, the final figure center of the mosaic image is listed here).

<sup>b</sup>Synthesized FWHM beam size with robust weighting (weighting parameter 1.0).

<sup>c</sup>1  $\sigma$  theoretical noise (robust weighting 1.0) / 1  $\sigma$  rms noise in the cleaned map.

The 230 GHz and 345 GHz receivers were used in the observations. Both receivers have two sidebands (lower and upper), with 2 GHz bandwidth each (separated by 10 GHz). The receiver setups were typically tuned to the CO (2–1) line in the 230 GHz observations (see, e.g., Chen et al. 2008b; 2010) and to the CO (3–2) line in the 345 GHz observations (see, e.g., Jørgenson et al. 2007; Lee et al. 2009). The total continuum bandwidth, combining the line-free portions of the two sidebands, are about 3.0–3.8 GHz for the 1.3 mm and 850  $\mu$ m dust continuum. We present only the continuum results in this paper. At 230 GHz, system temperatures generally range from 80 to 300 K (depending on elevation), with a typical value of 150 K. At 350 GHz, system temperatures range from 150 to 500 K, with a typical value of 250 K. The SMA primary beams are  $\sim 55''$  at 230 GHz and  $\sim 36''$  at 345 GHz.

The visibility data were reduced using the MIR package (Qi 2005). During the reduction, visibility points with clearly deviating phases and/or amplitudes were flagged. The passband (spectral response) was calibrated through observations of available planets (e.g., Saturn) and strong quasars (e.g., 3C 454.3) at the beginning and/or end of each track. Time variation of amplitude and phase was calibrated through frequent observations of quasars near to each source. The flux density scale was calibrated by observing planets such as Uranus and Ceres. For a few tracks, strong quasars (e.g., 3C 273) with stable flux densities during the observing dates, were also used as flux calibrators. We estimate a typical flux accuracy of about 20%–30%. The calibrated visibility data were then imaged using the MIRIAD toolbox (Sault et al. 1995). Each continuum map was deconvolved down to the  $1\sigma$  theoretical rms noise level using the MIRIAD *clean* routine. The synthesized beam sizes (with robust weighting 1.0) and rms noise levels are summarized in Tables 2 and 3. Figure 1 shows the beam sizes plotted as a function of the corresponding linear resolutions. The median angular resolution in this survey is  $3''.1$  at  $\lambda 1.3$  mm and  $1''.0$  at  $\lambda 850 \mu$ m, corresponding to the median linear resolutions of approximately 640 AU and 220 AU, respectively. Combining the observations at the two wavelengths, the median angular and linear resolutions in this survey are  $2''.5$  and 600 AU, respectively. Figure 2 shows the distribution of the rms noise levels. The median  $1\sigma$  theoretical noise is  $1.0$  mJy beam $^{-1}$  at  $\lambda 1.3$  mm and  $1.7$  mJy beam $^{-1}$  at  $\lambda 850 \mu$ m, while in the cleaned images, the median  $1\sigma$  noise is  $2.3$  mJy beam $^{-1}$  and  $5.5$  mJy beam $^{-1}$ , respectively.

### 3. RESULTS: SMA SUBMILLIMETER AND MILLIMETER MAPS

Figures 3–17 present the SMA submillimeter and millimeter maps for the sources listed in Table 1. Most sources in Table 1 were observed with SCUBA on the James Clerk Maxwell Telescope (JCMT). Complementary SCUBA submillimeter images are also shown for selected regions and sources, to illustrate the relative locations of the protostellar cores within the

clouds and/or the overall morphology of the sources. The SCUBA data for the sources in the Perseus and Ophiuchus clouds are available from the COMPLETE database<sup>5</sup>. The data for other objects were retrieved from the JCMT science archive<sup>6</sup>.

In the SMA observations, millimeter and/or submillimeter dust continuum emission is detected from all the sources in the sample. It must be noted that in this work we regard a local density peak or enhancement as a source if its emission is  $\geq 5\sigma$  levels with respect to its immediate surrounding. Except several very low luminosity sources such as PER 065 (see Figure 4), L1521F-IRS (see Figure 9c), and Oph-MMS 126 (see Figure 15c), most sources in the sample show centrally peaked emission in the SMA dust continuum images, suggesting the existence of a compact inner envelope and/or circumstellar disk in these sources.

As shown in the SCUBA images (angular resolution of  $\sim 14''$  at  $850\mu\text{m}$ ), most sources in the sample appear to be single cores (except CG 30). At the high angular resolution obtained with the SMA (median angular resolution of  $3''.1$  at  $1.3\text{ mm}$  and of  $1''.0$  at  $850\mu\text{m}$ ), 22 sources in the sample show signatures of binarity/multiplicity, with angular separations from  $0''.3$  (HH 211 MMS) to  $22''$  (CG 30). Detailed descriptions of the individual sources are presented in Appendix A.

Tables 4 and 5 list the derived parameters (e.g., positions, integrated fluxes, and deconvolved FWHM sizes) for each of the sources/components ( $\geq 5\sigma$  level) from circular Gaussian fits to the visibilities. The statistical uncertainties on the derived parameters are generally small and are mainly determined by the rms noise levels of the images (see Tables 2 and 3). On the other hand, the calibration uncertainties of the fluxes are 20%–30%, and thus dominate the uncertainties of the derived fluxes. For a few faint components in the systems such as IRAS 03282, NGC 1333 IRAS 2A, and HH 212 MMS, their fluxes are uncertain to within a factor of two, due to uncertainties in separating their emission from the surrounding envelope emission.

Figure 18 shows the distribution of fluxes derived in this work. The  $1.3\text{ mm}$  fluxes range from  $1.1\text{ mJy}$  to  $3.0\text{ Jy}$ , with a median value of  $100\text{ mJy}$ , while the  $850\mu\text{m}$  fluxes range from  $20\text{ mJy}$  to  $3.2\text{ Jy}$ , with a median value of  $430\text{ mJy}$ . Compared with the total fluxes obtained from the single-dish IRAM-30 m images at  $1.3\text{ mm}$  (see, e.g., Kauffmann et al. 2008; Launhardt et al. 2010) and the SCUBA images at  $850\mu\text{m}$  (see, e.g., Chandler & Richer 2000; Shirley et al. 2000; Sandell & Knee 2001), the SMA resolved out a significant fraction

---

<sup>5</sup>See Ridge et al. (2006) and <http://www.cfa.harvard.edu/COMPLETE/> for more details.

<sup>6</sup><http://cadcwww.dao.nrc.ca/jcmt/>. The JCMT archive at the Canadian Astronomy Data Center is operated by the Herzberg Institute of Astrophysics, National Research Council of Canada.

(generally 80%–90%) of the extended emission and detected only the compact emission in the center of protostellar cores (i.e., inner envelopes and circumstellar disks).

Assuming that the 1.3 mm and 850  $\mu\text{m}$  continuum emission is optically thin, the total gas mass ( $M_{\text{gas}}$ ) of the individual sources can be derived from the (sub-) millimeter fluxes using the formula:

$$M_{\text{gas}} = \frac{F_\nu D^2}{\kappa_m(\nu) B_\nu(T_d)} \quad (1)$$

where  $F_\nu$  is the flux of the source,  $D$  is the distance to the source,  $T_d$  is the dust temperature,  $\kappa_m(\nu)$  is the dust opacity (mass absorption coefficient per gram of dust, e.g., 1.75  $\text{cm}^2 \text{g}^{-1}$  at 850  $\mu\text{m}$  for OH5 dust; see Ossenkopf & Henning 1994), and  $B_\nu(T_d)$  is the Planck function at frequency  $\nu$  and dust temperature  $T_d$ . In practice, we use the same method as in Jørgensen et al. (2007) to calculate the masses (adopting a dust temperature of 30 K for all sources),

$$M_{1.3 \text{ mm}} = 1.3 M_\odot \left( \frac{F_{1.3 \text{ mm}}}{1 \text{ Jy}} \right) \left( \frac{D}{200 \text{ pc}} \right)^2 \times \{ \exp[0.36 \left( \frac{30 \text{ K}}{\text{T}} \right)] - 1 \}, \quad (2)$$

$$M_{0.85 \text{ mm}} = 0.18 M_\odot \left( \frac{F_{0.85 \text{ mm}}}{1 \text{ Jy}} \right) \left( \frac{D}{200 \text{ pc}} \right)^2 \times \{ \exp[0.55 \left( \frac{30 \text{ K}}{\text{T}} \right)] - 1 \}. \quad (3)$$

Column 5 of Tables 4 and 5 lists the total gas masses for each sources, calculated from the 1.3 mm and 850  $\mu\text{m}$  fluxes. The relative uncertainty of the derived masses due to calibration errors of the (sub-) millimeter fluxes is about 20%–30% for all sources. Moreover, due to the uncertainties in the dust opacity and temperature, the masses obtained this way may contain uncertainties of up to a factor of two.

Figure 18 shows the distribution of gas masses for the objects in this sample. The masses derived from the 1.3 mm observations range from  $0.001 M_\odot$  to  $2.4 M_\odot$ , with a median value of  $0.06 M_\odot$ , while the masses derived from the 850  $\mu\text{m}$  observations range from  $0.005 M_\odot$  to  $1.7 M_\odot$ , with a median value of  $0.12 M_\odot$ . Compared with the masses derived from single-dish observations, e.g., a median value of  $\sim 0.5 M_\odot$  derived from IRAM-30m 1.3 mm observations for protostars (see Kauffmann et al. 2008), the masses derived from this SMA survey are relatively small and represent only lower limits to the core masses. As indicated above, most of the (sub-) millimeter continuum emission is resolved out in the SMA images, and it is very likely that detected emission arises from the inner envelope and circumstellar disk. Therefore, the derived masses may also be regarded as upper limits to the disk masses (see, e.g., Jørgensen et al. 2009 for further discussion).

Table 4. SMA 1.3 mm dust continuum results.

Source	R.A. <sup>a</sup> (J2000)	Dec. <sup>a</sup> (J2000)	$S_{\nu}^a$ [mJy]	FWHM <sup>a</sup> (maj.'' × min.'')	$M_{\text{gas}}^b$ [ $M_{\odot}$ ]
L1448 IRS2	03:25:22.38	+30:45:13.3	180±36	3.9×2.3	0.15
L1448N A	03:25:36.48	+30:45:21.8	140±30	3.0×1.4	0.11
L1448N B	03:25:36.33	+30:45:14.8	660±130	2.3×1.6	0.54
L1448N NW	03:25:35.66	+30:45:34.2	70±14	3.5×2.5	0.057
L1448C N	03:25:38.88	+30:44:05.5	200±40	1.6×0.9	0.16
L1448C S	03:25:39.05	+30:43:59.3	20±5	5.7×1.9	0.016
PER 065 A	03:28:39.17	+31:05:55.6	4.4±1	8.1×6.5	0.004
PER 065 B	03:28:38.86	+31:05:56.8	1.1±0.2	2.3×1.3	0.001
PER 065 C	03:28:38.96	+31:06:04.2	1.5±0.3	2.3×2.1	0.001
NGC 1333 IRAS 2A	03:28:55.58	+31:14:37.2	330±66	1.8×1.3	0.27
NGC 1333 IRAS 2B	03:28:57.38	+31:14:15.8	50±10	3.8×2.0	0.04
NGC 1333 SVS 13 A	03:29:03.75	+31:16:03.6	450±90	2.7×2.0	0.37
NGC 1333 SVS 13 VLA3	03:29:03.41	+31:16:01.5	22±5	(unresolved)	0.02
NGC 1333 SVS 13 B	03:29:03.07	+31:15:51.8	460±90	2.8×2.3	0.37
NGC 1333 SVS 13 C	03:29:01.97	+31:15:38.1	50±10	2.2×0.7	0.04
NGC 1333 IRAS 4A	03:29:10.51	+31:13:31.3	3000±600	2.4×1.7	2.43
NGC 1333 IRAS 4B	03:29:12.01	+31:13:08.2	920±180	1.4×0.9	0.75
NGC 1333 IRAS 4C	03:29:12.84	+31:13:07.0	250±50	0.7×0.6	0.20
IRAS 03282	03:31:20.94	+30:45:30.2	290±60	1.4×1.3	0.24
Per-B1-c	03:33:17.87	+31:09:32.3	300±60	3.1×2.4	0.24
Per-B1-bN	03:33:21.19	+31:07:43.6	240±50	4.6×3.2	0.19
Per-B1-bS	03:33:21.33	+31:07:26.3	340±70	3.2×1.8	0.28
IC348 MMS1	03:43:57.05	+32:03:05.0	260±50	2.5×1.9	0.21
IC348 MMS2	03:43:57.73	+32:03:10.5	65±15	4.4×2.6	0.053
CB 17 IRS	04:04:33.76	+56:56:16.5	6.3±1.3	3.4×2.5	0.006
CB 17 MMS	04:04:35.78	+56:56:03.4	3.6±0.7	3.6×1.1	0.003
IRAM 04191 IRS	04:21:56.89	+15:29:46.1	4.5±1.5	2.8×2.7	0.001
IRAM 04191 MMS	04:21:56.36	+15:29:48.9	2.5±1.0	3.7×1.1	< 0.001
L1521F IRS	04:28:38.91	+26:51:34.6	15±5	5.0×2.1	0.004
L1527	04:39:53.90	+26:03:09.8	190±40	1.0×0.5	0.052
HH 114 MMS	05:18:15.24	+07:12:02.7	490±100	1.9×1.6	1.34
HH 212 MMS	05:43:51.41	-01:02:53.1	76±15	0.6×0.5	0.21
CG 30 N	08:09:33.13	-36:04:58.3	260±50	3.3×1.9	0.15
CG 30 S	08:09:32.73	-36:05:19.3	100±20	4.6×2.4	0.06
B228	15:43:02.20	-34:09:07.6	150±30	5.5×3.9	0.036
B228 (1.1 mm)	15:43:02.13	-34:09:07.3	135±30	5.4×4.3	0.032
VLA 1623 W	16:26:25.64	-24:24:29.3	42±10	1.1×0.7	0.009
VLA 1623 E A	16:26:26.39	-24:24:30.7	79±15	1.0×0.8	0.016
VLA 1623 E B	16:26:26.31	-24:24:30.4	71±15	0.6×0.6	0.014
Oph-MMS 126	16:28:21.58	-24:36:23.6	11±2	3.6×1.7	0.002
IRAS 16293 A	16:32:22.87	-24:28:36.6	620±120	1.7×1.4	0.13
IRAS 16293 B	16:32:22.62	-24:28:32.6	1300±260	1.6×1.4	0.26
L723 VLA2 MMS1	19:17:53.68	+19:12:19.8	59±12	2.7×2.0	0.075
L723 VLA2 MMS2	19:17:53.91	+19:12:18.4	58±12	3.2×1.4	0.074
B335	19:37:00.93	+07:34:09.9	145±30	4.5×2.4	0.13

Table 4—Continued

Source	R.A. <sup>a</sup> (J2000)	Dec. <sup>a</sup> (J2000)	$S_{\nu}^a$ [mJy]	FWHM <sup>a</sup> (maj.'' × min.'')	$M_{\text{gas}}^b$ [ $M_{\odot}$ ]
L1157	20:39:06.18	+68:02:16.3	280±56	3.1×3.0	0.42
L1251B IRS1	22:38:46.68	+75:11:33.1	48±10	4.2×2.3	0.061
L1251B IRS2	22:38:52.94	+75:11:23.2	21±4	3.6×3.3	0.027
L1251B SMA N	22:38:48.95	+75:11:33.4	17±4	4.9×4.7	0.022
L1251B SMA S	22:38:49.09	+75:11:25.0	28±6	6.1×4.2	0.035

<sup>a</sup>Center position, flux, and FWHM size of the dust continuum sources derived from Gaussian fitting.

<sup>b</sup>Total gas mass derived from the SMA 1.3 mm dust continuum observations. Note that the gas mass is from compact emission only, not the whole envelope.

Table 5. SMA 850  $\mu\text{m}$  dust continuum results.

Source	R.A. <sup>a</sup> (J2000)	Dec. <sup>a</sup> (J2000)	$S_{\nu}^a$ [mJy]	FWHM <sup>a</sup> (maj.'' × min.'')	$M_{\text{gas}}^b$ [ $M_{\odot}$ ]
L1448C N	03:25:38.87	+30:44:05.3	410±80	0.6×0.4	0.078
L1448C S	03:25:39.14	+30:43:60.0	40±10	1.2×0.6	0.008
NGC 1333 IRAS 2A1	03:28:55.57	+31:14:37.1	800±160	1.1×0.8	0.15
NGC 1333 IRAS 2A2	03:28:55.55	+31:14:38.5	40±10	(unresolved)	0.008
NGC 1333 IRAS 4A1	03:29:10.53	+31:13:31.0	3200±600	1.4×0.4	0.61
NGC 1333 IRAS 4A2	03:29:10.44	+31:13:32.2	1600±300	1.1×0.1	0.30
IRAS 03282 MMS1	03:31:20.94	+30:45:30.3	340±70	0.2×0.1	0.065
IRAS 03282 MMS2	03:31:21.08	+30:45:29.9	30±10	(unresolved)	0.006
HH 211 SMM1	03:43:56.80	+32:00:50.3	80±20	0.1×0.1	0.015
HH 211 SMM2	03:43:56.79	+32:00:50.0	25±10	< 0.1	0.005
HH 114 MMS	05:18:15.23	+07:12:02.5	1100±220	1.3×1.2	0.70
OMC3 MMS6 SMM1	05:35:23.43	-05:01:30.6	1350±200	1.0×0.8	0.86
OMC3 MMS6 SMM2	05:35:23.52	-05:01:41.2	550±100	1.8×1.7	0.35
NGC2024 FIR5 SMM1	05:41:44.26	-01:55:40.9	2640±500	2.9×1.8	1.69
NGC2024 FIR5 SMM2	05:41:44.51	-01:55:42.4	1030±200	3.5×3.0	0.66
HH 212 MMS1	05:43:51.41	-01:02:53.1	260±50	2.0×1.0	0.17
HH 212 MMS2	05:43:51.38	-01:02:53.0	20±4	(unresolved)	0.013
HH 212 MMS3	05:43:51.48	-01:02:53.8	27±5	0.5×0.4	0.018
HH 25 SMM1	05:46:07.26	-00:13:30.7	510±100	2.8×2.4	0.33
HH 25 SMM2	05:46:07.34	-00:13:43.4	430±80	1.3×0.7	0.27
HH 25 SMM3	05:46:07.58	-00:13:53.7	150±30	4.8×4.6	0.10
IRAS 16293 Aa	16:32:22.86	-24:28:36.6	980±200	0.8×0.7	0.05
IRAS 16293 Ab	16:32:22.88	-24:28:36.3	430±90	0.9×0.6	0.02
IRAS 16293 B	16:32:22.62	-24:28:32.5	3130±630	0.6×0.4	0.15
L483	18:17:29.94	-04:39:39.3	140±28	2.2×0.8	0.02

<sup>a</sup>Center position, flux, and FWHM size of the dust continuum sources derived from Gaussian fitting.

<sup>b</sup>Total gas mass derived from the SMA 850  $\mu\text{m}$  dust continuum observations. Note that the gas mass is from compact emission only, not the whole envelope.

## 4. DISCUSSION

### 4.1. Multiplicity in the Class 0 Phase

Before analyzing the binary/multiple frequency in the Class 0 protostellar phase, it is important to note how binary/multiple systems are defined in this work. Strictly speaking, only systems that show bound motions can be referred to as binary/multiple systems. However, compared with well-studied MS/PMS binaries (for which the orbital motion can be determined by direct imaging or spectroscopic monitoring at optical and near-infrared wavelengths; see Duchêne et al. 2007), these kinds of systems are extremely rare in the protostellar phase (see, e.g., Rodríguez 2004). The main reasons are: (1) the sample of protobinary systems is relatively small, (2) it is difficult to directly observe the protostellar phase, due to the limitation of angular resolution obtained at millimeter wavelengths, and (3) it is difficult to monitor bound motion in protobinary systems, as most known protobinary systems have large separations (100–1000 AU) and thus have long orbital periods. In this work, we use the following criterion to define binary/multiple systems: *the separation or the closest separation (if there are more than two components in the systems) is less than 5000 AU*. We explain below why we choose 5000 AU as the limit.

As introduced in Section I, through initial fragmentation, large-scale ( $\sim 0.1\text{--}1.0\,\text{pc}$ ) molecular clumps (or filaments) fragment into individual dense cores, which subsequently collapse to form individual stellar systems (i.e., fragmented components from initial clump fragmentation are not bound stellar systems but prestellar cores). The fragmented components from initial fragmentation generally have separations of more than 5000 AU, consistent with the typical Jeans length in large-scale molecular clumps/filaments (4000–5000 AU at  $T = 10\,\text{K}$  and  $n_{\text{H}_2} = 10^5\text{--}10^6\,\text{cm}^{-3}$ ). This is also in agreement with the results from the high angular resolution survey by Looney et al. (2000) that systems with separations  $\leq 6000\,\text{AU}$  have common envelopes while wider systems have separated envelopes. Interestingly, by analyzing observational data in the Taurus region (e.g., Ghez et al. 1993; Gomez et al. 1993), Larson (1995) also found the existence of an ‘intrinsic’ scale ( $\sim 0.04\,\text{pc}$  or 8000 AU) in binary star formation process, and this scale is found to be consistent with the Jeans length in large molecular clouds. Therefore, we consider that components with separations  $> 5000\,\text{AU}$  are likely not relevant for the formation of bound stellar systems. This is also the reason why we list several well-known sources, e.g., NGC 1333 IRAS 2A & 2B (separation  $\sim 7500\,\text{AU}$ ) and IRAS 4A & 4B (separation  $\sim 7200\,\text{AU}$ ), as separate targets in this work (see Table 1).

We use the densities of YSOs and dense cores in the Perseus molecular cloud to estimate the likelihood of identifying a background or foreground source as a possible binary (or multiple) companion in this study. Many of the targets (14 of 33, or 42%) in this sam-

ple are located in the Perseus cloud, and most of the rest of the sources are in regions with lower protostellar densities. In general, main sequence and evolved stars foreground and background to the cloud have very small amounts of (or no) circumstellar dust, and should be undetectable by this interferometric submillimeter and millimeter continuum survey. Therefore, the only possible “contaminating” sources in this study should be young stars with dusty circumstellar envelopes associated with the cloud. In Perseus, there are a total of 400 YSOs in an area of  $3.86 \text{ deg}^2$  (see Jørgensen et al. 2006). Assuming that these YSOs all have detectable dust continuum emission at the SMA, the density of potential dust continuum sources is  $103.6 \text{ YSOs}/\text{deg}^2$ . We therefore estimate the probability of there being a contaminating YSO within a 5000 AU ( $21''$  at the distance of Perseus) radius that could mistakenly be identified as a companion to be 0.01. Another estimate of the contamination likelihood can be obtained using the density of dense cores detected in previous single-dish dust continuum surveys. Hatchell et al. (2005; SCUBA 850  $\mu\text{m}$ ) and Enoch et al. (2006; Bolocam 1.1 mm) found 91 (within an area of  $3 \text{ deg}^2$ ) and 122 (within an area of  $7.5 \text{ deg}^2$ ) dense cores in Perseus, respectively. From these two large-scale surveys, the probabilities are estimated to be  $3.2 \times 10^{-3}$  and  $1.7 \times 10^{-3}$ , respectively. Hence, it is very unlikely that any of the identified companions in this work are background or foreground sources.

Nevertheless, we want to note that further high angular resolution kinematical data are important for complementing the separation criterion used here. For example, for relatively wide protobinary systems ( $> 1000 \text{ AU}$ ), molecular line observations are needed to verify if the components therein have similar systematic velocities, in order to insure that the components resolved therein are physically associated<sup>7</sup>. For close systems (on the scale of 100 AU), high angular resolution line (e.g., CO or H<sub>2</sub>) observations are needed to distinguish if each component drives its own outflow, in order to be sure that each component is associated with a protostellar object (and not a dense, starless, condensation).

In this work, we adopt the following terminology and definitions to describe the complexities of binary/multiple stars:

$$\text{multiplicity frequency (MF)} = \frac{B + T + Q}{S + B + T + Q}, \quad (4)$$

$$\text{companion star fraction (CSF)} = \frac{B + 2T + 3Q}{S + B + T + Q}, \quad (5)$$

---

<sup>7</sup>For several wide protobinary systems (e.g., L1448N, L1448C, IRAM 04191, CG 30, and L723), high angular resolution molecular line observations have already found that the components resolved therein have similar systematic velocities.

where  $S$ ,  $B$ ,  $T$ , and  $Q$  are the numbers of single, binary, triple, and quadruple systems, respectively. The ‘multiplicity frequency’, suggested by Reipurth & Zinnecker (1993), represents the probability that any system is a binary/multiple system. The ‘companion star fraction’, on the other hand, looks at the individual stars and counts the number of companions relative to the sample size. It should be noted that many previous works used ‘companion star fraction’ rather than ‘multiplicity frequency’ in their analysis (see, e.g., Haisch et al. 2004; Duchêne et al. 2004; Connelley et al. 2008b). Actually, as noted by Reipurth & Zinnecker (1993), the most precise description of multiplicity consists of explicitly listing the number of singles, binaries, triples, and quadruples, like  $S:B:T:Q$ , although this description (as well as others) does not account for hierarchicality.

In this SMA survey toward 33 protostars, 22 sources show signatures of binarity or multiplicity (see Appendix A for detailed descriptions of the individual sources). Table 6 lists the names of these sources, as well as their basic observed parameters (separation and circumstellar mass ratio). If we adopt 5000 AU as the limit, source CB 17 (21''.4 or 5350 AU) is beyond this limit and will *not* be regarded as a “bound” binary system in this work. Therefore, the numbers of singles<sup>8</sup>, binaries<sup>9</sup>, triples<sup>10</sup>, and quadruples<sup>11</sup> are considered to be 12, 14, 5, and 2, respectively, which is  $S:B:T:Q = 0.86:1.00:0.36:0.14$  when normalized to the number of binaries. The overall multiplicity frequency (MF) and companion star fraction (CSF) derived in the sample, without correcting for completeness (see below), is  $0.64 \pm 0.08$  and  $0.91 \pm 0.05$ , respectively, with the separations in the range between 50 AU (which is the smallest separation we detect between two components) and 5000 AU (the limit set in this work). The statistical standard errors are estimated as  $[MF(1-MF)/N]^{1/2}$  and  $[CSF(1-CSF)/N]^{1/2}$  (where  $N$  is the total number of sources in the sample), respectively.

It is important to note that the angular resolution is not uniform in this SMA survey (see Tables 2 & 3). The median angular resolution in the survey is 2''.5, corresponding to a median linear resolution of 600 AU in nearby clouds (see Figure 1). There are very likely more binary/multiple systems with separations less than 600 AU unresolved in this survey. Therefore, this survey is incomplete across the observed separation range. However, it is difficult to correct for this incompleteness at present, because we would have to adopt as-

<sup>8</sup>L1448 IRS2, NGC1333 IRAS 2B, B1c, CB 17, L1521F-IRS, L1527IRS, HH 114 MMS, B228, Oph MMS 126, L483, B335, and L1157

<sup>9</sup>L1448C, NGC1333 IRAS 2A, IRAS 4A, IRAS 4B, IRAS 03282, B1b, HH 211 MMS, IC348 MMS, IRAM 04191, OMC3 MMS6, NGC2024-FIR5, HH 25 MMS, CG 30, and L723 VLA2

<sup>10</sup>L1448N, PER 065, HH 212 MMS, VLA 1623, and IRAS 16293

<sup>11</sup>NGC 1333 SVS 13 and L1251B

sumptions regarding to the separation distributions of Class 0 protobinary systems, which are unfortunately unknown yet (see further discussion in § 4.2). Consequently, the multiplicity frequency and companion star fraction derived from this work could be considered as lower limits over the separation range observed here.

Recently, Maury et al. (2010) argued that binary systems are relatively rare in the Class 0 phase, as only one object shows a possible binary detection in their small PdBI survey toward five Class 0 objects. However, two protobinary systems detected in the SMA survey presented here, L1448C (see Appendix A.1) and IRAM 04191 (see Appendix A.8), are missing in their PdBI A-configuration (the most extended configuration) observations due to the low flux-ratio sensitivity (only 0.6–0.9; see Maury et al. 2010). Therefore, taking both L1448C and IRAM 04191 into account, the re-calculated multiplicity frequency in their sample is actually 0.60, which is consistent with the multiplicity frequency derived in this SMA survey (0.64).

## 4.2. The Distribution of Separations

Figure 19 shows the distribution of separations for the Class 0 binary/multiple systems observed in this work (see Table 6). It must be noted that these separations, measured in the SMA (sub-) millimeter images, are the projected separations between the components in individual systems. However, as discussed by Reipurth & Zinnecker (1993), using reasonable statistical assumptions, one could convert the mean projected separation ( $l$ ) to the mean semi-major axis ( $a$ ) with the ratio of  $l/a \sim 0.79\text{--}0.85$  (see Reipurth & Zinnecker 1993 and references therein). We therefore consider that there is no significant error by assuming that the overall statistical distribution of observed projected binary separations is representative of the actual distribution of the semi-major axes. In this work, we do not use these ratios to convert observed projected separations to the ‘semi-major’ axes, and instead show the original results from the observations.

As shown in the top of Figure 19, the distribution of separations for Class 0 protostars shows a general trend in which the companion star fraction increases from wide separations to close separations. Quantitatively, the companion star fraction is  $0.42 \pm 0.09$  for separations from 50 AU to 1700 AU,  $0.27 \pm 0.08$  from 1700 AU to 3350 AU, and  $0.21 \pm 0.07$  from 3350 AU to 5000 AU. The median separation in this survey is 1800 AU. Previous large-scale surveys toward MS and PMS stars found that the distributions of separations could be well fitted with log-normal functions with peaks at less than 100 AU (see, e.g., Duquennoy & Mayor 1991 and Patience et al. 2002). As shown in the bottom of Figure 19, the distribution of separations for Class 0 protostars does not exhibit a log-normal like distribution, and

Table 6: Separations and mass ratios of binary/multiple systems observed in this work

Source	Separation ["]	Separation [AU]	$M_{\text{low}}/M_{\text{high}}$
L1448N (A, B)	$7.4 \pm 0.3$	1800	$0.21 \pm 0.06$
L1448N (A, NW)	$16.5 \pm 0.3$	4000	$0.50 \pm 0.15$
L1448C (N, S)	$7.0 \pm 0.5$	1700	$0.10 \pm 0.05$
PER 065 (A, B)	$3.9 \pm 0.4$	940	$0.25 \pm 0.10$
PER 065 (B, C)	$7.5 \pm 0.4$	1800	$0.73 \pm 0.22$
NGC1333 IRAS 2A (A1, A2)	$1.5 \pm 0.2$	360	$0.05 \pm 0.02$
NGC1333 SVS 13 (A, VLA3)	$5.0 \pm 0.3$	1200	$0.05 \pm 0.02$
NGC1333 SVS 13 (VLA3, B)	$10.4 \pm 0.3$	2500	$0.05 \pm 0.02$
NGC1333 SVS 13 (B, C)	$19.8 \pm 0.3$	4750	$0.11 \pm 0.03$
NGC1333 IRAS 4A (A1, A2)	$1.4 \pm 0.2$	340	$0.50 \pm 0.15$
NGC1333 IRAS 4 B/C	$10.5 \pm 0.2$	2500	$0.27 \pm 0.10$
IRAS03282+3035 (MMS1, MMS2)	$1.6 \pm 0.2$	400	$0.10 \pm 0.05$
Per-B1-b (N, S)	$17.4 \pm 0.5$	4200	$0.71 \pm 0.21$
HH 211 (SMM1, SMM2)	$0.31 \pm 0.02$	74	$0.30 \pm 0.10$
IC348 (MMS1, MMS2)	$9.8 \pm 0.4$	2350	$0.25 \pm 0.10$
<sup>a</sup> CB 17 (IRS, MMS)	$21.4 \pm 0.5$	5350	$0.57 \pm 0.17$
IRAM 04191+1522 (IRS, MMS)	$8.0 \pm 0.4$	1100	$0.56 \pm 0.17$
OMC3 MMS 6 (SMM1, SMM2)	$10.8 \pm 0.2$	4750	$0.41 \pm 0.12$
NGC2024 FIR 5 (SMM1, SMM2)	$4.1 \pm 0.2$	1800	$0.39 \pm 0.12$
HH 212 (SMM1, SMM2)	$0.53 \pm 0.05$	230	$0.08 \pm 0.03$
HH 212 (SMM1, SMM3)	$1.2 \pm 0.1$	530	$0.10 \pm 0.03$
<sup>b</sup> HH 25 (SMM1, SMM2)	$12.7 \pm 0.3$	5600	$0.84 \pm 0.25$
HH 25 (SMM2, SMM3)	$10.9 \pm 0.3$	4800	$0.35 \pm 0.10$
CG 30 (N, S)	$21.8 \pm 0.5$	4400	$0.38 \pm 0.11$
VLA 1623 (W, E)	$9.9 \pm 0.2$	1200	$0.20 \pm 0.06$
VLA 1623 (EA, EB)	$1.1 \pm 0.1$	130	$1.0 \pm 0.3$
IRAS16293–2422 (A, B)	$5.3 \pm 0.2$	640	$0.50 \pm 0.15$
IRAS16293–2422 (Aa, Ab)	$0.42 \pm 0.05$	50	$0.44 \pm 0.13$
L723 VLA2 (MMS1, MMS2)	$3.5 \pm 0.3$	1050	$1.0 \pm 0.3$
L1251B (IRS1, SMA-N)	$8.9 \pm 0.4$	2700	$0.35 \pm 0.11$
L1251B (SMA-N, SMA-S)	$8.4 \pm 0.4$	2500	$0.61 \pm 0.18$
L1251B (SMA-S, IRS2)	$15.6 \pm 0.4$	4700	$0.80 \pm 0.25$

<sup>a</sup> CB 17 is not regarded as a “bound” binary system in this work.

<sup>b</sup> The separation between sources SMM 1 and SMM 2 is beyond the limit of 5000 AU, and hence we regard HH 25 MMS as a binary system (SMM 2 and SMM 3).

rather shows a trend where most companions are found with separations around 1800 AU. We ascribe this distribution to the limited angular resolution of the SMA observations (i.e., the completeness limit of the survey, see below), which allowed us to mostly detect binary separations in the order of 1000 AU. Further higher angular resolution large-scale surveys toward Class 0 protostars are needed, in order to achieve a wider distribution of separations (from  $\sim 0.1$  AU to  $\sim 10^3$  AU) for protobinary systems.

To better understand the evolution of binary properties, it is important to compare the separation distribution of Class 0 protobinary systems with those derived for Class I, PMS, and MS binaries. Yet, it must be noted in advance that MS and PMS binaries, as well as Class I binaries, have been well studied over the past two decades thanks to the availability of both large samples and high angular resolution obtained with large optical/near-infrared telescopes. The sample size and angular resolution in this SMA survey are an order of magnitude less than the optical and near-infrared surveys. Therefore, large uncertainties may remain in our comparisons due to the small sample size and limited angular resolution in this work.

In a large-scale survey toward Class I YSOs, Connelley et al. (2008a, b) found the number of single, binary, triple, and quadruple stars is S:B:T:Q = 122:51:12:4, with separations ranging from about 50 AU to 5000 AU. Based on the large-scale survey of Duquennoy & Mayor (1991), with a similar separations range, the corresponding number found in solar-type MS stars is S:B:T:Q = 131:32:1:0 (see Connelley et al. 2008b). These two studies, which summarize the binary properties for Class I YSOs and MS stars, will be mainly used here for comparison, as their separation ranges basically match the observed separation range in this SMA survey. From these two large-scale surveys, the multiplicity frequency and companion star fraction are derived to be  $0.35 \pm 0.03$  and  $0.46 \pm 0.04$  for Class I YSOs, and  $0.20 \pm 0.03$  and  $0.21 \pm 0.03$  for MS stars, respectively. Despite the incompleteness in the SMA survey and the difference between the sample sizes, the multiplicity frequency ( $0.64 \pm 0.08$ ) and companion star fraction ( $0.91 \pm 0.05$ ) found in Class 0 protostars are 1.8 (for MF) and 2.0 (for CSF) times larger than the values found in Class I YSOs, and 3.2 (for MF) and 4.3 (for CSF) times larger than the values found in MS stars (see Figure 20). Furthermore, the observed fraction of high order multiple systems to binary systems in Class 0 protostars (7:14 or  $0.50 \pm 0.09$ ) is also larger than the fractions found in Class I YSOs ( $0.31 \pm 0.07$ ) and MS stars ( $0.03 \pm 0.01$ )<sup>12</sup>. To estimate how different the distribution of separations for Class 0 protostars is from those distributions for Class I YSOs and MS stars, we use the equation given by Brandeker et al. (2006) in their Appendix B2 to calculate the probability that the

---

<sup>12</sup>The estimated fraction from the whole sample of Duquennoy & Mayor (1991; from  $\sim 0.1$  AU to  $\sim 10^4$  AU) is about 20% (see also Tokovinin 2004).

results in a given separation range from two studies are consistent with each other. Using this method, the probabilities that Class 0 protostars have the same distribution of separations as Class I YSOs and MS stars are estimated to be  $1.9 \times 10^{-6}$  and  $4.1 \times 10^{-15}$ , respectively.

The distributions of separations derived for PMS binaries are in general similar to those for Class I binaries (see, e.g., Connelley et al. 2008b). Therefore, we consider that the comparisons between Class 0 and PMS binaries will likely hold similar results to those derived from the comparisons between Class 0 and Class I binaries. Indeed, for example, in the survey toward PMS stars, Ghez et al. (1997) found a companion star fraction of  $0.21 \pm 0.04$  with separations from 150 AU to 1800 AU; with the same separation range, the companion star fraction found by Reipurth & Zinnecker (1993) is  $0.16 \pm 0.02$ . The companion star fraction derived from this survey with the same separation range is  $0.39 \pm 0.08$ , approximately two times higher, comparable to the ratios estimated between the Class 0 and Class I binaries.

As we indicated in § 4.1, this SMA survey is incomplete across the observed separation range, and the derived multiplicity frequency and companion star fraction in this work should be considered as lower limits. Therefore, the ratios estimated above should also be considered as lower limits. Considering that the median separation in this SMA survey is 1800 AU (larger than the lowest linear resolution in the survey of 1500 AU), the survey can be regarded to be complete for protobinary systems with separations from 1800 AU to 5000 AU. Since, to our knowledge, this work is the first large-scale observational survey of multiplicity in Class 0 protostars, the distribution of protobinary systems with smaller separations is not yet known. Hence, it is difficult to correct for our incompleteness to derive an accurate multiplicity frequency or companion star fraction for Class 0 protobinary systems with separations between 50 AU and 1800 AU. Nevertheless, we may adopt a simple method to ‘correct’ for completeness in this work. For separations smaller than 1800 AU, we assume that the completeness in a separation range is given by the averaged fraction of the sources in the total sample that have linear resolutions intermediate between the higher and lower limits of the range. For example, 55% of the sample has a resolution better than the median resolution of 600 AU, then we assume that we only detect  $\frac{55\%+100\%}{2}$  of the total number of multiple systems in the range between 600 AU and 1800 AU. Using this method, the multiplicity frequency and companion star fraction are derived to be  $0.33 \pm 0.08$  and  $0.42 \pm 0.08$  for systems with separations from 1800 AU to 5000 AU (100% completeness),  $0.15 \pm 0.06$  and  $0.24 \pm 0.07$  for systems with separations from 600 AU to 1800 AU (78% completeness), while  $0.15 \pm 0.06$  and  $0.24 \pm 0.07$  for systems with separations from 50 AU to 600 AU (32% completeness). After correcting for completeness, the overall multiplicity frequency and companion star fraction in this SMA survey are  $1.0 \pm 0.1$  and  $1.5 \pm 0.2$ , respectively, over the separation range from 50 AU to 5000 AU. Compared to the data derived from Class I YSOs survey (Connelley et al. 2008a, b), these ‘corrected’ values, result in a difference, in both the multiplicity frequency

and the companion star fraction, of a factor of three between Class 0 protostars and Class I YSOs, which is indeed larger than the factor of two estimated above. However, it must be noted that these ‘corrected’ values are uncertain. Further high angular resolution large-scale surveys toward Class 0 protostars are needed, in order to draw a real statistically significant separation distribution for close protobinary systems.

The decrease in both the multiplicity frequency and companion star fraction, as well as the fraction of high order multiple systems, suggests that binary properties change as stars evolve from the Class 0 to Class I/PMS, all the way to the MS phases. As reviewed by Goodwin et al. (2007), the evolution of binary properties has been ascribed to two main mechanisms: (1) the rapid dynamical decay of young small- $N$  systems ( $2 < N < 12$ ; see, e.g., Reipurth 2000; Reipurth & Clarke 2001; Goodwin & Kroupa 2005); and (2) dynamical destruction of loose binary systems in dense clusters (see, e.g., Kroupa 1995). Here, we consider that small- $N$  decay is likely the main process for the evolution of binary properties, because (1) most sources in this sample, as well as those in the Class I, PMS, and MS surveys discussed above, are not in dense cluster environments, and (2) the time scale for the decrease in binary fraction caused by destruction in dense cluster (a few 10 Myr) is much greater than the lifetimes of Class 0 protostars ( $\sim 10^4$ – $10^5$  yr) and Class I YSOs ( $\sim 10^5$  yr). As estimated by Goodwin et al. (2007), a triple system is unstable to decay with a general half-life of a few  $10^4$  yr, which is consistent with the lifetime estimated for Class 0 protostars. Thus, most of the decays/ejections are expected to happen during the Class 0 phase (e.g., Reipurth 2000). This small- $N$  decay will modify the binary properties by reducing the overall multiplicity frequency and companion star fraction, and reducing the fraction of high order multiple systems to binary systems. All have been evidenced by the comparisons between this work and previous large-scale surveys toward Class I and MS/PMS binaries.

In short, we find that approximately two-thirds of Class 0 protostars are binary or multiple systems in this SMA survey, and this could only be a lower limit to the fraction of Class 0 protostars formed in such systems. The results derived from this work, in concert with the comparison between this survey and large surveys toward Class I and MS/PMS binaries, is consistent with the possibility that most, if not all, stars are formed in binary or multiple systems and that single stars result from the decay of multiple systems, as suggested by Larson (1972).

### 4.3. The Distribution of Mass Ratios

We have derived the circumstellar gas masses for the sources in the sample using the (sub-) millimeter dust continuum emission (see Section 3 and Tables 4 & 5). We note that

these values are uncertain and generally cannot be compared among the sources in the sample, because different sources were observed differently (i.e., with different angular resolution, *uv*-coverage, and different resulting sensitivity), which probe different size scales and amounts of material. Relative masses between components within individual systems are more reliable. Assuming, for simplicity, that sources in a multiple system have similar temperatures, then we can obtain the circumstellar mass ratio from the continuum emission flux ratio of the sources (see Equations 1-3). Table 6 lists the circumstellar mass ratios of the binary/multiple systems observed in this work, under the assumption that the circumstellar mass is proportional to the (sub) millimeter continuum flux. It must be noted that this circumstellar mass ratio does not necessarily reflect the mass ratio of the hydrostatic cores nor that of the final stars, but still provides a valuable comparison between the components in these systems. Figure 21 shows the distribution of circumstellar mass ratios for the protobinary systems in this work. The distribution appears to be flat like that of more evolved long-period PMS and MS binary stars (see, e.g., Reipurth & Zinnecker 1993; Halbwachs et al. 2003). We find that  $67\% \pm 8\%$  of protobinary systems have circumstellar mass ratios below 0.5, i.e., unequal masses systems are more common than equal masses systems in the sample. This result suggests that unequal-mass systems may be preferred in the process of (wide) binary star formation (separations on the order of 1000 AU).

Figure 22 shows the distribution of circumstellar mass ratios versus separations. The distribution is somewhat scattered, similar to the distribution of PMS binaries (see, e.g., Reipurth & Zinnecker 1993). Numerical simulations predict that close binary systems (separations on the order of 1 AU) are likely to have mass ratios near unity (see Bate 2000), which is indirectly supported by statistical studies of MS binary systems (see, e.g., Halbwachs et al. 2003). However, we do not find this trend in Figure 22. It is probably because (1) the sample size in this work is still small, and (2) we cannot resolve close binary systems in which components may prefer similar masses.

#### 4.4. Sequential Fragmentation in Star Formation

Different physical processes at different evolutionary stages may trigger different fragmentation processes (e.g., Tohline 2002; Machida et al. 2008). At different evolutionary stages, the varying properties of a collapsing core (e.g., core temperature and density) will result in different fragmentation scales. As introduced in Section I, depending on the evolution of a collapsing core, fragmentation models can be divided into initial fragmentation, prompt (isothermal) fragmentation, adiabatic fragmentation and secondary fragmentation. Suggested by these models, the fragmentation of a core could take place sequentially during

the core’s different collapsing phases, which would result in a hierarchical system eventually. However, it is yet unclear whether the fragmentation at one specific phase is dominant over other phases, and whether most collapsing cores go through all these fragmentation processes. Based on the extensive single-dish and interferometric observations, we show in Figure 23 a suggested sequential fragmentation picture. This is a rough outline and further efforts are needed to collect corresponding samples and to derive their kinematical properties, in order to understand the fragmentation mechanisms at different core’s collapse phases in detail.

The initial fragmentation of a large-scale clump or filament ( $\sim 0.1\text{--}1.0\,\text{pc}$ ) occurs before the collapse of individual prestellar cores, and results in cores with separations of about  $10^3\text{--}10^4\,\text{AU}$ . This large-scale fragmentation has been frequently observed with single-dish millimeter telescopes (see, e.g., Kauffmann et al. 2008; Launhardt et al. 2010), and it is likely controlled by the combined effects of gravity and turbulence. Figure 23 shows a possible example of the initial clump fragmentation, CB 246 (see Launhardt et al. 2010 for more details), where the extended large-scale clump has fragmented into separated cores. These cores are invisible in the *Spitzer Space Telescope (Spitzer)* infrared images and may represent the prestellar cores which will further collapse and fragment.

Most of the protobinary systems that have been observed with current millimeter arrays have separations in scales of  $1000\,\text{AU}$  (e.g., Looney et al. 2000, and this work). These systems appear to support the scenario of prompt fragmentation, which occurs at the end of the isothermal collapse phase (see Tohline 2002). Nevertheless, these observed systems are mostly made of Class 0 objects that have already gone through the fragmentation process, and thus these systems do not exhibit the initial conditions of a fragmenting core. An observational example representing the prompt fragmentation may be the prestellar core R CrA SMM 1A (see Figure 23), in which multiple faint condensations were discovered with separations between  $1000\,\text{AU}$  and  $2000\,\text{AU}$ . These condensations are invisible in the deep infrared images, have extremely low bolometric luminosities ( $< 0.1 L_\odot$ ) and temperatures ( $< 20\,\text{K}$ ), indicating that these are young sources have yet to form protostars, and therefore represent the earliest phase of core fragmentation observed (see Chen & Arce 2010 for more details). More recently, based on the kinematic data collected at different interferometric arrays, Chen et al. (2012a) found that most protostellar cores with binary systems (separations scale  $\sim 1000\,\text{AU}$ ) formed therein have ratios of rotational energy to gravitational energy  $\beta_{\text{rot}} > 1\%$ , which is consistent with theoretical simulations (see, e.g., Boss 1999). This suggests that the level of rotational energy in a dense core plays an important role in the prompt fragmentation process.

Unfortunately, there is a lack of observations of protobinary systems with separations between  $10\,\text{AU}$  and  $100\,\text{AU}$ , which could be used to study the adiabatic fragmentation sce-

nario (see Machida et al. 2008). This can be easily explained by the fact that current millimeter interferometers (e.g., SMA and PdBI) normally reach 1–2 $''$  angular resolution under general conditions, and thus mostly resolve protobinary systems with separations of 100–200 AU or larger in nearby star-forming clouds (e.g., Perseus and Ophiuchus). In Figure 23, we show the eSMA 850  $\mu$ m image of source IRAS 16293A, which represents the best angular resolution that can be achieved at the SMA. In IRAS 16293 A, a close binary system with a separation of 50 AU is revealed (see also Appendix A.19). We speculate that the close binary system in IRAS 16293A was formed through adiabatic fragmentation, which took place after the initial clump fragmentation (that formed the IRAS 16293 and IRAS 16293 E cores; see, e.g., Figure 8 in Jørgensen et al. 2008) and the prompt (isothermal) fragmentation (that formed the IRAS 16293 A-B system; see Figure 15d). We note that the protobinary system VLA 1623 (see Appendix A.17 and Figures 15a-b) may show another example of adiabatic fragmentation. Here, the VLA 1623 system appears to have fragmented from the Oph-A core through initial clump fragmentation and have later fragmented into VLA 1623 West & East (through prompt fragmentation); VLA1623 East seems to have subsequently gone through adiabatic fragmentation to form VLA 1623 East A and B. As we discussed in Appendix A.17, source VLA 1623 B could also be a binary system, which needs to be verified by further higher angular resolution observations.

We believe that routine observations at angular resolution better than 0 $.''1$  will reveal more multiple protobinary systems with smaller separations, which will then allow us to study in detail a statistically significant number of protostellar binary/multiple systems with a wide range of separations (from 1 AU to  $10^4$  AU). The Atacama Large Millimeter/submillimeter Array (ALMA), capable of attaining an angular resolution down to 10 mas (when fully completed), will provide a breakthrough in our knowledge of binary star formation. It will certainly help us find closer protobinary systems with separations in the scale of 1–10 AU, and will even allow us to test the secondary fragmentation scenario (see, e.g., Machida et al. 2008), by which stellar systems with separations of 0.01–0.1 AU can be formed.

## 5. SUMMARY

We present SMA 1.3 mm and 850  $\mu$ m dust continuum data toward a sample of 33 Class 0 protostars in nearby clouds (distance  $< 500$  pc), which thus far represents the largest survey toward protostellar binary/multiple systems. The median angular resolution in the survey is 2 $.''5$ , while the median linear resolution is approximately 600 AU. The main results of this work are summarized below.

- (1) Compact millimeter and/or submillimeter dust continuum emission is detected from

all sources in the sample, which likely originates from the inner envelope and/or circumstellar disk. The measured 1.3 mm fluxes in the sample range from 1.1 mJy to 3.0 Jy, with a median value of 100 mJy, while the 850  $\mu$ m fluxes range from 20 mJy to 3.2 Jy, with a median value of 430 mJy. Assuming that the 1.3 mm and 850  $\mu$ m dust continuum emission is optically thin and a dust temperature of 30 K for all sources, the estimates of the total gas masses are in the ranges of  $0.001\text{--}2.4 M_{\odot}$  at  $\lambda 1.3 \text{ mm}$  and of  $0.005\text{--}1.7 M_{\odot}$  at  $\lambda 850 \mu\text{m}$ .

(2) Twenty-one sources in the sample show signatures of binarity/multiplicity, with separations ranging from 50 AU to 5000 AU. Of them, four sources are newly-discovered binary/multiple candidates (PER 065, NCG 1333 IRAS 2A, IC 348 MMS, and HH 25 SMM). Quantitatively, the numbers of singles, binaries, triples, and quadruples in the sample are 12, 14, 5, and 2, respectively. The estimated multiplicity frequency and companion star fraction are  $0.64 \pm 0.08$  and  $0.91 \pm 0.05$ , respectively, with no correction for completeness. We consider these values as lower limits, as it is likely that there are unresolved binary/multiple systems with small ( $< 600 \text{ AU}$ ) separations in this survey.

(3) The derived multiplicity frequency and companion star fraction for Class 0 protostars are approximately two times higher than those values found in the binary surveys toward Class I YSOs and pre-main sequence stars, and approximately three (for multiplicity frequency) and four (for companion star fraction) times larger than the values found among main sequence stars, with a similar range of separations. Furthermore, the observed fraction of high order multiple systems to binary systems in Class 0 protostars ( $0.50 \pm 0.09$ ) is also larger than the fractions found in Class I YSOs ( $0.31 \pm 0.07$ ) and main sequence stars ( $\leq 0.2$ ). The decrease in both the multiplicity frequency/companion star fraction and the fraction of high order multiple systems clearly suggests that binary properties evolve as protostars evolve, as predicted by numerical simulations.

(4) The distribution of separations for Class 0 protostars shows a general trend in which the companion star fraction increases with decreasing companion separation. Quantitatively, the companion star fraction is  $0.42 \pm 0.09$  for separations from 50 AU to 1700 AU,  $0.27 \pm 0.08$  from 1700 AU to 3350 AU, and  $0.21 \pm 0.07$  from 3350 AU to 5000 AU, with no correction for completeness. The median separation in this survey is 1800 AU (larger than the lowest linear resolution), and thus the survey is regarded to be complete for protobinary systems with separations from 1800 AU to 5000 AU (over this separation range the multiplicity frequency and companion star fraction are  $0.33 \pm 0.08$  and  $0.42 \pm 0.08$ , respectively). After correcting for incompleteness for separations less than 1800 AU with a simple method, the overall multiplicity frequency and companion star fraction in this survey are  $1.0 \pm 0.1$  and  $1.5 \pm 0.2$ , respectively, over the separation range from 50 AU to 5000 AU.

(5) The distribution of circumstellar mass ratios for the protobinary systems in this

survey appears to be flat, like that of more evolved long-period main-sequence and pre-main sequence binary stars. We find that  $67\% \pm 8\%$  of the protobinary systems have circumstellar mass ratios below 0.5 (i.e., unequal masses are much more common than equal masses). This implies that unequal-mass systems are preferred in the process of binary star formation (with separations in the scale of 1000 AU).

(6) The high angular resolution survey in this work, in concert with previous extensive single-dish observations, strongly support that the fragmentation of molecular cloud cores, at different core collapse phases, is the main mechanism for the formation of binary/multiple stars. Based on these observations, we suggest an empirical sequential fragmentation picture for binary star formation.

We thank the anonymous referee for providing many insightful suggestions and comments, which helped us improve this work greatly. We thank the SMA staff for technical support during the observations and their maintenance of the SMA archival data. X.C. acknowledges the support of the Thousand Young Talents Program of China. This material is based on work supported by NSF grant AST-0845619 to H.G.A. JEP has received funding from the European Community’s Seventh Framework Programme (/FP7/2007-2013/) under grant agreement No 229517.

## A. DESCRIPTION OF INDIVIDUAL SOURCES

In this Appendix, we provide a brief description of the individual sources, and discuss their SMA results in more detail. We note that, for sources L1448C, NGC 1333 IRAS 2A & 2B, NGC 1333 IRAS 4A & 4B, L1527, L483, B335, and L1157, the SMA results (dust continuum and molecular lines) were presented by Jørgensen et al. (2007). The dust continuum results (images and fluxes) derived independently in this work are comparable with those in Jørgensen et al. (2007). We refer readers to that paper for more details on the line data of these sources. Other sources for which their SMA data have been published elsewhere include: HH 211 MMS (Lee et al. 2007b; 2009; 2010), NGC 2024-FIR5 (Alves et al. 2011), HH 212 MMS (Lee et al. 2006; 2007a; 2008), L723 VLA2 (Girart et al. 2009), and L1251B (J. Lee et al. 2006; 2007).

### A.1. L1448 Region

L1448 is a dark globule located on the west end of the Perseus cloud, which has been observed extensively in the past two decades (see, e.g., Bally et al. 2008, and references therein). Figure 3a shows the SCUBA 850  $\mu\text{m}$  image of the L1448 region. The region contains three well-known Class 0 protostars: L1448 IRS2, L1448 N, and L1448C (see, e.g., Barsony et al. 1998; O’Linger et al. 2006).

**L1448 IRS2** was suggested to be a protobinary candidate (with a 10 $''$  separation) by Wolf-Chase et al. (2000) based on the NRAO-12 m CO (1-0) observations that mapped two distinct molecular outflows from IRS2. Volgenau et al. (2002) also claim the detection of a binary system in IRS2 using BIMA, but no results (e.g., spatial separation or image) have been presented yet. However, the SMA 1.3 mm dust continuum observations with an angular resolution of 3. $''$ 4  $\times$  2. $''$ 5 (see Figure 3c), as well as *Spitzer* infrared observations (e.g., Chen et al. 2010), do not find any companions around IRS2 (see also O’Linger et al. 2006). We therefore conclude that L1448 IRS2 is a single protostar.

**L1448 N** is also referred to as L1448 IRS3 by several authors. However, we prefer using the name L1448 N, because the IRAS source IRS3 in fact consists of two protostars, L1448 N and L1448C (see O’Linger et al. 2006). L1448 N is the brightest source at infrared and millimeter wavelengths in L1448, and has been resolved into three distinct sources by previous interferometric observations (e.g., Looney et al. 2000). The three sources are named L1448 NA, L1448 NB, and L1448 NW (O’Linger et al. 2006). The SMA 1.3 mm dust continuum image of L1448 N shows these three distinct sources (see Figure 3b). The dust continuum emission is dominated by source NB, which is located 7. $''$ 4  $\pm$  0. $''$ 3 south of

source NA. Source L1448 NW, located approximately  $20''$  northwest of the NA-NB pair, has relatively weaker dust continuum emission in the interferometric observations.

**L1448C**, also known as L1448-mm, is one of the best-studied Class 0 protostars. L1448C is well-known for driving a young, highly collimated, and high-velocity bipolar outflow (e.g., Bachiller et al. 1990; Hirano et al. 2010). *Spitzer* infrared observations resolved L1448C into two separated components, with an angular separation of about  $8''$  (see Jørgensen et al. 2006). The SMA observations at both  $850\,\mu\text{m}$  and  $1.3\,\text{mm}$  continuum bands detect these two components (see Figures 3d & 3e). The dust continuum emission is dominated by the northern component, and only weak dust continuum emission is found from the southern component ( $5\sigma$  detection). The northern component is the driving source of the well-known high-velocity bipolar outflow (Jørgensen et al. 2007; Hirano et al. 2010). Maury et al. (2010) argued that the southern component is not a protostar but a dusty clump associated with the outflow driven by the northern component. However, we note that a relatively low-velocity bipolar outflow associated with the southern component has been found in the SMA CO (2–1) observations (see Jørgensen et al. 2007) and CO (3–2) observations (see Hirano et al. 2010), which clearly indicates that the southern component is a protostellar object.

## A.2. PER 065

The protostellar core PER 065 was discovered by the dust continuum survey in the Perseus cloud, and was classified as a Class 0 protostar by Hatchell et al. (2007) and Enoch et al. (2009). Because of its low luminosity ( $0.03\text{--}0.22\,L_\odot$ ), it was also cataloged as one of the very low luminosity objects (VeLLOs) in Perseus (No. 065; see Dunham et al. 2008). The SMA  $1.3\,\text{mm}$  dust continuum observations resolve, for the first time, the faint core into three components, named A, B, and C, respectively (see Figure 4). The separations between components A and B and between B and C are  $3''.9 \pm 0''.4$  and  $7''.5 \pm 0''.4$ , respectively.

## A.3. NGC 1333 Region

NGC 1333 is a well-studied protostellar cluster located in the western part of the Perseus cloud (see, e.g., a review by Walawender et al. 2008 and references therein, and Arce et al. 2010). Submillimeter and millimeter dust continuum observations have revealed several protostellar cores within the region (see, e.g., Sandell & Knee 2001), of which three cores, SVS 13, IRAS 2, and IRAS 4 are the most well-known and studied (see Figure 5a).

Figure 5b shows the SMA  $1.3\,\text{mm}$  continuum image of **SVS 13**, in which three distinct

sources, referred to as A, B, and C, are found. The SMA results are consistent with the results found in other high angular resolution observations (e.g., Bachiller et al. 1998; Looney et al. 2000; Chen et al. 2009). Another weak continuum source, which is spatially coincident with the radio source VLA 3 (Rodríguez et al. 1997) and the 3 mm dust continuum source detected by Looney et al. (2000) and Chen et al. (2009), is found in the SMA 1.3 mm dust continuum image (see Figure 5c). Also note that, with the VLA centimeter observations, Anglada et al. (2000; 2004) resolved source A into a close binary system with an angular separation of  $0''.3$ .

The SMA continuum images of **IRAS 2** and **IRAS 4** are shown in Figures 5d & 5e and Figures 5f & 5g, respectively. The continuum results of the two sources derived independently in this work are comparable with those in Jørgensen et al. (2007). We therefore refer readers to that work for more details about the SMA results. We note that IRAS 2A is resolved into two separated components in the high angular resolution  $850 \mu\text{m}$  image (see Figure 5e), with a faint companion  $1''.5 \pm 0''.2$  to the north of the main dust peak. In the CO observations, a quadrupolar outflow centered at IRAS 2A was detected (see, e.g., Jørgensen et al. 2007). This quadrupolar outflow is likely two different outflows driven by the two binary components in IRAS 2A. Further high angular resolution observations are needed to confirm the tentative detection of the faint secondary source in IRAS 2A and to distinguish which source drives which outflow.

#### A.4. IRAS 03282+3035

IRAS 03282+3035 (IRAS 03282) is a young Class 0 protostar located in the western part of the Perseus cloud, which has been studied by various groups using different molecular line transitions (see, e.g., Bachiller et al. 1991, 1994; Arce & Sargent 2006; Chen et al. 2007; Tobin et al. 2011).

The OVRO 1.3 mm dust continuum observations (at  $0''.9 \times 0''.7$  resolution) revealed two millimeter sources in IRAS 03282, with an angular separation of  $1''.5$  (see Launhardt 2004). Although the SMA 1.3 mm observations (at  $2''.5 \times 2''.2$ ) do not resolve the two components, the SMA  $850 \mu\text{m}$  observations (at  $0''.9 \times 0''.8$ ) show two separated components (see Figure 6). We refer to the main continuum source as MMS 1 and the faint source as MMS 2. In the SMA images, the angular separation between the two sources is  $1''.6 \pm 0''.2$ , similar to the result found in the OVRO 1.3 mm images.

### A.5. Perseus B1-c and B1-b

Barnard 1 (B1) is a dark cloud in the western part of Perseus. Single-dish dust continuum observations have revealed four protostellar cores in this cloud (see, e.g., Matthews & Wilson 2002, Hatchell et al. 2005, and Enoch et al. 2006), which are commonly referred to as B1-a, -b, -c, and -d (see Figure 7a).

The Class 0 protostar **B1-c** was studied with BIMA by Matthews et al. (2006). The BIMA 3.3 mm dust continuum observations (at  $6''.4 \times 4''.9$  resolution) revealed a protostellar envelope with radius of  $\sim 2400$  AU and mass of  $2.1\text{--}2.9 M_{\odot}$ . The SMA 1.3 mm dust continuum observations, with higher angular resolution ( $3''.4 \times 2''.9$ ), resolve an inner envelope with radius of  $700 \pm 100$  AU and mass of  $0.24 \pm 0.05 M_{\odot}$  (see Figure 7b).

The **B1-b** protostellar core is elongated in the north-south direction in the SCUBA images (see Figure 7a). The 3 mm dust continuum observations at the Nobeyama Millimeter Array (NMA) found two separate sources in the B1-b core, referred to as B1-bN and B1-bS (Hirano et al. 1999). The SMA 1.3 mm observations show similar results to those found by Hirano et al. (1999): the two sources are separated by  $17''.4 \pm 0''.5$  and have similar circumstellar masses (mass ratio  $0.7 \pm 0.2$ ).

### A.6. IC 348 MMS and HH 211 MMS

**IC 348 MMS** is a Class 0 protostar discovered in the southwestern part of the IC 348 cluster (see Eislöffel et al. 2003). It drives a collimated molecular outflow, traced by H<sub>2</sub> emission (Eislöffel et al. 2003) and CO emission (Tafalla et al. 2006). The SMA 1.3 mm dust continuum images of IC 348 MMS reveal, for the first time, two sources embedded in the common envelope detected by single-dish dust continuum observations (see Figure 8b). The angular separation between the two sources is  $9''.8 \pm 0''.4$ , and the mass ratio is  $0.25 \pm 0.10$ . The main continuum source MMS 1 is the driving source of the collimated molecular outflow.

The Class 0 protostar **HH 211 MMS** is well-known for driving a highly collimated bipolar outflow, which has a narrow bipolar jet-like component in the high-velocity CO/SiO emission and a relatively wide-angle bipolar cavity in the low-velocity CO emission (see, e.g., Gueth & Guilloteau 1999; Hirano et al. 2006; Lee et al. 2007b).

Based on very high angular resolution SMA observations (at  $0''.20 \times 0''.15$ ), Lee et al. (2009) found that HH 211 MMS actually contains two dust continuum sources, SMM 1 and SMM 2, with an angular separation of  $0''.31 \pm 0''.02$  (see Figure 8c). Source SMM 1 appears to be the driving source of the collimated jet/outflow, while the nature of source SMM 2, which

has a mass of only  $1.5\text{--}4 M_{\text{Jup}}$ , is still uncertain. More interestingly, based on the reflection-symmetric wiggle of the HH 211 jet, Lee et al. (2010) suggested that source SMM 1 itself could be a very low mass protobinary with a separation of  $\sim 4.6$  AU (the putative 4.6 AU companion was not directly detected, but inferred from the morphology of the outflow). Further higher angular resolution observations are needed to confirm this interesting tentative detection. More details about HH 211 MMS and its surrounding envelope can be found in Gueth & Guilloteau (1999), Lee et al. (2007b; 2009; 2010), and Tanner & Arce (2011).

### A.7. CB 17

CB 17 (also known as L1389) is a small, isolated, and slightly cometary-shaped dark cloud, which was classified as a Bok globule by Clemens & Barvainis (1988). CB 17 has been studied by various groups using different molecular line transitions (e.g., Pavlyuchenkov et al. 2006) and multi-wavelength dust continuum emission (e.g., Launhardt et al. 2010).

The SMA 1.3 mm dust continuum observations reveal two sources within CB 17, which are separated by  $21''.4 \pm 0''.5$  in the northwest-southeast direction (see Figure 9a). The northwestern dust continuum source is associated with an infrared source seen in the *Spitzer* images and is referred to as CB 17 IRS (see Chen et al. 2012b). No compact infrared emission is detected from the southeastern source in the *Spitzer* bands from 3.6 to  $70\,\mu\text{m}$ , and we refer to this source as CB 17 MMS. Interestingly, the SMA CO (2–1) observations suggest that source CB 17 MMS, an object with an extremely low bolometric luminosity ( $\leq 0.04 L_{\odot}$ ), is driving a low velocity ( $\sim 2.5\,\text{km}\,\text{s}^{-1}$ ) molecular outflow. These characteristics have lent this source to be classified as a candidate of the so-called first hydrostatic cores (see Chen et al. 2012b for more details).

### A.8. IRAM 04191+1522

IRAM 04191+1522 (IRAM 04191) is a well-studied Class 0 protostar located in the southern part of the Taurus molecular cloud (André et al. 1999). IRAM 04191 drives a large bipolar molecular outflow, features bright molecular line and dust continuum emission, and shows evidences of supersonic infall, fast rotation, depletion, and deuteration (see, e.g., André et al. 1999; Belloche et al. 2002; Belloche & André 2004; Lee et al. 2005).

The SMA 1.3 mm dust continuum observations reveal two distinct continuum sources with an angular separation of  $8''.0 \pm 0''.4$ , embedded within the elongated core of IRAM 04191 (see Figure 9b). The discovery of this binary system was reported by Chen et al. (2012a).

The southeastern source, associated with an infrared source seen in the *Spitzer* images (see Dunham et al. 2006), represents the well-known Class 0 protostar and is referred to as IRAM 04191 IRS here. In contrast, the northwestern source has no infrared emission detected in the *Spitzer* images, and is referred to as IRAM 04191 MMS (see Chen et al. 2012a for more details).

#### A.9. L1521F-IRS and L1527-IRS

L1521F is a well-studied dense core in Taurus. This core shows high central density, infall asymmetry, molecular depletion, and enhanced deuterium fractionation, and was suggested as a highly evolved starless core by Crapsi et al. (2004). However, *Spitzer* observations found that L1521F harbors a very low luminosity protostar, referred to as **L1521F-IRS** (see Bourke et al. 2006), which is in the early stage of the Class 0 phase (Shinnaga et al. 2009; Terebey et al. 2009). The SMA 1.3 mm dust continuum observations of L1521F-IRS show a faint source (see Figure 9c). More than 95% of the flux around L1521F-IRS is resolved out by the SMA observations, compared to the flux detected in the IRAM-30m 1.2 mm maps ( $600 \pm 150$  mJy; Bourke et al. 2006). We also note that L1521F-IRS was observed at higher angular resolution with the IRAM-PdBI by Maury et al. (2010). In the PdBI 1.3 mm dust continuum images, there is also only one object detected.

**L1527-IRS** is another protostar in Taurus, which is associated with a far-infrared source and is probably more evolved than L1521F-IRS (see, e.g., Terebey et al. 2009). Based on the JCMT 800  $\mu\text{m}$  continuum observations, Fuller et al. (1996) suggested L1527-IRS is a binary system with the secondary at about  $20''$  from the main protostar. However, no evidence is found of this secondary source in the SMA 1.3 mm dust continuum image (see Figure 9d). We therefore conclude that L1527-IRS is a single protostar (see also Maury et al. 2010).

#### A.10. HH 114 MMS

HH 114 MMS is a Class 0 protostar located in the western part of the  $\lambda$  Orionis molecular shell, which drives a highly collimated bipolar outflow (see Arce & Sargent 2006). In the SMA 1.3 mm and 880  $\mu\text{m}$  dust continuum images (see Figure 10), source HH 114 MMS remains as a single object at the angular resolution of  $2''.2 \times 1''.9$ , which is consistent with the OVRO 2.7 mm and 3.4 mm continuum observations (Arce & Sargent 2006).

### A.11. OMC3 MMS 6

The MMS 6 core is the brightest source in submillimeter and millimeter wavelengths in the Orion molecular cloud-3 (OMC-3) region (Chini et al. 1997; Lis et al. 1998; Johnstone & Bally 1999). The SMA 850  $\mu\text{m}$  continuum images show two sources in the MMS 6 core, referred to as SMM 1 and SMM 2, with an angular separation of  $10''.8 \pm 0''.2$  (see Figure 11a). The northern continuum source SMM 1 is spatially coincident with a continuum source detected in early interferometric observations (see Matthews et al. 2005; Takahashi et al. 2009). The southern continuum source SMM 2 is associated with a continuum source detected in the BIMA 1.3 mm observations by Matthews et al. (2005), but it was not detected in the multi-wavelength observations by Takahashi et al. (2009). We note that source MMS 6 was also observed in the SMA 0.9 mm continuum by Takahashi et al. (2009), but the sensitivity in their image was about 2 times worse than that in the SMA 850  $\mu\text{m}$  image presented here.

### A.12. NGC 2024 FIR 5

FIR 5 is a Class 0 protostar located in the NGC 2024 cloud, the most active star-forming region in the Orion B cloud (see, e.g., a review by Meyer et al. 2008 and references therein). With a high velocity, collimated molecular outflow extending over 5' south of the core (Richer et al. 1992), FIR 5 is the brightest and also probably most evolved protostellar core among the dense cores in NGC 2024 (Mezger et al. 1992).

In the SMA 850  $\mu\text{m}$  continuum images, the FIR 5 core is resolved into two main components, referred to as SMM 1 and SMM 2, with an angular separation of  $4''.1 \pm 0''.2$  (see Figure 11b). The SMA results are consistent with the results derived from the PdBI 3 mm continuum observations, in which the FIR 5 core was also resolved into two main components (see Wiesemeyer et al. 1997). Nevertheless, in the BIMA 1.3 mm deep observations, Lai et al. (2002) also found several weaker dust condensations around the two main components, which are not detected in the SMA images. We note that the SMA results of FIR 5 (including also dust polarization and CO emission results) were independently published by Alves et al. (2011), and similar dust continuum results were derived there.

### A.13. HH 212 MMS

HH 212 is a remarkable jet in the Orion L1630 cloud, discovered by Zinnecker et al. (1998). The jet is associated with a bipolar molecular outflow seen in CO lines (see, e.g.,

Lee et al. 2000; 2006; 2007a) and SiO lines (see, e.g., Codella et al. 2007; Lee et al. 2008). The driving source of the jet/outflow, referred to as HH 212 MMS, is a low-luminosity Class 0 protostar associated with a cold IRAS source (IRAS 05413-0104; Zinnecker et al 1992).

The SMA 1.3mm and 850  $\mu\text{m}$  dust continuum images of HH 212 MMS were shown by Lee et al. (2006; 2007a; 2008). By re-analyzing the high angular resolution 850  $\mu\text{m}$  images in Lee et al. (2008; angular resolution  $0''.35 \times 0''.32$ ), a faint continuum component is found to the west of source HH 212 MMS (see Figure 12c). Hereafter, we refer to the main dust continuum component as MMS 1 and to the faint continuum component as MMS 2. The separation between the two components is measured to be  $0''.53 \pm 0''.05$ . We also retrieved the SMA 230 GHz data of HH 212 MMS obtained in the Extended and Very Extended configurations (the 230 GHz data published by Lee et al. 2006 were obtained only in the Compact configuration). The high angular resolution 1.3 mm dust continuum images (angular resolution  $0''.8 \times 0''.7$ ) show that source HH 212 MMS is extended in the east-west direction and a component is tentatively detected in the 1.3 mm images, which is spatially associated with the new component MMS 2 seen in the 850  $\mu\text{m}$  images (see Figure 12d).

We also note that another dust continuum source was tentatively detected in the PdBI 1.4 mm continuum observations, which is about  $1''.7$  to the southeast of the main dust continuum source MMS 1 (see Codella et al. 2007). In the SMA 850  $\mu\text{m}$  images, a weak dust continuum source ( $\sim 7\sigma$  detection) is seen near this PdBI 1.4 mm source but  $0''.6$  closer to the main continuum source MMS 1. We referred to this weak continuum source as MMS 3 (see Figure 12c). Altogether, there may be three dust continuum sources found within the elongated envelope of HH 212 MMS. Further high angular observations are needed to confirm this tentative multiple system detection.

#### A.14. HH 25 MMS

The protostellar jet HH 25 is located in the northern part of the Orion B dark cloud. The jet is associated with a compact but collimated molecular outflow (e.g., Gibb & Davis 1998; Gibb et al. 2004). The driving source of the jet/outflow, referred to as HH 25 MMS, was revealed by a VLA 3.6 cm survey in this region (Bontemps et al. 1995), and was classified as a Class 0 protostar with a luminosity of  $\sim 6 L_\odot$  (Gibb & Davis 1998).

In the single-dish dust continuum maps (IRAM-30m, Lis et al. 1999; JCMT/SCUBA, Phillips et al. 2001), HH 25 MMS is elongated in the north-south direction, with the VLA source located at the northern tip of the extension. In the SMA 870  $\mu\text{m}$  dust continuum image, three distinct, previously unknown sources are revealed within the large-scale elon-

gated core, approximately aligned in the north-south direction (see Figure 13a). The three continuum sources, from north to south, are referred to as SMM 1, SMM 2, and SMM 3. The angular separations between sources SMM 1 and SMM 2 and between sources SMM 2 and SMM 3 are measured to be  $12''.7 \pm 0''.3$  and  $10''.9 \pm 0''.3$ , respectively. Source SMM 1 is spatially coincident with the VLA 3.6 cm source, and is the driving source of the HH 25 jet/outflow.

### A.15. CG 30

CG 30 (also known as BHR 12; Bourke et al. 1995) is a bright-rimmed cometary globule located in the Gum Nebula region. In the SCUBA submillimeter (Henning et al. 2001) and ATCA 3 mm (Chen et al. 2008a) continuum observations, this globule was resolved into a wide protobinary system with an angular separation of  $\sim 22''$ .

The SMA 1.3 mm dust continuum image of CG 30 shows two compact sources (see Figure 13b). The angular separation between the two sources is measured to be  $21''.8 \pm 0''.5$ , consistent with the ATCA result. Following Chen et al. (2008a), we refer to the northern source as CG 30N (which is spatially coincident with IRAS 08076–3556) and to the southern source as CG 30S. The two sources each drive their own bipolar protostellar jets/outflows, which are roughly perpendicular to each other (see Chen et al. 2008a, b). Further discussion of the gas kinematics (from ATCA N<sub>2</sub>H<sup>+</sup> and SMA CO observations) and infrared emission (from *Spitzer* observations) in CG 30 can be found in Chen et al. (2008a, b).

### A.16. B228

B228 is a Class 0 protostar located in the Lupus I cloud (Shirley et al. 2000). It drives a compact bipolar molecular outflow that extends in the northeast-southwest direction (see van Kempen et al. 2009). In the SMA dust continuum images, an elongated source is seen at both 1.3 mm and 1.1 mm (see Figure 14). The source is extended in the southwest direction, roughly following the direction of the blueshifted outflow lobe, suggesting that the outflow has a strong impact on the dust envelope, similar to L1157 (see, e.g., Gueth et al. 2003).

### A.17. VLA 1623

VLA 1623 is the prototypical Class 0 protostar (André et al. 1993), which drives a large scale bipolar outflow (Dent et al. 1995; Yu & Chernin 1997). With VLA centimeter continuum observations, Bontemps & André (1997) found a series of emission clumps, named

A, B, and C. At high angular resolution, clump A was further resolved into two components (Bontemps & André 1997; Looney et al. 2000).

In the SMA high angular resolution images (resolution  $0''.6 \times 0''.3$ ; observed in 2007), three distinct dust continuum sources are detected (see Figure 15a). The three sources, aligning roughly from east to west, are referred to as VLA 1623 A, VLA 1623 B, and VLA 1623 West, respectively. Sources A and B, the east pair with an angular separation of  $1''.1 \pm 0''.1$  (see Figure 15b), are spatially coincident with the BIMA 2.7 mm sources A and B in Looney et al. (2000) and the two VLA centimeter sources in clump A in Bontemps & André (1997). The mass ratio between sources A and B is close to  $1.0 \pm 0.3$ , similar to the result found by Looney et al. (2000). Source VLA 1623 West, located approximately  $10''$  to the east of the A-B pair, is spatially coincident with clump B in Bontemps & André (1997).

More recently, Maury et al. (2012) presented high angular resolution SMA data of VLA 1623 (observed in 2009) and argued that sources VLA 1623 B and VLA 1623 West are two dusty knots due to shocks along the outflow cavity wall of source VLA 1623 A (although they did not show any evidence that VLA 1623 A is the driving source of the VLA 1623 outflow). However, in the *Spitzer* mid-infrared images, source VLA 1623 West is associated with a point-like infrared source, strongly suggesting that it is a young stellar object (X. Chen et al. in preparation). Furthermore, the SMA CO (2–1) data show a quadrupolar outflow centered at source VLA 1623 B, indicating that this source is not only a protostellar object but also a potential close binary system unresolved in the current SMA dust continuum observations (X. Chen et al., in preparation).

### A.18. Oph-MMS 126 (IRAS 16253–2429)

Oph-MMS 126 is a Class 0 protostar discovered in the SEST 1.2 mm continuum survey toward the  $\rho$  Ophiuchi molecular cloud, which is associated with a faint, cold IRAS source (IRAS 16253–2429) and drives a low-velocity bipolar molecular outflow (see Stanke et al. 2006). In the SMA images, a faint dust continuum source is seen (about  $5\sigma$  detection; see Figure 15c), which is associated with an infrared source seen in the *Spitzer* images (see Barsony et al. 2010). The total flux was measured to be  $11 \pm 2$  mJy in the SMA 1.3 mm dust continuum images. Compared with the total flux obtained in the SEST observations (411 mJy; Stanke et al. 2006), more than 97% of the dust continuum emission flux from the large envelope was resolved out by the SMA.

### A.19. IRAS 16293–2422

IRAS 16293–2422 (IRAS 16293) is a well-studied Class 0 protostar located in the  $\rho$  Ophiuchi cloud. Millimeter interferometric observations resolved this source into a binary system, referred to as IRAS 16293 A and B, with a separation of  $5''.2$  (see, e.g., Mundy et al. 1992; Loony et al. 2000). In the high angular resolution VLA radio continuum observations, source A is further resolved into a chain of radio components (see Loinard et al. 2007a; Pech et al. 2010), which are suggested to be related to a jet from source A. Recent ALMA Science verification data revealed an inverse P-Cygni profile towards source B, which is direct evidence of infalling material close to the central protostar (Pineda et al. 2012).

Figure 15d shows the SMA 1.3 mm continuum image of IRAS 16293, in which two continuum sources, A and B, are detected with an angular separation of  $5''.3 \pm 0''.2$ . In the higher angular resolution eSMA 850  $\mu\text{m}$  images, source A is further resolved into two close continuum sources (see Figure 15e). The separation between the two sources is  $0''.42 \pm 0''.05$ . Following Chandler et al. (2005), the two sources are referred to as Aa and Ab.

### A.20. L483

L483 is an isolated dense core, associated with a strong infrared source (IRAS 18148–0440). It was classified as a Class 0/I transition object by Tafalla et al. (2000). High angular resolution molecular line observations found a cold, quiescent core in L483 (see Jørgensen 2004). In the SMA 850  $\mu\text{m}$  dust continuum observations, source L483 remains as single object at the angular resolution of  $2''.6 \times 1''.9$  (see Figure 16), which is consistent with previous interferometric millimeter continuum observations (see, e.g., Jørgensen 2004).

### A.21. L723 VLA 2

L723 is a small isolated dark cloud. At the center of the cloud core is an IRAS point source (IRAS 19156+1906), which was classified as a Class 0 protostar with a bolometric luminosity  $L_{\text{bol}} \sim 3.0 L_{\odot}$  and a circumstellar mass  $M_{\text{env}} \sim 1.2 M_{\odot}$  (Shirley et al. 2000). Anglada et al. (1991) detected two radio continuum sources (VLA 1 and VLA 2) with  $15''$  separation, both located within the error ellipse of the IRAS position. However, only VLA 2 was found to be associated with dense gas in the cloud core (Girart et al. 1997).

Figure 17a shows the SMA 1.3 mm dust continuum images of L723 VLA 2, in which two separated compact sources (labeled MMS 1 and MMS 2) are revealed. The angular separation

( $3\rlap{.}''5 \pm 0\rlap{.}''3$ ) and mass ratio ( $1.0 \pm 0.3$ ) between the two sources derived in the SMA images are consistent with the results derived earlier in the OVRO 3 mm continuum observations (see Launhardt 2004). The two close compact sources are embedded in a common envelope seen in the SCUBA 850  $\mu$ m observations. We note that the SMA data of L723 VLA 2 (including molecular lines results) have been published by Girart et al. (2009). Also note that VLA 7 mm continuum observations discovered two components in source MMS 2 with an angular separation of  $\sim 1''$  (see Carrasco-González et al. 2008), which would be unresolved by the SMA observations presented here.

### A.22. B335 and L1157

**B335** is a well-studied, isolated Class 0 protostar, and is widely accepted as one of the best protostellar collapse candidates (see, e.g., Zhou et al. 1993; Evans et al. 2005). It drives a large-scale bipolar outflow extending in the east-west direction (see, e.g., Jørgensen et al. 2007). **L1157** is also a well-studied, isolated Class 0 protostar, and is well-known for its prominent outflow. This outflow shows rich chemistry in various molecular lines observations (see, e.g., Bachiller et al. 2001; Arce et al. 2008), and is commonly considered the prototypical chemically active outflow. In the SMA 1.3 mm dust continuum observations, both B335 and L1157 remain as single sources (see Figure 17b & 17c), which is consistent with previous high angular resolution continuum observations toward the two sources (see, e.g., Harvey et al. 2003 for B335 and Chiang et al. 2010 for L1157).

### A.23. L1251B

L1251B is a small protostellar group located at  $300 \pm 50$  pc (Kun & Prusti 1993). It is associated with an IRAS point source (IRAS 22376+7455), and was found to be associated with a CO outflow by Sato & Fukui (1989). Using OVRO and SMA (as well as single-dish telescopes), J. Lee et al. (2006; 2007) presented multiple-line observations toward L1251B, which shows very complex kinematics, including infall, rotation, and outflow motions.

The SMA 1.3 mm dust continuum observations show four distinct sources embedded in the common envelope seen in the single-dish observations. Following J. Lee et al. (2007), the four sources are named L1251B IRS1, IRS2, SMA-N, and SMA-S (see Figure 17d). Both IRS1 and IRS2 are associated with the infrared sources seen in the *Spitzer* images, and were classified as Class 0/I transition objects by J. Lee et al. (2006). Sources SMA-N and SMA-S have weak 1.3 mm dust continuum emission (see Figure 17d) and are not detected in the

*Spitzer* images, and are likely still in the early stages of the Class 0 phase (see J. Lee et al. 2007 for more details).

## REFERENCES

- Alves, F. O., Girart, J. M., Lai, S.-P., Rao, R., & Zhang, Q. 2011, ApJ, 726, 63
- André, P., Basu, S., and Inutsuka, S.-I. 2009, in Structure Formation in Astrophysics, ed. G. Chabrier (Cambridge: Cambridge University Press), 254
- André, P., Motte, F., & Bacmann, A. 1999, ApJ, 513, L57
- André, P., Ward-Thompson, D., & Barsony, M. 1993, ApJ, 406, 122
- André, P., Ward-Thompson, D., & Barsony, M. 2000, in Protostars and Planets IV, ed. V. Mannings, A. P. Boss, & S. S. Russell (Tucson, AZ: Univ. Arizona Press), 59
- Anglada, G., Estalella, R., Rodríguez, L. F., et al. 1991, ApJ, 376, 615
- Anglada, G., Rodríguez, L. F., Osorio, M., et al. 2004, ApJ, 605, L137
- Anglada, G., Rodríguez, L. F., & Torrelles, J. M. 2000, ApJ, 542, L123
- Arce, H. G., Borkin, M. A., Goodman, A. A., Pineda, J. E., & Beaumont, C. N. 2011, ApJ, 742, 105
- Arce, H. G., Borkin, M. A., Goodman, A. A., Pineda, J. E., & Halle, M. W. 2010, ApJ, 715, 1170
- Arce, H. G., Santiago-García, J., Jørgensen, J. K., Tafalla, M., & Bachiller, R. 2008, ApJ, 681, L21
- Arce, H. G., & Sargent, A. I. 2006, ApJ, 646, 1070
- Bachiller, R., André, P., & Cabrit, S. 1991, A&A, 241, L43
- Bachiller, R., Guilloteau, S., Gueth, F., et al. 1998, A&A, 339, L49
- Bachiller, R., Martin-Pintado, J., Tafalla, M., Cernicharo, J., & Lazareff, B. 1990, A&A, 231, 174
- Bachiller, R., Pérez Gutiérrez, M., Kumar, M. S. N., & Tafalla, M. 2001, A&A, 372, 899
- Bachiller, R., Terebey, S., Jarrett, T., et al. 1994, ApJ, 437, 296
- Bally, J., Walawender, J., Johnstone, D., Kirk, H., & Goodman, A. 2008, in Handbook of Star Forming Regions, Volume I: The Northern Sky, ASP Monograph Publications, Vol. 4. ed, Reipurth, B., 308

- Barsony, M., Ward-Thompson, D., André, P., & O’Linger, J. 1998, ApJ, 509, 733
- Barsony, M., Wolf-Chase, G. A., Ciardi, D. R., & O’Linger, J. 2010, ApJ720, 64
- Bate, M. R. 2000, MNRAS, 314, 33
- Bate, M. R., & Bonnell, I. A. 1997, MNRAS, 285, 33
- Belloche, A., & André, P. 2004, A&A, 419, L35
- Belloche, A., André, P., Despois, D., & Blinder, S. 2002, A&A, 393, 927
- Bodenheimer, P., Burkert, A., Klein, R. I., & Boss, A. P. 2000, in Protostars and Planets IV, ed. V. Mannings, A. P. Boss, & S. R. Russell (Tucson, AZ: Univ. Arizona Press), 675
- Bontemps, S., & André, P. 1997, in IAU Symposium 182, Herbig-Haro Flows and the Birth of Stars, ed. B. Reipurth & C. Bertout (Kluwer Academic Publishers), 63
- Bontemps, S., André, P., & Ward-Thompson, D. 1995, A&A, 297, 98
- Boss, A. P. 1999, ApJ, 520, 744
- Bourke, T. L., Hyland, A. R., & Robinson, G. 1995, MNRAS, 276, 1052
- Bourke, T. L., Myers, P. C., Evans, N. J., II, et al. 2006, ApJ, 649, L37
- Brandeker, A., Jayawardhana, R., Khavari, P., Haisch, K. E., Jr., & Mardones, D. 2006, ApJ, 652, 1572
- Carrasco-González, C., Anglada, G., Rodríguez, L. F., et al. 2008, ApJ, 676, 1073
- Černis, K. 1990, Ap&SS, 166, 315
- Černis, K., & Straižys, V. 2003, Baltic Astronomy, 12, 301
- Chabrier, G. 2005, in Astrophysics and Space Science Library, Vol. 327, The Initial Mass Function 50 Years Later, ed. E. Corbelli, F. Palla, & H. Zinnecker, 41
- Chandler, C. J., Brogan, C. L., Shirley, Y. L., & Loinard, L. 2005, ApJ, 632, 371
- Chandler, C. J., & Richer, J. S. 2000, ApJ, 530, 851
- Chen, X., & Arce, H. G., 2010, ApJ, 720, L169
- Chen, X., Arce, H. G., Dunham, M. M., & Zhang, Q. 2012a, ApJ, 747, L43

- Chen, X., Arce, H. G., Dunham, M. M., et al. 2012b, ApJ, 751, 89
- Chen, X., Arce, H. G., Zhang, Q., et al. 2010, ApJ, 715, 1344
- Chen, X., Bourke, T. L., Launhardt, R., & Henning, Th., 2008b, ApJ, 686, L107
- Chen, X., Launhardt, R., & Bourke, T. L., Henning, Th., & Barnes, P. J. 2008a, ApJ, 683, 862
- Chen, X., Launhardt, R., & Henning, Th. 2007, ApJ, 669, 1058
- Chen, X., Launhardt, R., & Henning, Th. 2009, ApJ, 691, 1729
- Chiang, H.-F., Looney, L. W., Tobin, J. J., & Hartmann, L. 2010, ApJ, 709, 470
- Chini, R., Reipurth, B., Ward-Thompson, D., et al. 1997, ApJ, 474, L135
- Clemens, D. P., & Barainis, R. 1988, ApJS, 68, 257
- Codella, C., Cabrit, S., Gueth, F., et al. 2007, A&A, 462, L53
- Connelley, M. S., Reipurth, B., & Tokunaga, A. T. 2008a, AJ, 135, 2496
- Connelley, M. S., Reipurth, B., & Tokunaga, A. T. 2008b, AJ, 135, 2526
- Crapsi, A., Caselli, P., Walmsley, C. M., et al. 2004, A&A, 420, 957
- Dame, T. M. & Thaddeus, P. 1985, ApJ, 297, 751
- Delfosse, X., Beuzit, J.-L., & Marchal, L. et al. 2004, in Spectroscopically and Spatially Resolving the Components of the Close Binary Stars, ed. R. W. Hilditch, H. Hensberge & K. Pavlovski. ASP Conference Series, Vol. 318, 166
- Dent, W. R. F., Matthews, H. E., & Walther, D. M. 1995, MNRAS, 277, 193
- Duchêne, G., Bouvier, J., Bontemps, S., André, P., & Motte, F. 2004, A&A, 427, 651
- Duchêne, G., Delgado-Donate, E., Haisch, K. E., Loinard, L., and Rodríguez, L. 2007, in Protostars and Planets V, ed. B. Reipurth, D. Jewitt, & K. Keil (Tucson, AZ: Univ. Arizona Press), 379
- Dunham, M. M., Crapsi, A., Evans, N. J., II, et al. 2008, ApJS, 179, 249
- Dunham, M. M., Evans, N. J., II, Bourke, T. L., et al. 2006, ApJ, 651, 945
- Duquennoy, A., & Mayor, M. 1991, A&A, 248, 485

- Eislöffel, J., Froebrich, D., Stanke, T., & McCaughrean, M. J. 2003, ApJ, 595, 259
- Elias, J. H. 1978, ApJ, 224, 857
- Enoch, M. L., Evans, N. J., II, Sargent, A. I., & Glenn, J. 2009, ApJ, 692, 973
- Enoch, M. L., Young, K. E., Glenn, J., et al. 2006, ApJ, 638, 293
- Evans, N. J., II, Dunham, M. M., Jørgensen, J. K., et al. 2009, ApJS, 181, 321
- Evans, N. J., II, Lee, J.-E., Rawlings, J. M. C., & Choi, M. 2005, ApJ, 626, 919
- Fischer, D. A., & Marcy, G. W. 1992, ApJ, 396, 178
- Froebrich, D. 2005, ApJS, 156, 169
- Fuller, G. A., Ladd, E. F., & Hodapp, K.-W. 1996, ApJ, 463, L97
- Ghez, A. M., McCarthy, D. W., Patience, J. L., & Beck, T. L. 1997, ApJ, 481, 378
- Ghez, A. M., Neugebauer, G., & Matthews, K. 1993, AJ, 106, 2005
- Gibb, A. G., & Davis, C. J. 1998, MNRAS, 298, 644
- Gibb, A. G., Richer, J. S., Chandler, C. J., & Davis, C. J. 2004, ApJ, 603, 198
- Girart, J. M., Estalella, R., Anglada, G., et al. 1997, ApJ, 489, 734
- Girart, J. M., Rao, R., & Estalella, R. 2009, ApJ, 694, 56
- Goldsmith, P. F., Snell, R. L., Hemeon-Heyer, M., & Langer, W. D. 1984, ApJ, 286, 599
- Gomez, M., Hartmann, L., Kenyon, S. J., & Hewett, R. 1993, AJ, 105, 1927
- Goodwin, S. P., & Kroupa, P. 2005, A&A, 439, 565
- Goodwin, S., Kroupa, P., Goodman, A., & Burkert A. 2007, in Protostars and Planets V, ed. B. Reipurth, D. Jewitt, & K. Keil (Tucson, AZ: Univ. Arizona Press), 133
- Gueth, F., Bachiller, R., & Tafalla, M. 2003, A&A, 401, L5
- Gueth, F., & Guilloteau, S. 1999, A&A, 343, 571
- Haisch, K. E., II., Greene, T. P., Barsony, M., & Stahler, S. W. 2004, AJ, 127, 1747
- Halbwachs, J. L., Mayor, M., Udry, S., & Arenou, F. 2003, A&A, 397, 159

- Harvey, D. W. A., Wilner, D. J., Myers, P. C., & Tafalla, M. 2003, ApJ, 596, 383
- Hatchell, J., Fuller, G. A., & Richer, J. S. 2007, A&A, 472, 187
- Hatchell, J., Richer, J. S., Fuller, G. A., et al. 2005, A&A, 440, 151
- Henning, Th., Wolf, S., Launhardt, R., & Waters, R. 2001, ApJ, 561, 871
- Herbig, G. H. & Jones, B. F. 1983, AJ, 88, 1040
- Hirano, N., Ho, P. P. T., Liu, S.-Y., et al. 2010, ApJ, 717, 58
- Hirano, N., Kamazaki, T., Mikami, H., Ohashi, N., & Umemoto, T. 1999, in Proc. Star Formation 1999, ed. T. Nakamoto (Nagoya: Nobeyama Radio Observatory), 181
- Hirano, N., Liu, S.-Y., & Shang, H., et al. 2006, ApJ, 636, L141
- Hirota, T., Bushimata, T., Choi, Y. K., et al. 2007, PASJ, 59, 897
- Hirota, T., Bushimata, T., Choi, Y. K., et al. 2008, PASJ, 60, 37
- Hirota, T., Honma, M., Imai, H., et al. 2011, PASJ, 63, 1
- Ho, P. T. P., Moran, J. M., & Lo, K. Y. 2004, ApJ, 616, L1
- Johnstone, D., & Bally, J. 1999, ApJ, 510, L49
- Jørgensen, J. K. 2004, A&A, 424, 589
- Jørgensen, J. K., Bourke, T. L., Myers, P. C., et al. 2007, ApJ, 659, 479
- Jørgensen, J. K., Harvey, P. M., Evans, N. J., II, et al. 2006, ApJ, 645, 1246
- Jørgensen, J. K., Johnstone, D., Kirk, H., et al. 2008, ApJ, 683, 822
- Jørgensen, J. K., van Dishoeck, E. F., Visser, R., et al. 2009, A&A, 507, 861
- Kauffmann, J., Bertoldi, F., Bourke, T. L., Evans, N. J., II, & Lee, C. W. 2008, A&A, 487, 993
- Kenyon, S. J., Dobrzycka, D., & Hartmann, L. 1994, AJ, 108, 1872
- Knude, J., Jønch-Sørensen, H., & Nielsen, A. S. 1999, A&A, 350, 985
- Köhler, R., & Leinert, Ch. 1998, A&A, 331, 977
- Kroupa, P. 1995, MNRAS, 277, 1491

- Kroupa, P. 2002, Science, 295, 82
- Kun, M. & Prusti, T. 1993, A&A, 272, 235
- Lada, C. J. 1987, in IAU Symposium 115, Star Formation Regions, ed., M. Peimbert & J. Jugaku (Dordrecht: Reidel), 1
- Lada, C. J. 2006, ApJ, 640, L63
- Lai, S.-P., Crutcher, R. M., Girart, J. M., & Rao, R. 2002, ApJ, 566, 925
- Larson, R. B. 1972, MNRAS, 156, 437
- Larson, R. B. 1995, MNRAS, 272, 213
- Launhardt, R. 2004, in IAU Symp. 221, Star Formation at High Angular Resolution, ed. M. G. Burton, R. Jayawardhana, & T. L. Bourke (San Francisco, CA: ASP), 213
- Launhardt, R., Nutter, D., Ward-Thompson, D., et al. 2010, ApJS, 188, 139
- Lee, C.-F., Hasegawa, T. I., Hirano, N., et al. 2010, ApJ, 713, 731
- Lee, C.-F., Hirano, N., Palau, A., Ho, P. T. P., & Bourke, T. L. 2009, ApJ, 699, 1584
- Lee, C.-F., Ho, P. T. P., Beuther, H., et al. 2006, ApJ, 639, 292
- Lee, C.-F., Ho, P. T. P., Bourke, T. L., et al. 2008, ApJ, 685, 1026
- Lee, C.-F., Ho, P. T. P., Hirano, N., et al. 2007a, ApJ, 659, 499
- Lee, C.-F., Ho, P. T. P., Palau, A., et al. 2007b, ApJ, 670, 1188
- Lee, C.-F., Ho, P. T. P., & White, S. M. 2005, ApJ, 619, 948
- Lee, C.-F., Mundy, L. G., Reipurth, B., Ostriker, E. C., & Stone, J. M. 2000, ApJ, 542, 925
- Lee, J.-E., Di Francesco, J., Bourke, T. L., Evans, N. J., II, & Wu, J. 2007, ApJ, 671, 1748
- Lee, J.-E., Di Francesco, J., Lai, S.-P., et al. 2006, ApJ, 648, 491
- Lis, D. C., Menten, K. M., & Zylka, R. 1999, ApJ, 527, 856
- Lis, D. C., Serabyn, E., Keene, J., et al. 1998, ApJ, 509, 299
- Loinard, L., Torres, R. M., Mioduszewski, A. J., & Rodríguez, L. F. 2008, ApJ, 675, L29
- Loinard, L., Chandler, C. J., Rodríguez, L. F., et al. 2007a, ApJ, 670, 1353

- Loinard, L., Torres, R. M., Mioduszewski, A. J., et al. 2007b, ApJ, 671, 546
- Looney, L. W., Mundy, L. G., & Welch, W. J. 2000, ApJ, 529, 477
- Machida, M. N., Matsumoto, T., Hanawa, T., & Tomisaka, K. 2005, MNRAS, 362, 382
- Machida, M. N., Tomisaka, K., Matsumoto, T., & Inutsuka, S.-I. 2008, ApJ, 677, 327
- Masunaga, H., & Inutsuka, S.-I. 2000, ApJ, 531, 350
- Mathieu, R. D. 1994, ARA&A, 32, 465
- Matthews, B. C., & Wilson, C. D. 2002, ApJ, 574, 822
- Matthews, B. C., Hogerheijde, M. R., Jørgensen, J. K., & Bergin, E. A. 2006, ApJ, 652, 1374
- Matthews, B. C., Lai, S.-P., Crutcher, R. M., & Wilson, C. D. 2005, ApJ, 626, 959
- Maury, A. J., André, Ph., Hennebelle, P., et al. 2010, A&A, 512, 40
- Maury, A. J., Ohashi, N., & André, Ph. 2012, A&A, 539, 130
- McKee, C. F., & Ostriker, E. C. 2007, ARA&A, 45, 565
- Meyer, M. R., Flaherty, K., Levine, J. L. et al. 2008, in Handbook of Star Forming Regions, Volume I: The Northern Sky, ASP Monograph Publications, Vol. 4. ed, Reipurth, B., 662
- Mezger, P. G., Sievers, A. W., Haslam, C. G. T., et al. 1992, A&A, 256, 631
- Mundy, L. G., Wootten, A., Wilking, B. A., Blake, G. A., & Sargent, A. I. 1992, ApJ, 385, 306
- Murphy, D. C.; Cohen, R., & May, J. 1986, A&A, 167, 234
- O'Linger, J. C., Cole, D. M., Ressler, M. E., & Wolf-Chase, G. 2006, AJ, 131, 2601
- Ossenkopf, V., & Henning, Th. 1994, A&A, 291, 943
- Patience, J., Ghez, A. M., Reid, I. N., & Matthews, K. 2002, AJ, 123, 1570
- Pavlyuchenkov, Ya., Wiebe, D., Launhardt, R., & Henning, Th. 2006, ApJ, 645, 1212
- Pech, G., Loinard, L., Chandler, C. J., et al. 2010, ApJ, 712, 1403

- Phillips, R. R., Gibb, A. G., & Little, L. T. 2001, MNRAS, 326, 927
- Pineda, J. E., Maury, A. J., Fuller, G. A., et al. 2012, A&A, 544, L7
- Qi, C. 2005, MIR Cookbook (Cambridge: Harvard), <http://cfa-www.harvard.edu/~cqi/mircook.html>
- Reipurth, B. 2000, AJ, 120, 3177
- Reipurth, B., & Clarke C. 2001, AJ, 122, 432
- Reipurth, B., Mikkola, S., Connelley, M., & Valtonen, M. 2010, ApJ, 725, L56
- Reipurth, B., Jewitt, D., & Keil, K. 2007, ed., Protostars and Planets V (Univ. Arizona Press)
- Reipurth, B., Rodríguez, L. F., Anglada, G., & Bally, J. 2002, AJ, 124, 1045
- Reipurth, B., & Zinnecker, H. 1993, A&A, 278, 81
- Richer, J. S., Hills, R. E., & Padman, R. 1992, MNRAS, 254, 525
- Ridge, N. A., Di Francesco, J., Kirk, H., et al. 2006, AJ, 131, 2921
- Rodríguez, L. F. 2004, Revista Mexicana de Astronomia y Astrofisica Conference Series, 21, 93
- Rodríguez, L. F., Anglada, G., & Curiel, S. 1997, ApJ, 480, L125
- Sandell, G., & Knee, L. B. G. 2001, ApJ, 546, L49
- Sato, F., & Fukui, Y. 1989, ApJ, 343, 773
- Sault, R. J., Teuben, P. J., & Wright, M. C. H. 1995, in ASP Conf. Ser. 77, Astronomical Data Analysis Software and Systems IV, ed. R. A. Shaw, H. E. Payne, & J. J. E. Hayes (San Francisco, CA: ASP), 443
- Shinnaga, H., Phillips, T. G., Furuya, R. S., & Kitamura, Y. 2009, ApJ, 706, L226
- Shirley, Y. L., Evans, N. J., II, Rawlings, J. M. C., & Gregersen, E. M. 2000, ApJS, 131, 249
- Shu, F. H., Adams, F. C., & Lizano, S. 1987, ARA&A, 25, 23
- Siegler, N., Close, L. M., Cruz, K. L., Martin, E. L., & Reid, I. N. 2005, ApJ, 621, 1023
- Stanke, T., Smith, M. D., Gredel, R., & Khanzadyan, T. 2006, A&A, 447, 609

- Straizys, V., Černis, K., Kazlauskas, A., & Meištas, E. 1992, Baltic Astronomy, vol. 1, 149
- Tafalla, M., Kumar, M. S. N., Bachiller, R. 2006, A&A, 456, 179
- Tafalla, M., Myers, P. C., Mardones, D., & Bachiller, R. 2000, A&A, 359, 967
- Takahashi, S., Ho, P. T. P., Tang, Y.-W., Kawabe, R., & Saito, M. 2009, ApJ, 704, 1459
- Tanner, J. D., & Arce, H. G. 2011, ApJ, 726, 40
- Terebey, S., Fich, M., Noriega-Crespo, A., et al. 2009, ApJ, 696, 1918
- Tobin, J. J., Hartmann, L., Chiang, H.-F., et al. 2011, ApJ, 740, 45
- Tohline, J. E. 2002, ARA&A, 40, 349
- Tokovinin, A. 2004, Revista Mexicana de Astronomia y Astrofisica Conference Series, 21, 7
- Tomita, Y., Saito, T., & Ohtani, H. 1979, PASJ, 31, 407
- van Kempen, T. A., van Dishoeck, E. F., Güsten, R., et al. 2009, A&A, 507, 1425
- Volgenau, N., Mundy, L. G., Evans, N. J., II, et al. 2002, BAAS, 34, 1216
- Volgenau, N. H., Mundy, L. G., Looney, L. W., & Welch, W. J. 2006, ApJ, 651, 301
- Walawender, J., Bally, J., Francesco, J. D., Jørgensen, J., & Getman, K. 2008, in Handbook of Star Forming Regions, Volume I: The Northern Sky, ASP Monograph Publications, Vol. 4. ed, Reipurth, B., 346
- Wiesemeyer, H., Guesten, R., Wink, J. E., & Yorke, H. W. 1997, A&A, 320, 287
- Wolf-Chase, G. A., Barsony, M., & O'Linger, J. 2000, AJ, 120, 1467
- Yu, T., & Chernin, L. M. 1997, ApJ, 479, L63
- Zhou, S., Evans, N. J., II, Koempe, C., & Walmsley, C. M. 1993, ApJ, 404, 232
- Zinnecker, H., Bastien, P., Arcoragi, J.-P., & Yorke, H. W. 1992, A&A, 265, 726
- Zinnecker, H., McCaughrean, M. J., & Rayner, J. T. 1998, Nature, 394, 862

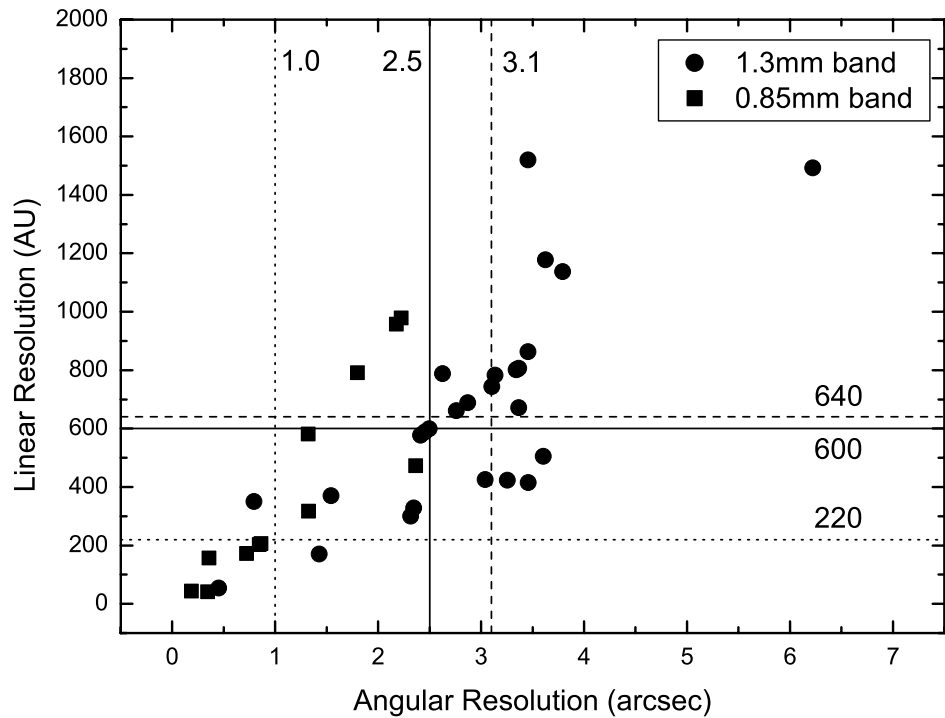


Fig. 1.— Distribution of angular resolutions and corresponding linear resolutions in this SMA survey. The dashed lines show the median values in the 1.3 mm continuum observations ( $3\rlap{.}^{\prime\prime}1$  and 640 AU), the dotted lines show the median values in the  $850 \mu\text{m}$  continuum observations ( $1\rlap{.}^{\prime\prime}0$  and 220 AU), while the solid lines show the median values for all observations ( $2\rlap{.}^{\prime\prime}5$  and 600 AU).

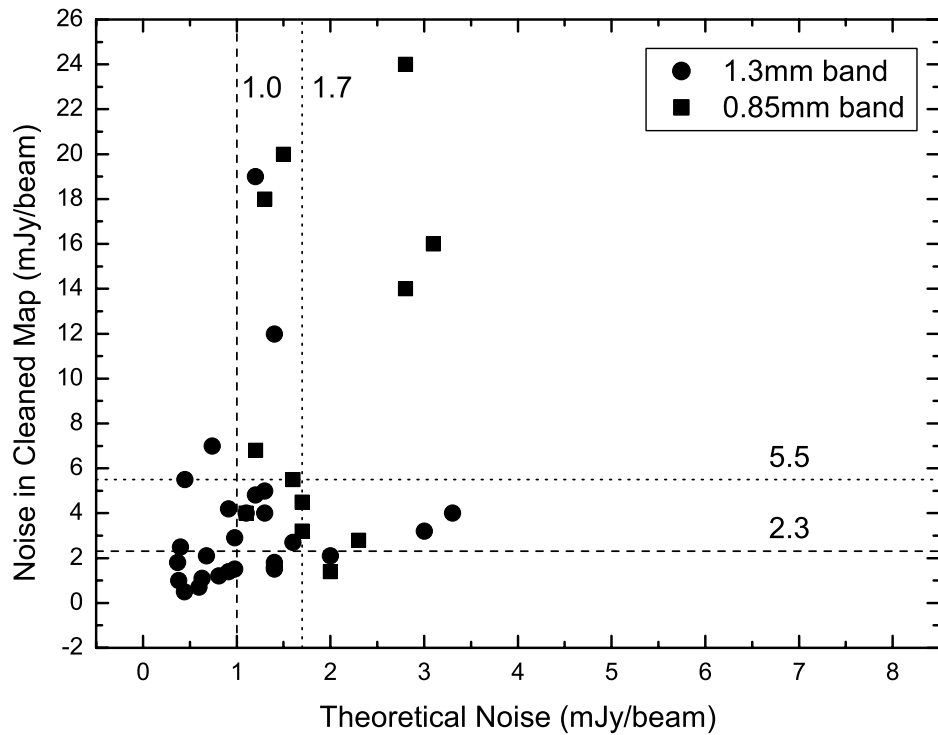


Fig. 2.— Distribution of  $1\sigma$  theoretical noises and  $1\sigma$  measured noises in cleaned maps in this SMA survey. The dashed lines show the median values in the 1.3 mm continuum observations ( $1.0$  and  $2.3 \text{ mJy beam}^{-1}$ ), and the dotted lines show the median values in the  $850 \mu\text{m}$  continuum observations ( $1.7$  and  $5.5 \text{ mJy beam}^{-1}$ ).

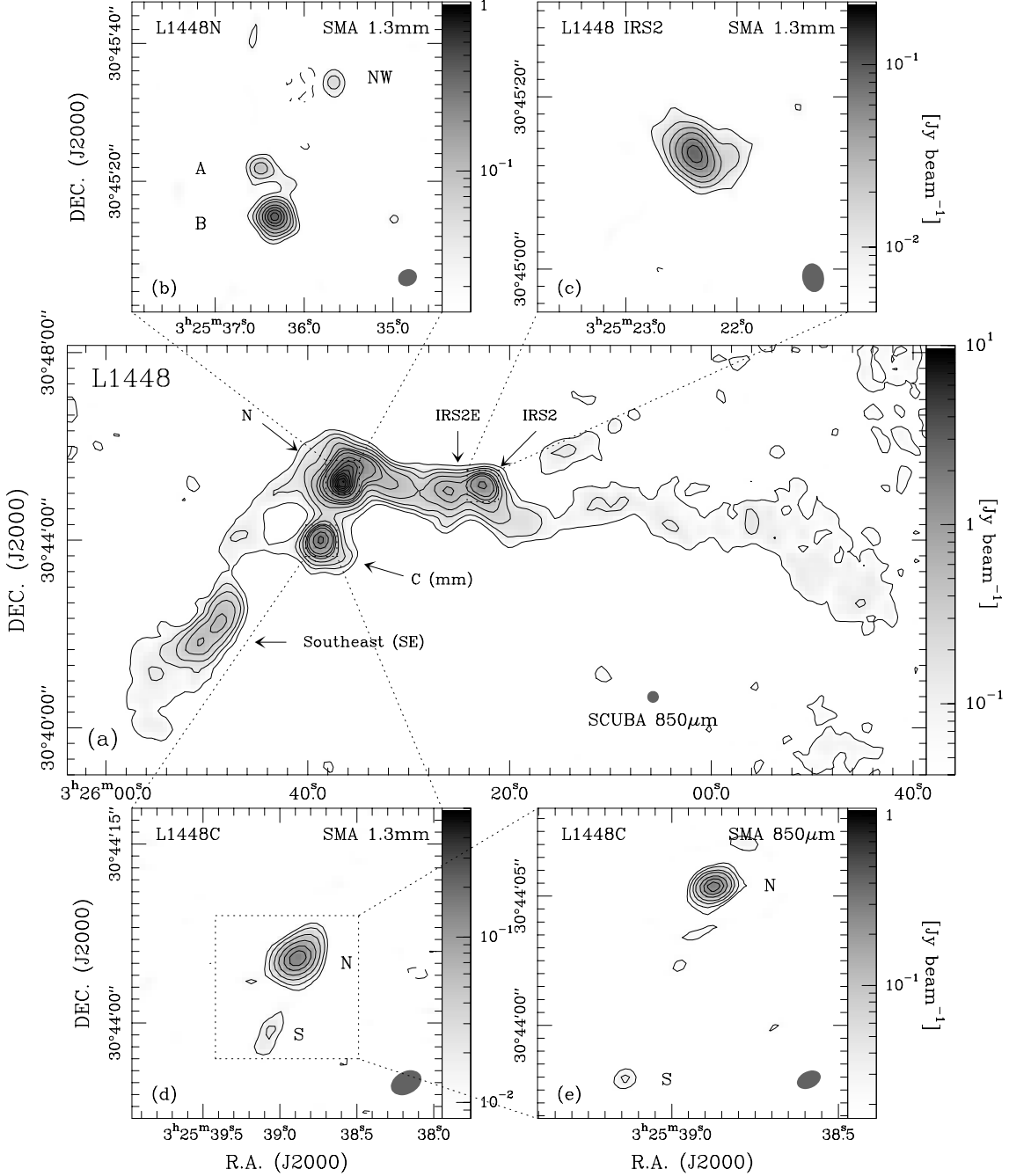


Fig. 3.— (a) JCMT/SCUBA 850  $\mu\text{m}$  dust continuum image of L1448. Contour levels correspond to 1, 3, 5, 8, 12, 15, and 20  $\sigma$ , then increase in steps of 15  $\sigma$  ( $1\sigma \sim 40 \text{ mJy beam}^{-1}$ ). The SCUBA FWHM beam ( $\sim 14''$ ) is shown as a grey oval in the image. (b) SMA 1.3 mm dust continuum image of L1448N. Contour levels correspond to  $-3, 3, 6, 10$ , and  $15\sigma$ , then increase in steps of 10  $\sigma$  ( $1\sigma \sim 7.0 \text{ mJy beam}^{-1}$ ). (c) SMA 1.3 mm dust continuum image of L1448 IRS2. Contour levels correspond to  $-3, 3, 6, 10$ , and  $16\sigma$ , then increase in steps of 10  $\sigma$  ( $1\sigma \sim 2.1 \text{ mJy beam}^{-1}$ ). (d) SMA 1.3 mm dust continuum image of L1448C. Contour levels correspond to  $-3, 3, 5, 9$ , and  $15\sigma$ , then increase in steps of 8  $\sigma$  ( $1\sigma \sim 4.0 \text{ mJy beam}^{-1}$ ). (e) SMA 850  $\mu\text{m}$  image of L1448C. Contour levels correspond to  $-3, 3, 6, 10$ , and  $15\sigma$ , then increase in steps of 10  $\sigma$  ( $1\sigma \sim 5.5 \text{ mJy beam}^{-1}$ ). The synthesized SMA beam is shown as a grey oval in the bottom right corner of each SMA dust continuum image.

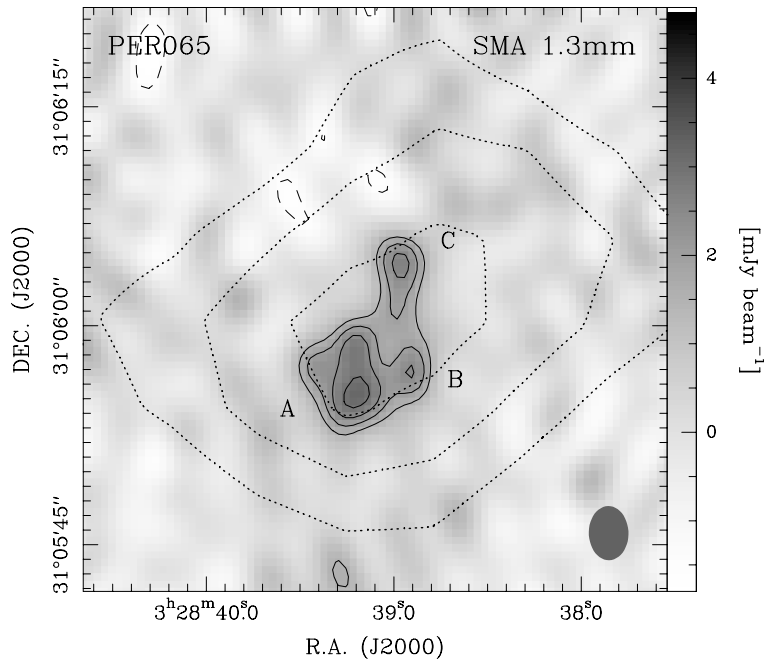


Fig. 4.— SMA 1.3 mm dust continuum image of source PER 065, overlapped with the SCUBA 850  $\mu\text{m}$  contours. The SMA contours (solid lines) start from  $-3\sigma$ ,  $3\sigma$ , then increase in steps of  $1\sigma$  ( $1\sigma \sim 5.0 \text{ mJy beam}^{-1}$ ). The synthesized SMA beam is shown as a grey oval in the bottom right corner. The SCUBA 850  $\mu\text{m}$  contours (dotted lines) correspond to 75%, 85%, and 95% of the peak emission ( $\sim 0.3 \text{ Jy beam}^{-1}$ ).

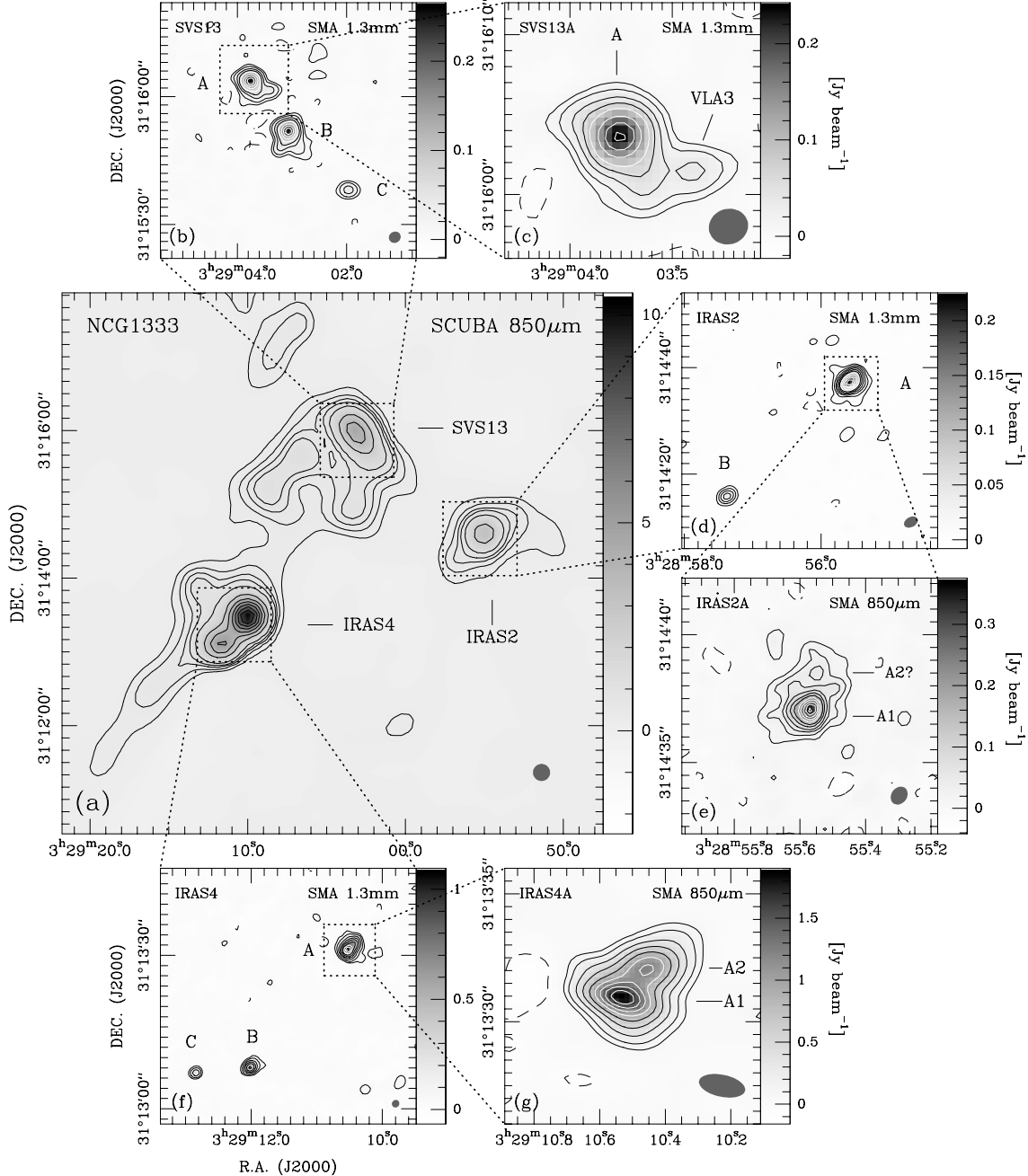


Fig. 5.— (a) JCMT/SCUBA 850  $\mu\text{m}$  dust continuum image of the NCG 1333 central region. Contour levels correspond to 5, 10, 15, 20 and 30  $\sigma$ , then increase in steps of 30  $\sigma$  ( $1\sigma \sim 42 \text{ mJy beam}^{-1}$ ). The SCUBA FWHM beam is shown as a grey circle in the bottom right corner of the image. (b) SMA 1.3 mm dust continuum image of SVS 13. Contour levels correspond to  $-3, 3, 6, 12, 20$ , and  $30\sigma$ , then increase in steps of  $20\sigma$  ( $1\sigma \sim 2.5 \text{ mJy beam}^{-1}$ ). (c) Enlarged view of source SVS 13A. (d) SMA 1.3 mm dust continuum image of IRAS 2. Contour levels correspond to  $-3, 3, 6, 10, 15, 22, 30$ , and  $40\sigma$ , then increase in steps of  $15\sigma$  ( $1\sigma \sim 2.0 \text{ mJy beam}^{-1}$ ). (e) SMA 850  $\mu\text{m}$  dust continuum image of IRAS 2A. Contour levels correspond to  $-3, 3, 6, 10, 15, 22$ , and  $30\sigma$ , then increase in steps of  $10\sigma$  ( $1\sigma \sim 4.5 \text{ mJy beam}^{-1}$ ). (f) SMA 1.3 mm dust continuum image of IRAS 4. Contour levels correspond to  $-3, 3, 6, 12, 20$ , and  $30\sigma$ , then increase in steps of  $15\sigma$  ( $1\sigma \sim 12 \text{ mJy beam}^{-1}$ ). (g) SMA 850  $\mu\text{m}$  dust continuum image of IRAS 4A. Contour levels correspond to  $-3, 3, 6, 12$ , and  $20\sigma$ , then increase in steps of  $10\sigma$  ( $1\sigma \sim 24 \text{ mJy beam}^{-1}$ ). The synthesized SMA beam is shown as a grey oval in the bottom right corner of each SMA dust continuum image.

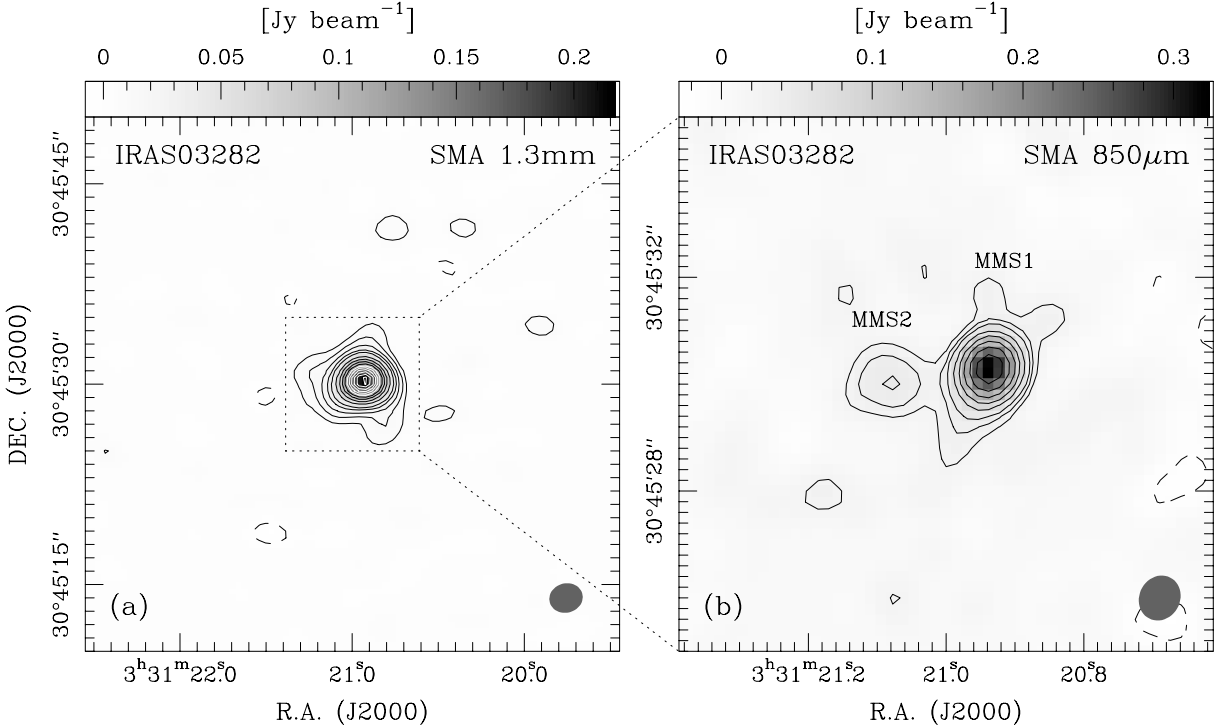


Fig. 6.— (a) SMA 1.3 mm dust continuum image of IRAS 03282. The SMA contour levels correspond to  $-3, 3, 6, 10, 15$ , and  $20\sigma$ , then increase in steps of  $10\sigma$  ( $1\sigma \sim 1.8 \text{ mJy beam}^{-1}$ ). (b) SMA 850  $\mu\text{m}$  dust continuum image of IRAS 03282. Contour levels correspond to  $-3, 3, 5, 7, 11, 16, 22$ , and  $30\sigma$ , then increase in steps of  $10\sigma$  ( $1\sigma \sim 4.0 \text{ mJy beam}^{-1}$ ). The synthesized SMA beam is shown as a grey oval in the bottom right corner of the two SMA dust continuum images.

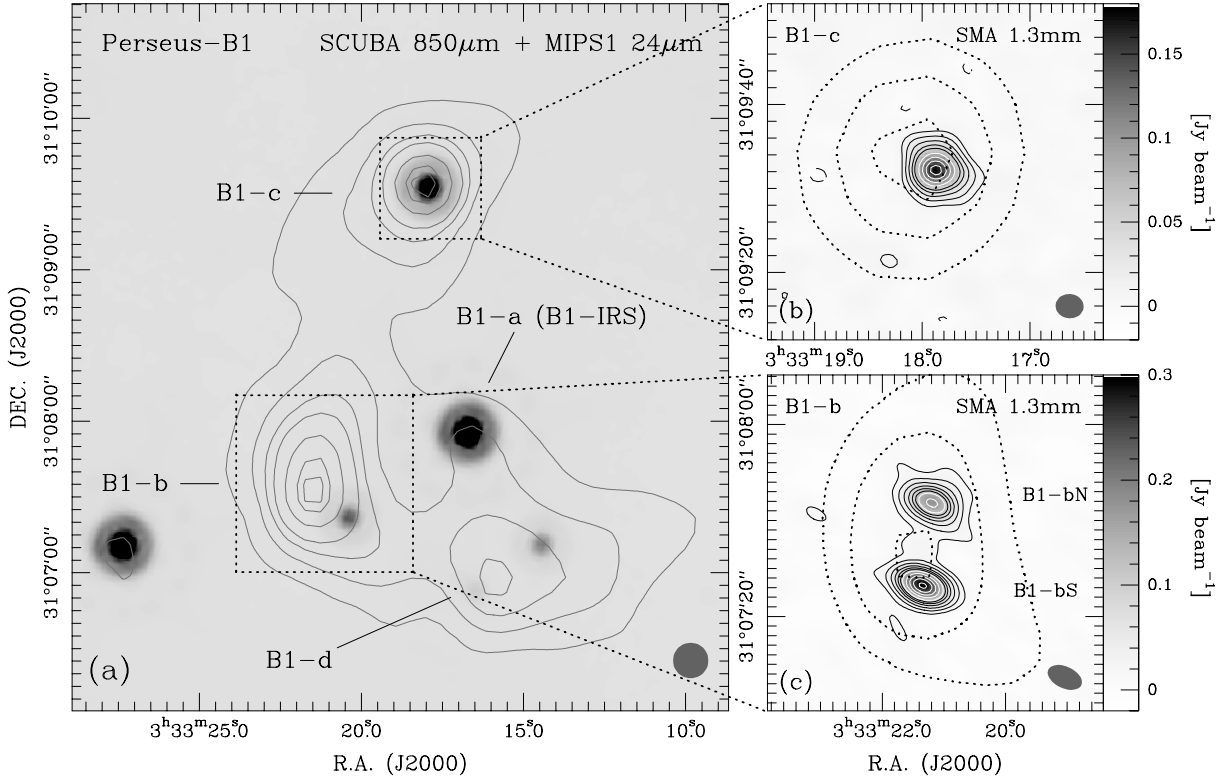


Fig. 7.— (a) JCMT/SCUBA 850  $\mu\text{m}$  dust continuum image of the Per-B1 central region, plotted on the *Spitzer* 24  $\mu\text{m}$  image. The SCUBA contour levels correspond to 10%, 20%, 30%, 40%, 60%, 80%, and 90% of the peak emission ( $\sim 2.5 \text{ Jy beam}^{-1}$ ). The SCUBA FWHM beam is shown as a grey circle in the bottom right corner of the image. (b) SMA 1.3 mm dust continuum image of Per-B1c, overlaid with the SCUBA 850  $\mu\text{m}$  contours. The SMA contours (solid lines) correspond to  $-3, 3, 6, 10, 15$ , and  $20\sigma$ , then increase in steps of  $10\sigma$  ( $1\sigma \sim 2.7 \text{ mJy beam}^{-1}$ ). The SCUBA 850  $\mu\text{m}$  contours (dotted lines) correspond to 50%, 70%, and 90% of the peak emission. (c) SMA 1.3 mm dust continuum image of Per-B1b, overlaid with the SCUBA 850  $\mu\text{m}$  contours. The SMA contours (solid lines) correspond to  $-3, 3, 6, 10, 15, 20, 25$ , and  $30\sigma$ , then increase in steps of  $10\sigma$  ( $1\sigma \sim 4.2 \text{ mJy beam}^{-1}$ ). The SCUBA 850  $\mu\text{m}$  contours (dotted lines) correspond to 30%, 50%, and 90% of the peak emission. The synthesized SMA beam is shown as a grey oval in the bottom right corner of the two SMA dust continuum images.

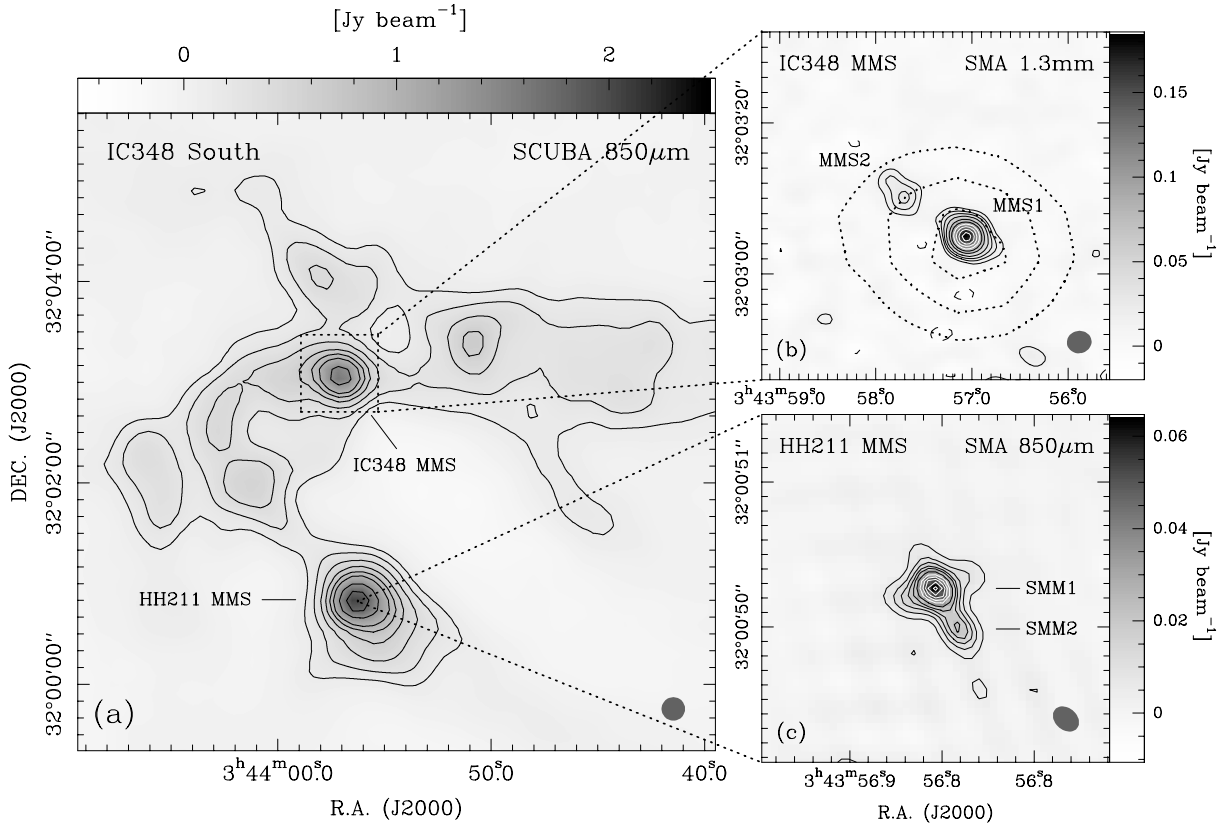


Fig. 8.— (a) SCUBA 850  $\mu\text{m}$  dust continuum image of the IC 348 southern region. The SCUBA contour levels correspond to 3, 6, 10, 15, 20 and 25  $\sigma$ , then increase in steps of  $10\sigma$  ( $1\sigma \sim 40 \text{ mJy beam}^{-1}$ ). The SCUBA FWHM beam is shown as a grey circle in the bottom right corner of the image. (b) SMA 1.3 mm dust continuum image of IC 348 MMS, overlapped with the SCUBA 850  $\mu\text{m}$  contours. The SMA contours (solid lines) correspond to  $-3, 3, 5, 7, 10, 15, 20$ , and  $25\sigma$ , then increase in steps of  $6\sigma$  ( $1\sigma \sim 4.0 \text{ mJy beam}^{-1}$ ). The SCUBA 850  $\mu\text{m}$  contours (dotted lines) correspond to 50%, 70%, and 90% of the peak emission of the IC 348 MMS core ( $\sim 1.6 \text{ Jy beam}^{-1}$ ). (c) SMA 850  $\mu\text{m}$  image of HH211 MMS. The SMA contours correspond to  $-3, 3, 6, 9, 12, 15, 20$ , and  $25\sigma$ , then increase in steps of  $5\sigma$  ( $1\sigma \sim 1.4 \text{ mJy beam}^{-1}$ ). The synthesized SMA beam is shown as a grey oval in the bottom right corner of the two SMA dust continuum images.

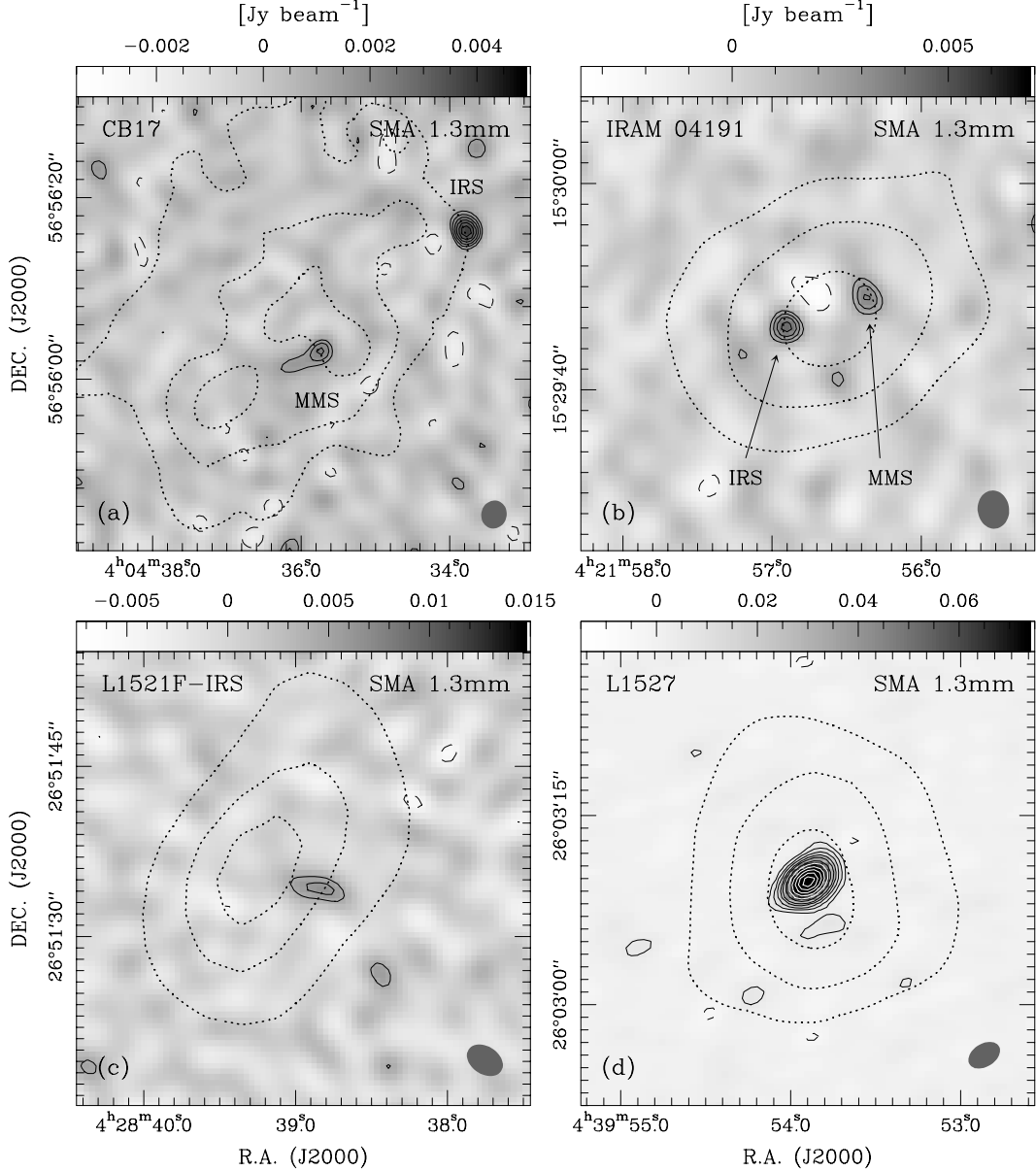


Fig. 9.— (a) SMA 1.3 mm dust continuum image of CB 17, overlapped with the SCUBA 850  $\mu\text{m}$  contours. The SMA contours (solid lines) start at  $-3, 3\sigma$ , then increase in steps of  $1\sigma$  ( $1\sigma \sim 0.5 \text{ mJy beam}^{-1}$ ). The SCUBA contours (dotted lines) correspond to 50%, 70%, and 90% of the peak emission ( $\sim 170 \text{ mJy beam}^{-1}$ ). (b) The same as Figure a, but for source IRAM 04191. The SMA contours start at  $-3, 3\sigma$ , then increase in steps of  $1\sigma$  ( $1\sigma \sim 7 \text{ mJy beam}^{-1}$ ). The SCUBA 850  $\mu\text{m}$  contours correspond to 50%, 70%, and 90% of the peak emission ( $\sim 0.37 \text{ Jy beam}^{-1}$ ). (c) The same as Figure a, but for source L1521-IRS. The SMA contours correspond to  $-3, 3$ , and  $5\sigma$  ( $1\sigma \sim 1.5 \text{ mJy beam}^{-1}$ ). The SCUBA 850  $\mu\text{m}$  contours correspond to 70%, 85%, and 95% of the peak emission ( $\sim 0.44 \text{ Jy beam}^{-1}$ ). (d) The same as Figure a, but for source L1527. The SMA contours correspond to  $-3, 3, 6, 10, 15, 20, 30$ , and  $40\sigma$ , then increase in steps of  $15\sigma$  ( $1\sigma \sim 1.5 \text{ mJy beam}^{-1}$ ). The SCUBA 850  $\mu\text{m}$  contours correspond to 50%, 70%, and 90% of the peak emission ( $\sim 0.5 \text{ Jy beam}^{-1}$ ). The synthesized SMA beam is shown as a grey oval in the bottom right corner of the each SMA image.

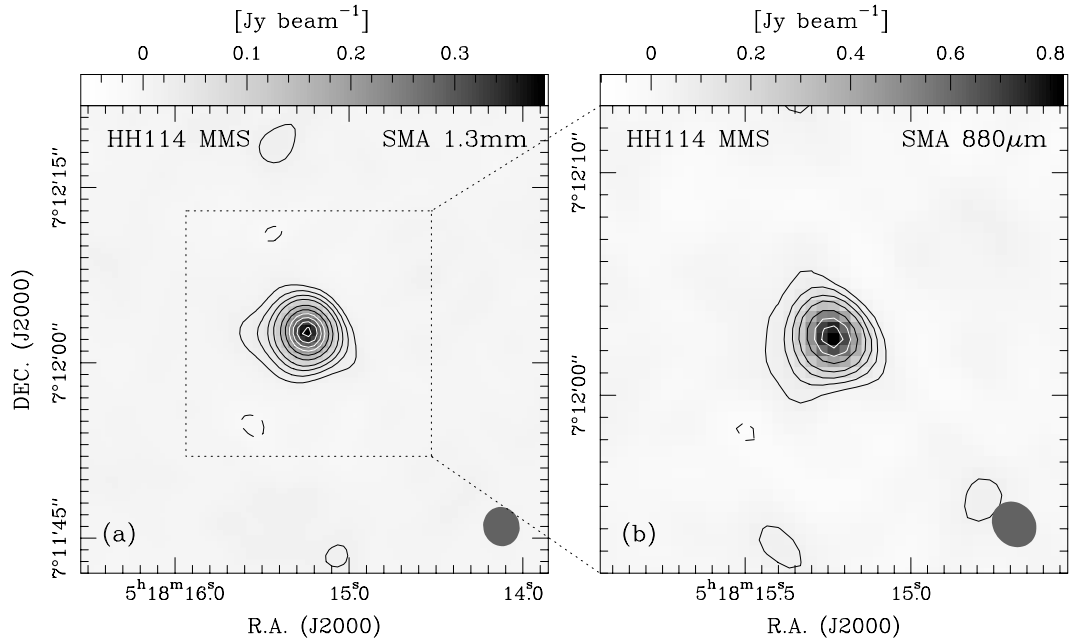


Fig. 10.— (a) SMA 1.3 mm dust continuum image of HH 114 MMS. The contour levels correspond to  $-3, 3, 6, 10$ , and  $15\sigma$ , then increase in steps of  $10\sigma$  ( $1\sigma \sim 5.0$  mJy beam<sup>-1</sup>). (b) SMA 880  $\mu$ m dust continuum image of HH 114 MMS. The contour levels correspond to  $-3, 3, 6, 10$ , and  $15\sigma$ , then increase in steps of  $10\sigma$  ( $1\sigma \sim 16$  mJy beam<sup>-1</sup>). The synthesized SMA beam is shown as a grey oval in the bottom right corner of the two SMA dust continuum images.

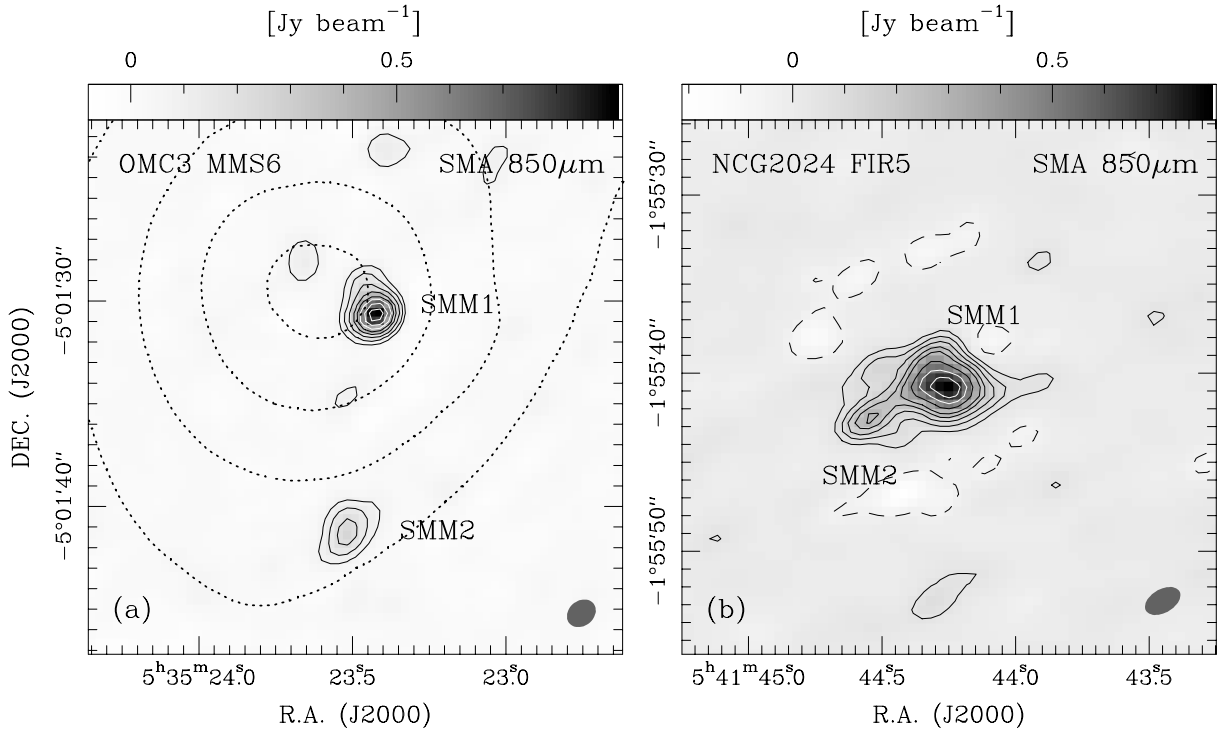


Fig. 11.— (a) SMA 850  $\mu\text{m}$  dust continuum image of OMC3 MMS6, overlaid with the SCUBA 850  $\mu\text{m}$  contours. The SMA contours (solid lines) correspond to  $-3, 3, 6, 10, 15, 20,$  and  $25\sigma$ , then increase in steps of  $8\sigma$  ( $1\sigma \sim 20 \text{ mJy beam}^{-1}$ ). The SCUBA 850  $\mu\text{m}$  contours (dotted lines) correspond to 25%, 50%, 75%, and 95% of the peak emission ( $\sim 27 \text{ Jy beam}^{-1}$ ). (b) SMA 850  $\mu\text{m}$  dust continuum image of NGC 2024 FIR5. The SMA contours correspond to  $-3, 3, 6, 10, 15,$  and  $20\sigma$ , then increase in steps of  $10\sigma$  ( $1\sigma \sim 14 \text{ mJy beam}^{-1}$ ). The synthesized SMA beam is shown as a grey oval in the bottom right corner of the two SMA dust continuum images.

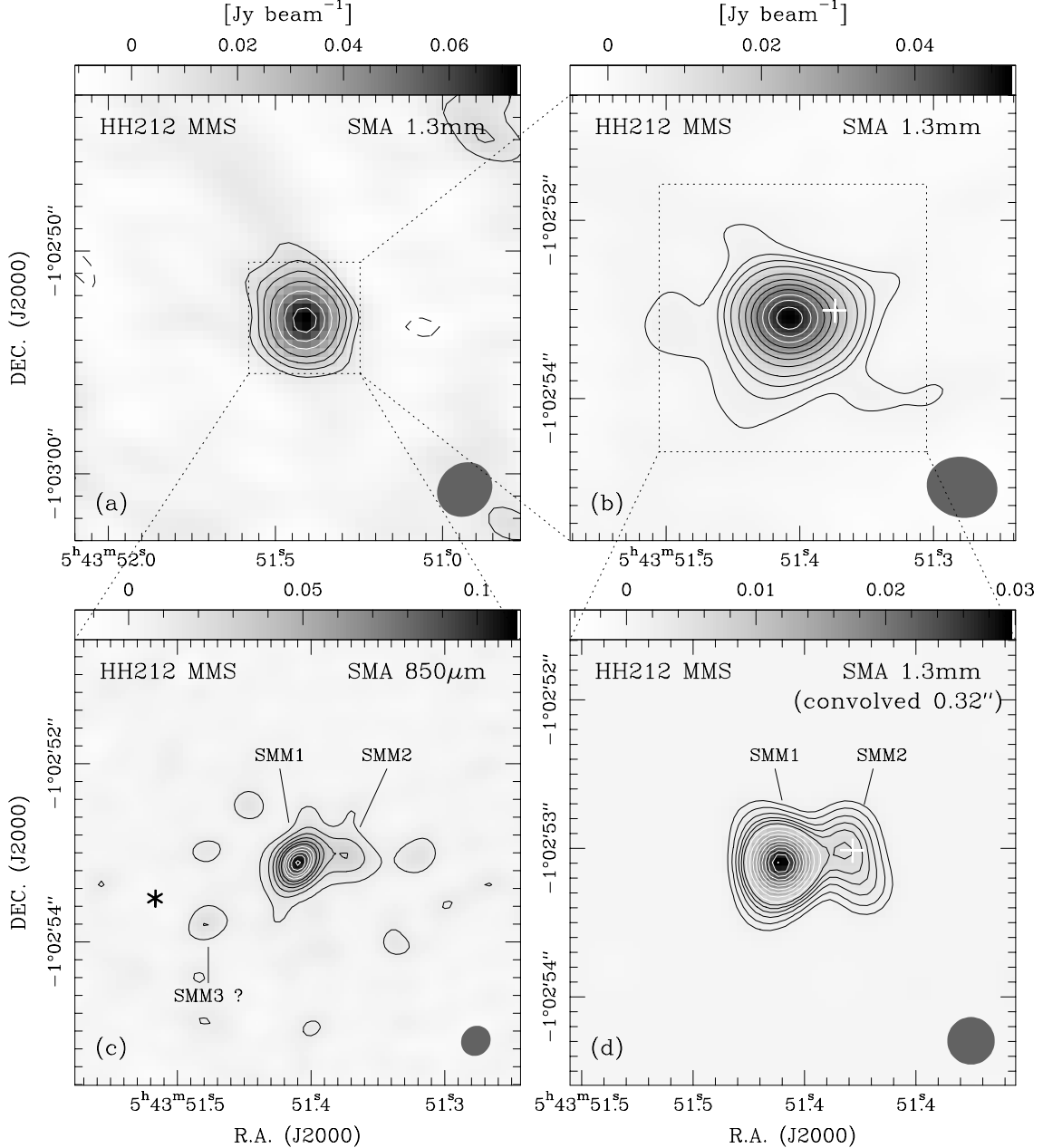


Fig. 12.— (a) SMA 1.3 mm dust continuum image of HH 212 MMS (resolution  $2.^{\prime\prime}6 \times 2.^{\prime\prime}3$ ). The SMA contours correspond to  $-3, 3, 5, 7$ , and  $10\sigma$ , then increase in steps of  $4\sigma$  ( $1\sigma \sim 3.0 \text{ mJy beam}^{-1}$ ). (b) SMA 1.3 mm dust continuum image (resolution  $0.^{\prime\prime}8 \times 0.^{\prime\prime}7$ ); the contours correspond to  $-3, 3, 5, 7$ , and  $10\sigma$ , then increase in steps of  $5\sigma$  ( $1\sigma \sim 1.1 \text{ mJy beam}^{-1}$ ). (c) The SMA  $850 \mu\text{m}$  dust continuum image (resolution  $0.^{\prime\prime}35 \times 0.^{\prime\prime}32$ ); the contours correspond to  $-3, 3, 7$ , and  $11\sigma$ , then increase in steps of  $4\sigma$  ( $1\sigma \sim 2.8 \text{ mJy beam}^{-1}$ ). (d) The restored SMA 1.3 mm image with angular resolution of  $0.^{\prime\prime}32 \times 0.^{\prime\prime}32$ ; the contours correspond to  $-3, 5, 8, 12, 16, 20, 25$ , and  $30\sigma$ , then increase in steps of  $10\sigma$  ( $1\sigma \sim 0.25 \text{ mJy beam}^{-1}$ ). The white crosses in Figures b & d show the position of the secondary continuum source derived from Figure c, while the stellar symbol in Figure c shows the position of the 1.4 mm dust continuum source detected by Codella et al. (2007).

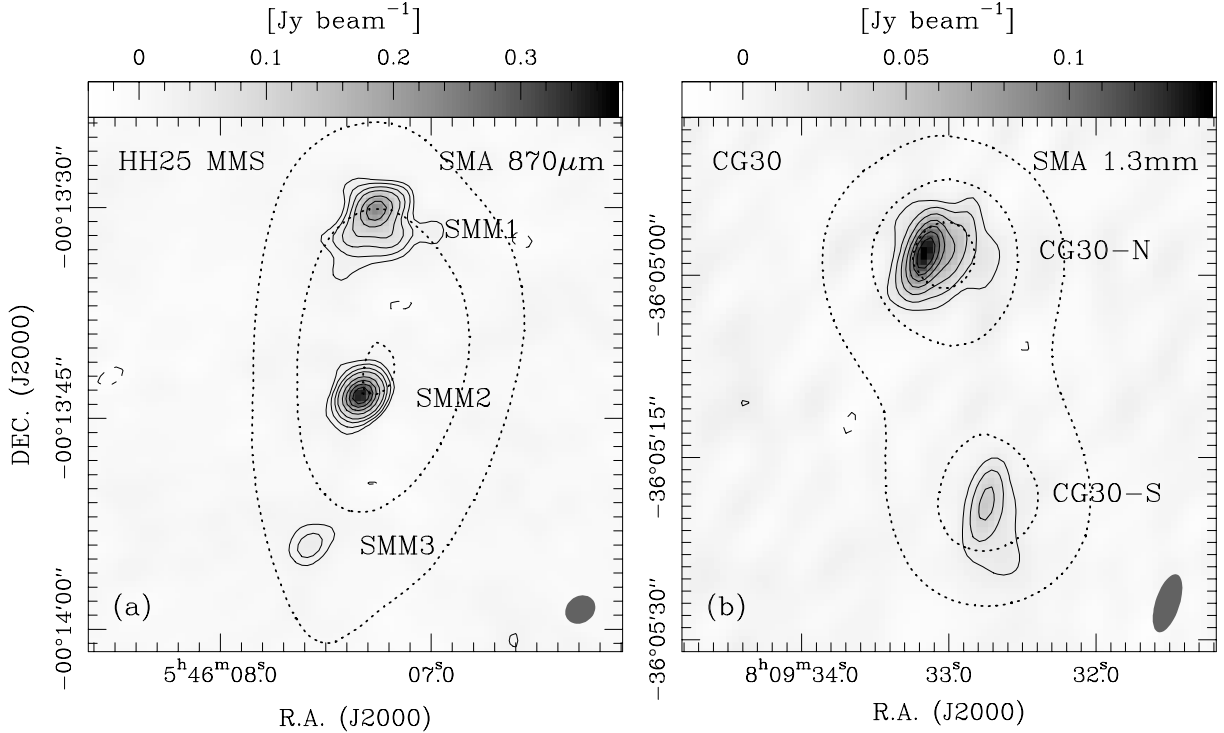


Fig. 13.— (a) SMA 870  $\mu\text{m}$  dust continuum image of HH 25 MMS, overlapped with the SCUBA 850  $\mu\text{m}$  contours. The SMA contour levels (solid lines) correspond to  $-3, 3, 5, 8$ , and  $12\sigma$ , then increase in steps of  $8\sigma$  ( $1\sigma \sim 6.8 \text{ mJy beam}^{-1}$ ). The SCUBA contours (dotted lines) represent the 50%, 75%, and 99% levels of the peak emission ( $\sim 1.6 \text{ Jy beam}^{-1}$ ). (b) SMA 1.3 mm dust continuum image of CG 30, overlapped with the SCUBA 850  $\mu\text{m}$  contours. The SMA contours (solid lines) correspond to  $-3, 3, 6, 10, 15, 20, 25$ , and  $30\sigma$ , then increase in steps of  $10\sigma$  ( $1\sigma \sim 4.0 \text{ mJy beam}^{-1}$ ). The SCUBA contours (dotted lines) represent the 50%, 75%, and 95% levels of the peak emission ( $\sim 1.2 \text{ Jy beam}^{-1}$ ). The synthesized SMA beam is shown as a grey oval in the bottom right corner of the two SMA dust continuum images.

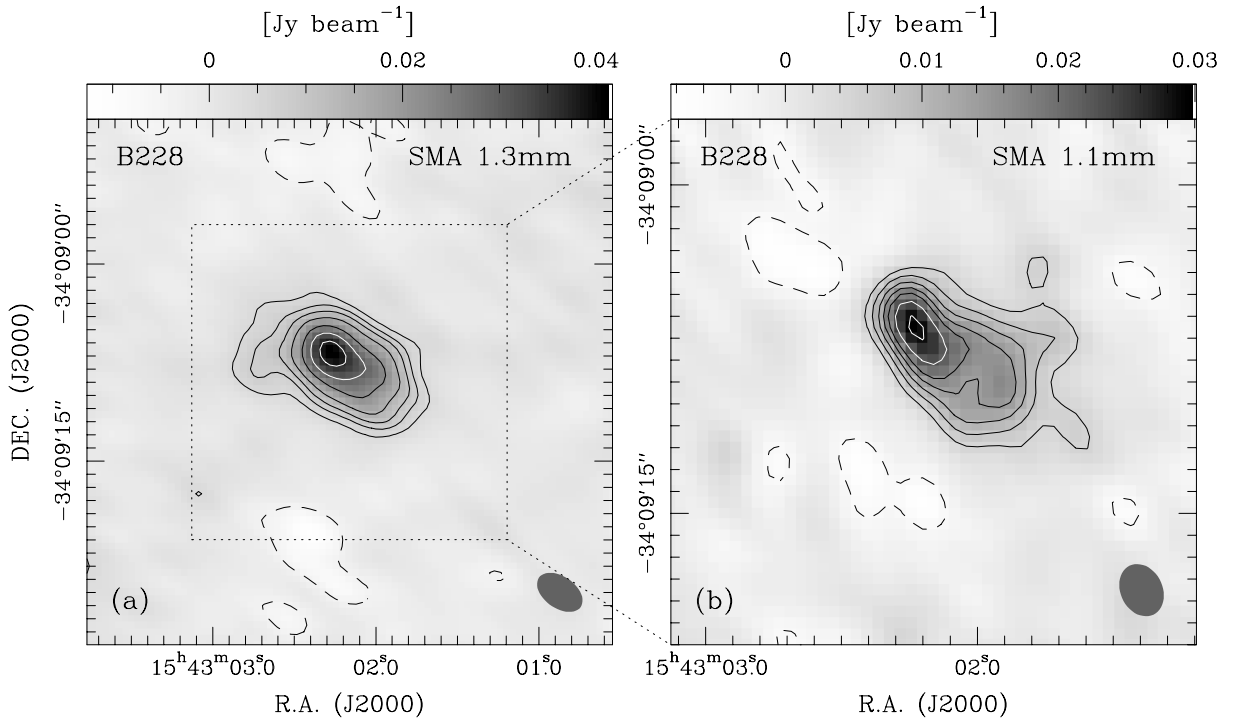


Fig. 14.— (a) SMA 1.3 mm dust continuum image of B 228. The contour levels correspond to  $-3, 3, 5, 7$ , and  $10\sigma$ , then increase in steps of  $5\sigma$  ( $1\sigma \sim 1.5 \text{ mJy beam}^{-1}$ ). (b) SMA 1.1 mm dust continuum image of B 228. The contour levels correspond to  $-3, 3, 5, 7, 9, 11, 14$ , and  $18\sigma$  ( $1\sigma \sim 1.6 \text{ mJy beam}^{-1}$ ). The synthesized SMA beam is shown as a grey oval in the bottom right corner of the two SMA images.

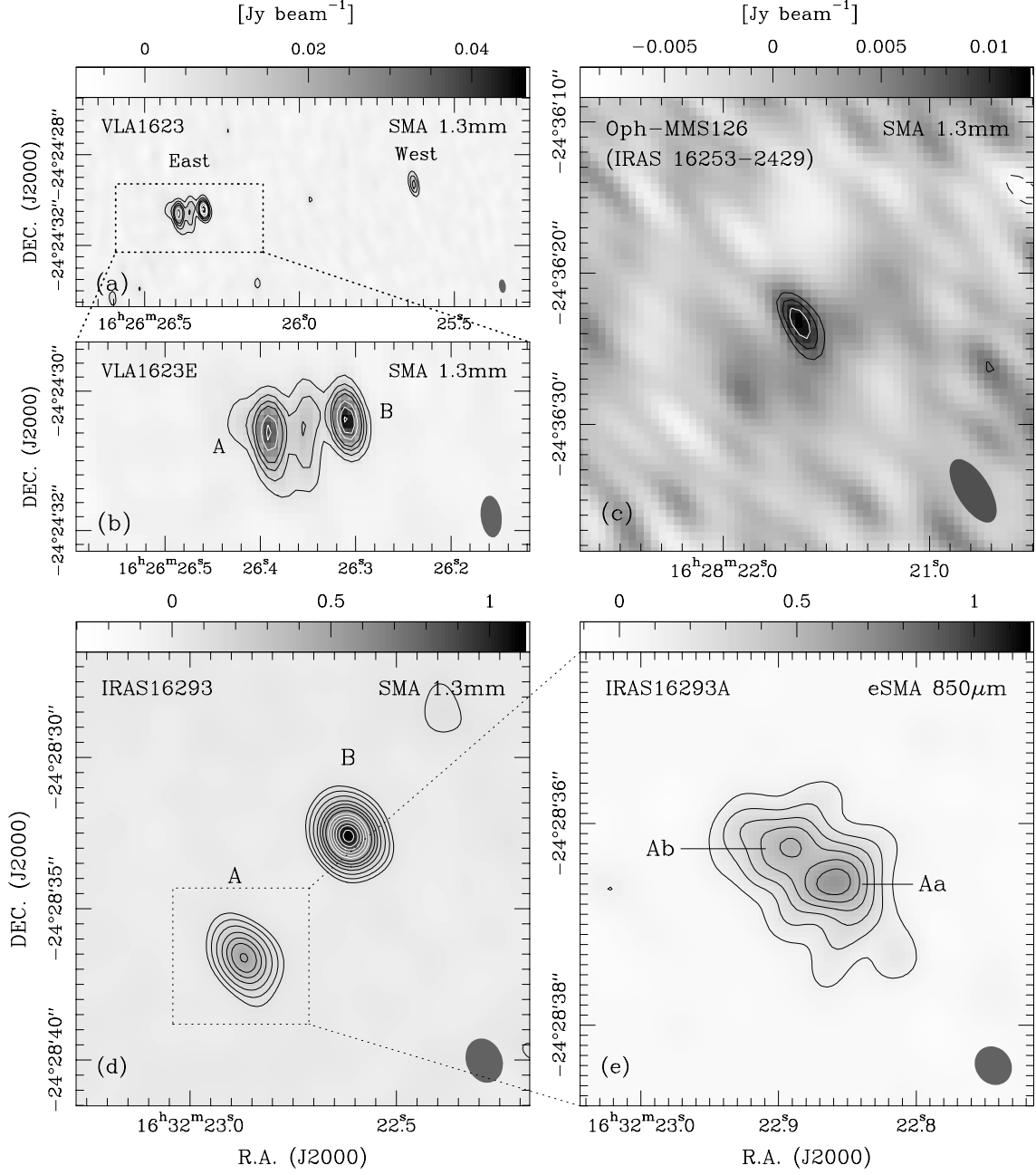


Fig. 15.— (a) SMA 1.3 mm dust continuum image of VLA 1623. The contour levels correspond to 5, 10, 15, 20, and 30  $\sigma$ , then increase in steps of 8  $\sigma$  ( $1\sigma \sim 1.0 \text{ mJy beam}^{-1}$ ). (b) The enlarged view of the VLA 1623 East pair. (c) SMA 1.3 mm dust continuum image of Oph-MMS 126. The contour levels correspond to -3, 3, 4, and 5  $\sigma$  ( $1\sigma \sim 2.1 \text{ mJy beam}^{-1}$ ). (d) SMA 1.3 mm dust continuum image of IRAS 16293. The contour levels correspond to -3, 3, 5, 8, 12, 16, and 20  $\sigma$ , then increase in steps of 5  $\sigma$  ( $1\sigma \sim 19 \text{ mJy beam}^{-1}$ ). (e) The eSMA 850  $\mu\text{m}$  continuum image of source IRAS 16293 A. The contour levels correspond to -3, 5, and 10  $\sigma$ , then increase in steps of 5  $\sigma$  ( $1\sigma \sim 20 \text{ mJy beam}^{-1}$ ). The synthesized SMA beam is shown as a grey oval in the bottom right corner of each SMA image.

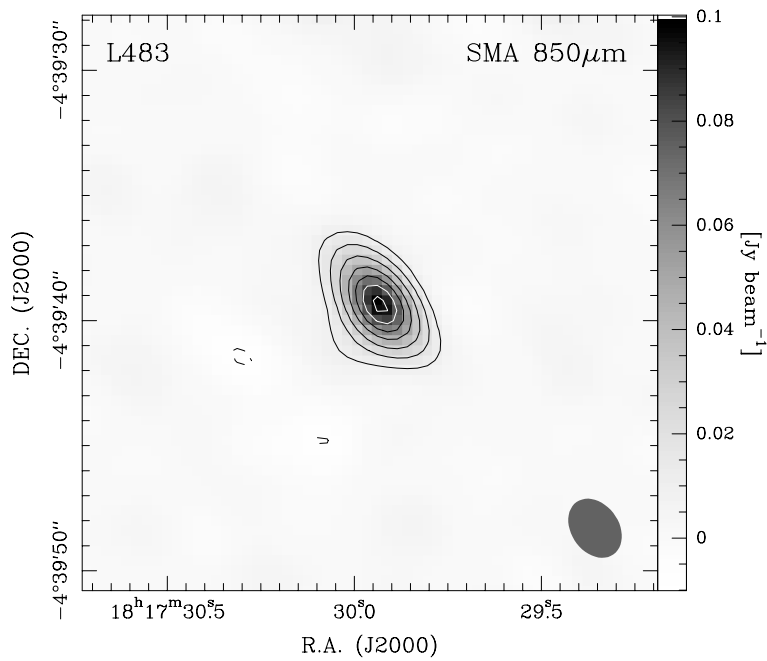


Fig. 16.— SMA 850  $\mu$ m dust continuum image of L483. The contour levels correspond to  $-3$ ,  $3$ ,  $6$ , and  $10\sigma$ , then increase in steps of  $5\sigma$  ( $1\sigma \sim 3.2 \text{ mJy beam}^{-1}$ ). The synthesized SMA beam is shown as a grey oval in the bottom right corner.

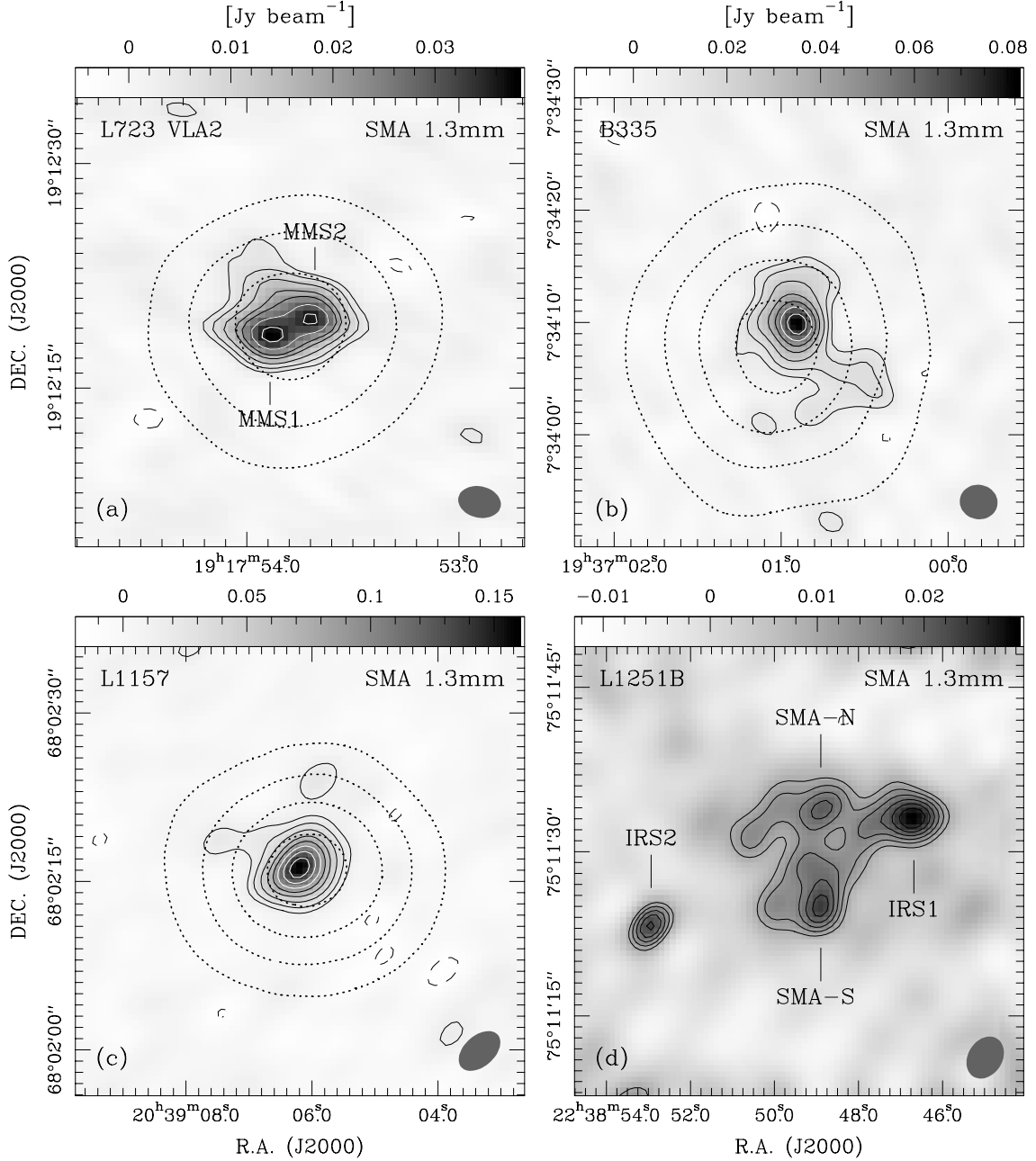


Fig. 17.— (a) SMA 1.3 mm dust continuum image of L723, overlapped with the SCUBA 850  $\mu\text{m}$  contours. The SMA contours (solid lines) correspond to  $-3, 3, 5, 8, 12$ , and  $15\sigma$  levels and then increase in steps of  $5\sigma$  ( $1\sigma \sim 1.4 \text{ mJy beam}^{-1}$ ). The SCUBA 850  $\mu\text{m}$  contours (dotted lines) represent 30%, 50%, and 90% of the peak emission ( $\sim 0.9 \text{ Jy beam}^{-1}$ ). (b) Same as Figure a, but for source B335. The SMA contours correspond to  $-3, 3, 5, 8, 12, 16$ , and  $20\sigma$  levels and then increase in steps of  $5\sigma$  ( $1\sigma \sim 2.9 \text{ mJy beam}^{-1}$ ). The SCUBA 850  $\mu\text{m}$  contours represent 30%, 50%, 70%, and 90% of the peak emission ( $\sim 1.2 \text{ Jy beam}^{-1}$ ). (c) Same as Figure b, but for source L1157, where  $1\sigma$  noise in the SMA image is  $\sim 4.8 \text{ mJy beam}^{-1}$  and the peak value in the SCUBA 850  $\mu\text{m}$  image is  $\sim 1.4 \text{ Jy beam}^{-1}$ . (d) SMA 1.3 mm dust continuum image of L1251B. The SMA contours start at  $-3, 3\sigma$  and then increase in steps of  $1\sigma$  ( $1\sigma \sim 3.2 \text{ mJy beam}^{-1}$ ).

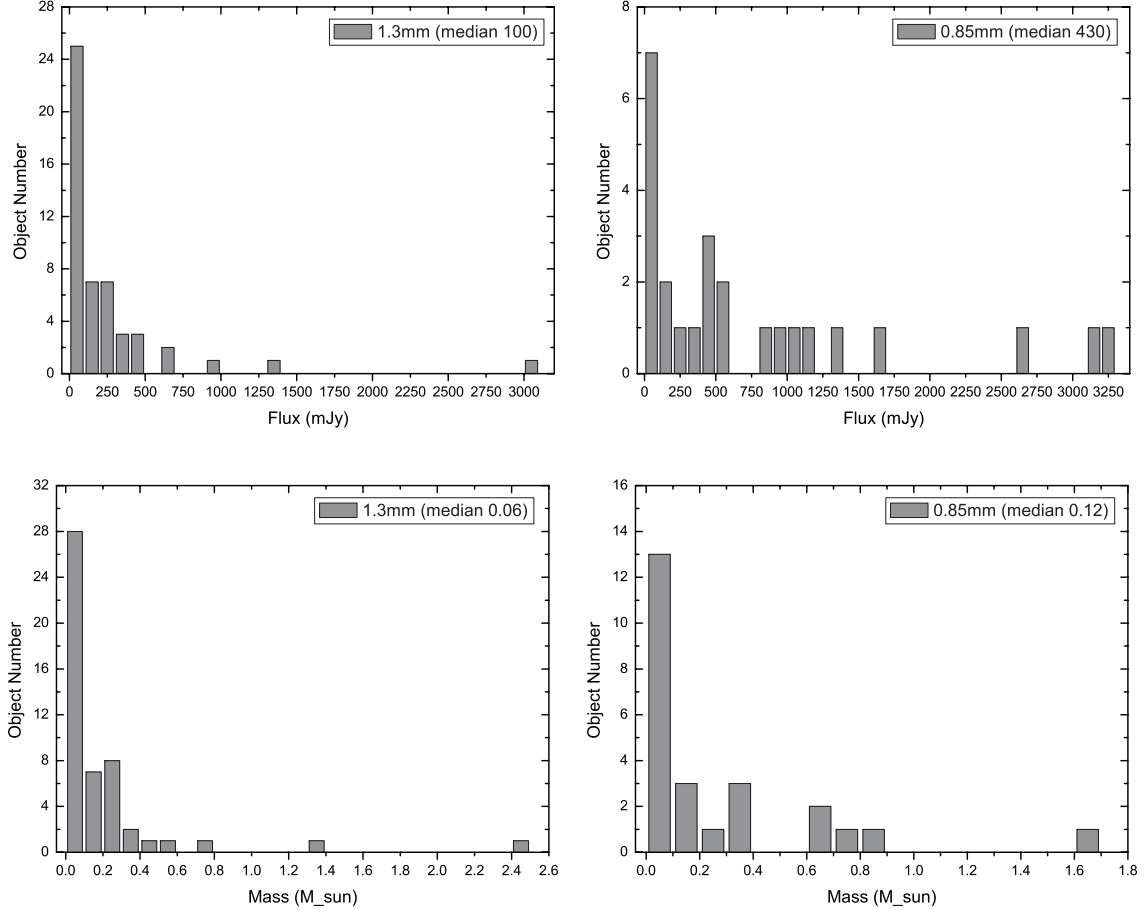


Fig. 18.— *Top Left:* Distribution of the 1.3 mm fluxes derived in this SMA survey. The median value is 100 mJy. *Top Right:* Distribution of the 850  $\mu$ m fluxes (median value 430 mJy). *Bottom Left:* Distribution of the circumstellar gas masses derived from the 1.3 mm dust continuum observations (median value  $0.06 M_{\odot}$ ). *Bottom Right:* Distribution of the circumstellar gas masses derived from the 850  $\mu$ m dust continuum observations (median value  $0.12 M_{\odot}$ ).

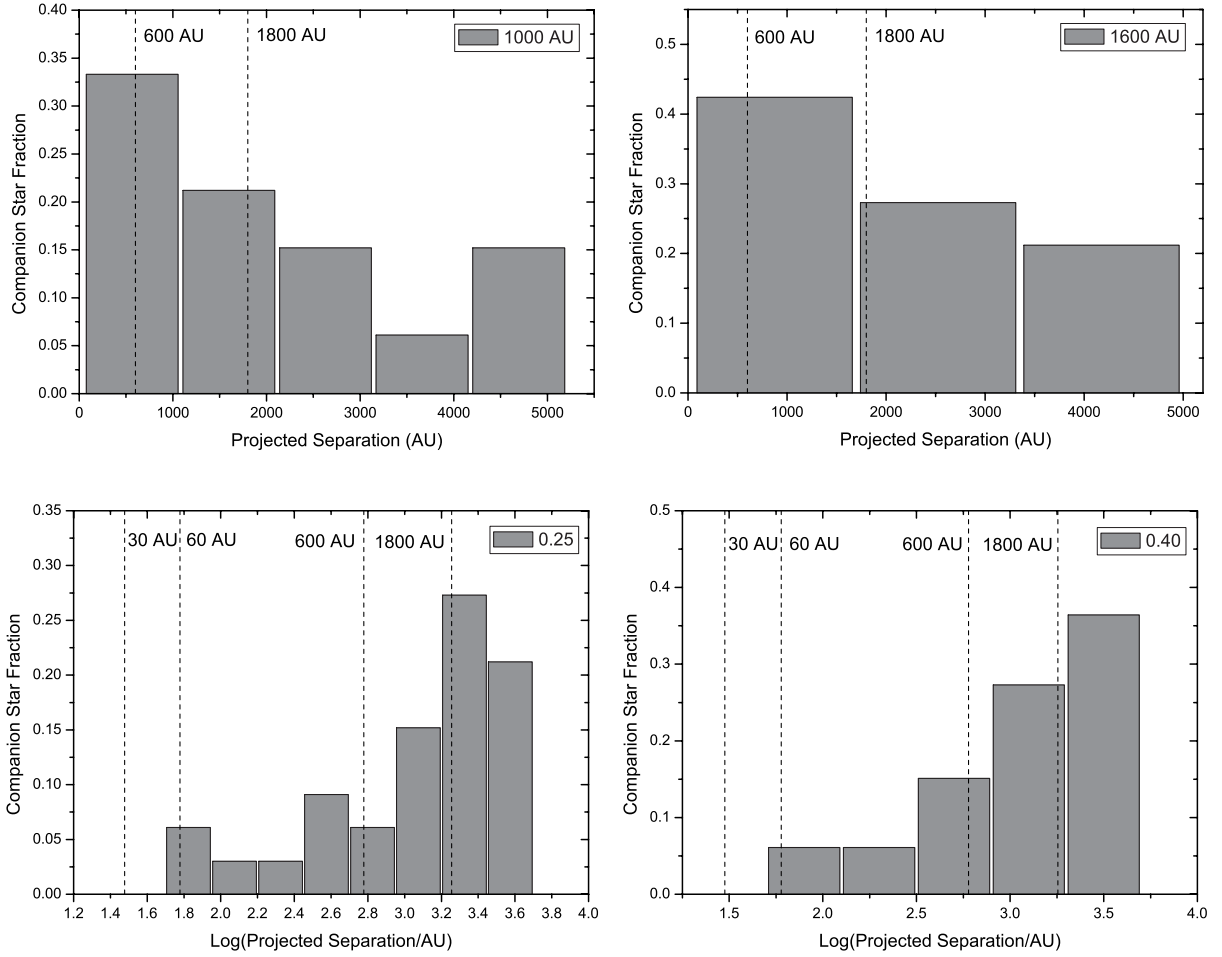


Fig. 19.— Distribution of separations for protobinary systems in this SMA survey (see Table 6), binned in intervals of linear values of 1000 AU (*top left*) and 1600 AU (*top right*), and binned in intervals of log values of 0.25 (*bottom left*) and 0.40 (*bottom right*). The two dashed lines shown in the top figures mark the median linear resolution (600 AU) and median (projected) separation (1800 AU) in this survey, while the four dashed lines shown in the bottom figures mark the peak values in the distributions of separations for main sequence stars (30 AU; see Duquennoy & Mayor 1991) and pre-main sequence stars (60 AU; see Patience et al. 2002), and the median linear resolution and separation in this survey. We note that the ‘separations’ shown here are observed projected separations.

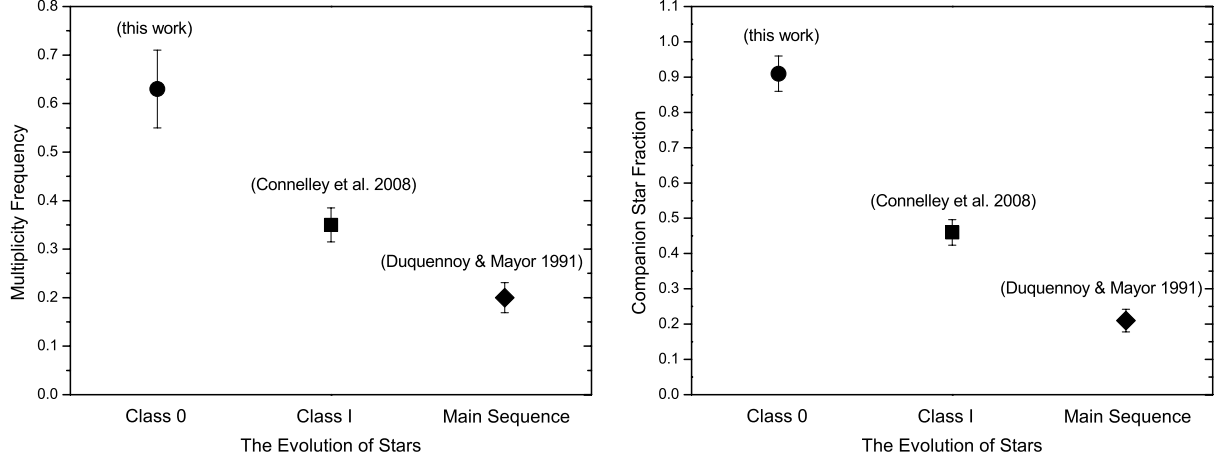


Fig. 20.— Observed multiplicity frequencies (*left*) and companion star fractions (*right*) with separations from 50 AU to 5000 AU for Class 0 protostars (*this work*), Class I young stellar objects (data from Connelley et al. 2008a, b), and main sequence stars (data from Duquennoy & Mayor 1991). It must be noted that the SMA survey for Class 0 protobinary systems is incomplete across the observed separations range, and the derived values should be considered as lower limits.

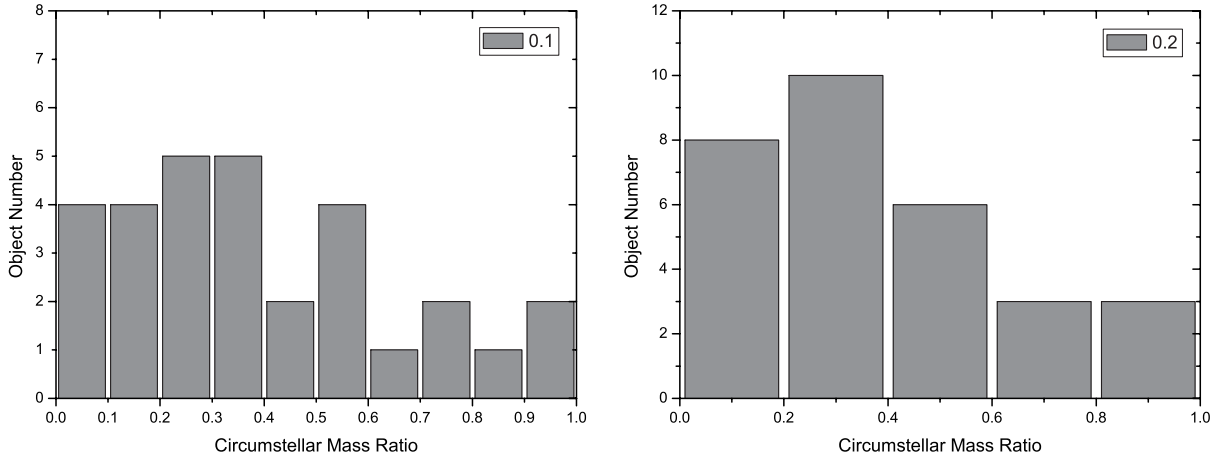


Fig. 21.— Histograms of circumstellar mass ratios for Class 0 protobinary systems in this work (see Table 6), binned in intervals of 0.1 (*left*) and 0.2 (*right*).

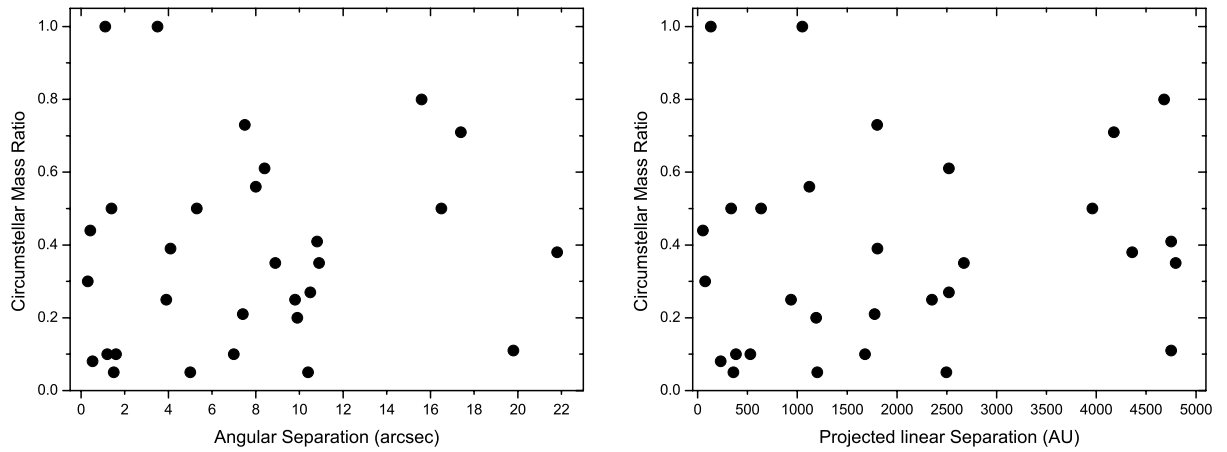


Fig. 22.— The circumstellar mass ratios plotted as a function of angular separations (*left*) and projected linear separations (*right*) for the Class 0 protobinary systems in this work (see Table 6). The diagrams show that there is no obvious relation between mass ratios and separations for the protobinary systems in this sample.

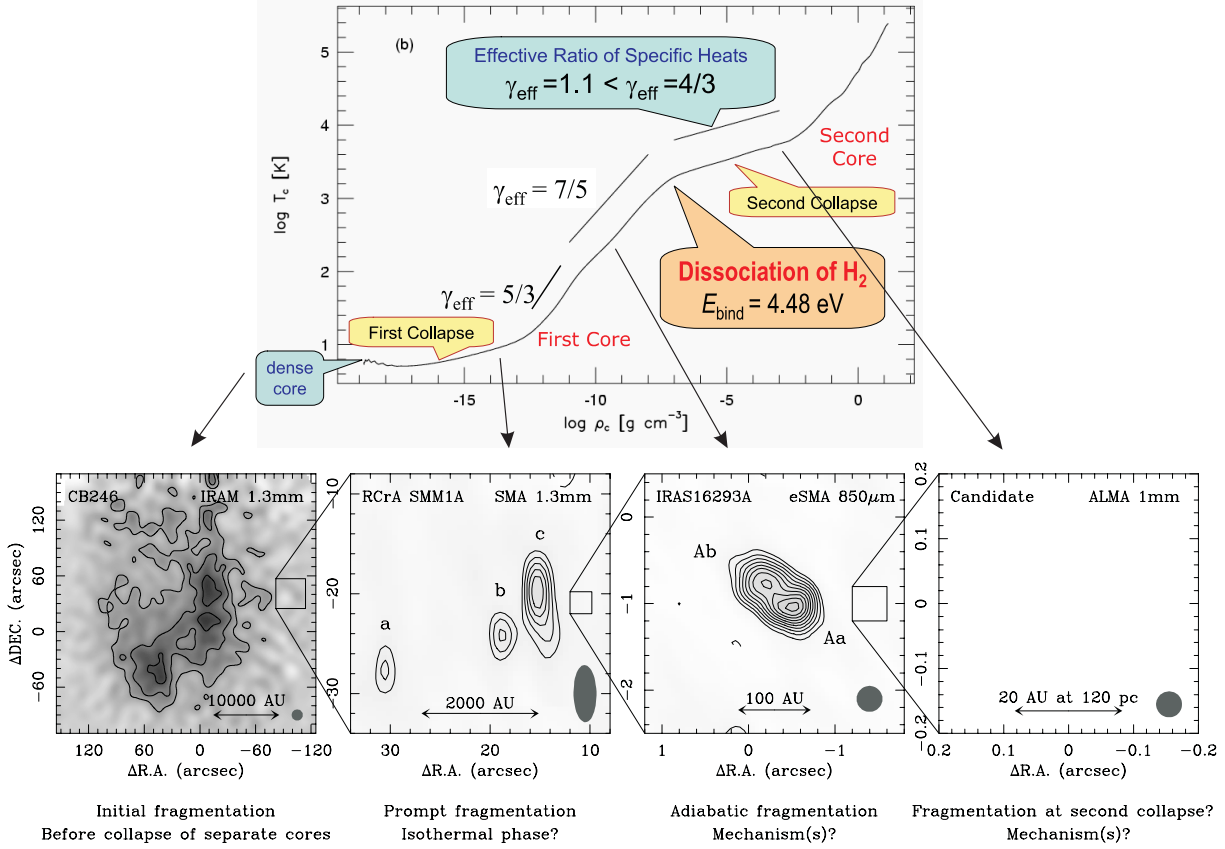


Fig. 23.— *Top:* Temperature and density evolution at the center of a gravitationally collapsing cloud core obtained by Masunaga & Inutsuka (2000) in their radiation hydrodynamical calculation of spherically symmetric protostellar collapse. Each of these phases in the temperature evolution is characterized by a distinct value of the effective ratio of specific heats,  $\gamma_{\text{eff}}$ . The image is adopted from André et al. (2009). *Bottom:* A suggested picture of the sequential fragmentation for binary stars. From left to right: the IRAM-30m 1.3 mm dust continuum image of Bok globule CB 246 (data from Launhardt et al. 2010), the SMA 1.3 mm dust continuum image of R CrA SMM1A (data from Chen & Arce 2010), and the eSMA 850  $\mu\text{m}$  image of IRAS16293 A (this work), while the right blank panel shows a possible view with an angular resolution of  $0''.04$  attained at the ALMA.